

# Solution processed hybrid solar cells : structure and material considerations

Sun, Shuangyong

2015

Sun, S. (2015). Solution processed hybrid solar cells : structure and material considerations.  
Doctoral thesis, Nanyang Technological University, Singapore.

<https://hdl.handle.net/10356/62175>

<https://doi.org/10.32657/10356/62175>



**NANYANG**  
**TECHNOLOGICAL**  
**UNIVERSITY**

**SOLUTION PROCESSED  
HYBRID SOLAR CELLS  
- STRUCTURE AND MATERIAL  
CONSIDERATIONS**

SUN SHUANGYONG

SCHOOL OF MATERIALS SCIENCE AND ENGINEERING

2015

**Solution processed hybrid solar cells**  
**- Structure and material considerations**

**SUN SHUANGYONG**

**School of Materials Science and Engineering**

A thesis submitted to the Nanyang Technological University

In partial fulfillment of the requirement for the degree of Doctor of Philosophy

**2015**

## Acknowledgments

The author would like to express his sincere gratitude to the following people who have offered their help during his PhD journey, without whom this thesis cannot be completed.

First and foremost, I would like to thank my supervisor Assoc. Prof. Lam Yeng Ming for her advice, support and patience throughout the course of my PhD study. I am very grateful for the invaluable guidance she has provided. Her positive attitude about life and research work inspires me a lot.

I would also like to thank my co-supervisor Assoc. Prof. Sum Tze Chien for sharing his knowledge with me. I appreciate the help from his group members, especially Dr. Xin Guichuan, in running all the photophysics related experiments in their femosecond dynamics lab.

I also need thank Dr. Melvin T. Zin for letting me work in the R&D lab of 3M Singapore for two years. I learnt a lot from him and the colleges around in the lab. The experience is an important treasure for me.

Besides, our group members Dr. Teddy Salim, Dr. Lek Jun Yan, Dr. Lam Kwan Hang, Mr. Abe Yuichiro, and Dr. Li Zhenggang are great help both in the lab and in the office. It is also a great pleasure to work together with Dr. Li Hairong. It is truly an honor to know these guys. I would like to thank all the other friends and the technical staff in showing their kindness and providing their help these years.

Lastly, I would like to thank my parents and my brother for their understanding and continuous support.



# Table of Contents

<b>Acknowledgements.....</b>	<b>i</b>
<b>Table of Contents.....</b>	<b>ii</b>
<b>List of Figures.....</b>	<b>vi</b>
<b>List of Tables.....</b>	<b>xi</b>
<b>List of Abbreviations.....</b>	<b>xii</b>
<b>List of Symbols.....</b>	<b>xiv</b>
<b>Abstract.....</b>	<b>xv</b>
 <b>Chapter 1: Introduction</b>	
1.1 Background and Motivation.....	1
1.2 Objective and Scope.....	4
1.3 Thesis Organization.....	5
 <b>Chapter 2: Literature Review</b>	
2.1 Organic and Hybrid Solar Cells.....	7
2.1.1 Device characteristics.....	9
2.1.2 Device physics.....	11
2.1.3 Device structure.....	14
2.2 BHJ Hybrid Solar Cells.....	18
2.2.1 Geometry effect of nanocrystals.....	20
2.2.2 Surface treatment of nanocrystals.....	23
2.2.3 Functionalization of polymers.....	26
2.3 Bilayer Hybrid Solar Cells.....	28

2.3.1 Exciton multiplication.....	29
2.3.2 Materials with long exciton diffusion length.....	31
2.4 References.....	34
<b>Chapter 3: P3HT:CdSe BHJ Solar Cells</b>	
3.1 Introduction.....	40
3.2 Results and Discussion.....	45
3.2.1 P3HT nanofiber and its application in HSCs.....	45
CdSe NCs and ligand exchange.....	45
Characterization of P3HT nanofiber.....	47
Device based on CdSe NCs and P3HT nanofiber.....	51
3.2.2 End-chain functionalized low molecular weight P3HT (P3HT <sub>L</sub> ).....	55
Synthesis of pyridine-terminated P3HT (P3HT <sub>L</sub> -py).....	56
Structure confirmation of P3HT <sub>L</sub> -py.....	58
Interaction between P3HT <sub>L</sub> -py and CdSe NCs.....	58
Assembly of hybrid nanostructure.....	60
Device based on hybrid nanostructure.....	62
3.3 Conclusions.....	64
3.4 Experimental Section.....	64
3.5 References.....	68
<b>Chapter 4: CH<sub>3</sub>NH<sub>3</sub>PbI<sub>3</sub> for Photovoltaic Application</b>	
4.1 Introduction.....	71

4.2 Results and Discussion.....	74
4.2.1 Characterization of $\text{CH}_3\text{NH}_3\text{PbI}_3$ thin film.....	74
Crystal structure.....	75
Film morphology.....	76
4.2.2 Optical properties of $\text{CH}_3\text{NH}_3\text{PbI}_3$ .....	77
4.2.3 Photophysical properties of $\text{CH}_3\text{NH}_3\text{PbI}_3$ .....	80
Photoluminescence (PL) spectroscopy.....	82
Transient absorption spectroscopy (TAS).....	87
4.2.4 $\text{CH}_3\text{NH}_3\text{PbI}_3$ characteristic in device.....	93
Device structure.....	93
Device performance.....	94
Effect of heat treatment.....	96
Effect of film thickness.....	97
4.3 Conclusions.....	99
4.4 Experimental Section.....	100
4.5 References.....	104
 <b>Chapter 5: <math>\text{CH}_3\text{NH}_3\text{PbI}_3/\text{PC}_{61}\text{BM}</math> Bilayer Solar Cells</b>	
5.1 Introduction.....	107
5.2 Results and Discussion.....	110
5.2.1 Device structure and material characterization.....	110
Structure layout and energy level diagram.....	110

Characterization of device cross-section.....	111
Elemental analysis.....	112
5.2.2 Optical characteristics.....	113
5.2.3 Electrical characteristics.....	115
5.2.4 Role of PC <sub>61</sub> BM and PEDOT:PSS in the device.....	117
5.2.5 Elucidating the reasons for the high performance.....	120
5.2.6 Effect of heat treatment.....	126
5.3 Conclusions.....	131
5.4 Experimental Section.....	132
5.5 References.....	136
<b>Chapter 6: Summary and Future Work</b>	
6.1 Summary.....	138
6.2 Future Work.....	144
<b>List of Publications.....</b>	<b>146</b>
<b>Appendix.....</b>	<b>147</b>

## List of Figures

Figure 2-1	Current density-voltage ( $J$ - $V$ ) characteristics of a typical solar cell.....	11
Figure 2-2	Schematic drawing of the important processes in organic/hybrid solar cells.....	14
Figure 2-3	(a) Bilayer device structure and (b) Bulk heterojunction (BHJ) device structure.....	15
Figure 2-4	(a) Domains of “dead ends” in general BHJ structure and (b) Proposed “ideal” BHJ structure.....	17
Figure 2-5	AFM phase images of P3HT and CdSe NCs blend films casted from (a) 1% v/v pyridine in chloroform and (b) 8% v/v pyridine in chloroform; surface roughness of P3HT and CdSe NCs blend films prepared from various concentration of pyridine in chloroform and the EQE of their corresponding devices (c). Images reproduced from the work done by Huynh <i>et al.</i> <sup>34</sup> .....	20
Figure 2-6	(a) EQE signals of devices based on P3HT and 7-nm-diameter CdSe NCs with length of 7 nm, 30 nm, 60 nm; TEM cross section images of blend films based on P3HT and CdSe NCs of (b) dot shape (c) rod shape. Images reproduced from the work done by Huynh <i>et al.</i> <sup>39</sup> .....	22
Figure 2-7	(a) $J$ - $V$ characteristic of devices based on P3HT and non-ligand-exchanged CdSe QDs; and the proposed QDs sphere model. (b) The dependence of device performance on the aspect ratio of CdS NCs grown in P3HT; and the proposed synthesis scheme of CdS NCs grown in P3HT matrix. Images reproduced from the works done by Zhou <i>et al.</i> <sup>51</sup> and Liao <i>et al.</i> <sup>53</sup> .....	26
Figure 2-8	(a) Synthetic scheme of grafting vinyl-terminated P3HT onto DOPO-Br functionalized CdSe QDs (b) Schematic drawing of the formation of P3HT/CdSe QDs nanocomposites and representative TEM images of P3HT/CdSe QDs nanocomposites. Images reproduced from the works done by Xu <i>et al.</i> <sup>56a</sup> and Pentzer <i>et al.</i> <sup>60</sup> .....	28
Figure 2-9	Device structure and energy diagram of solar cells based on bilayer device of ITO/Pentacene/PbS/Al. The absorption region of device in respective of solar spectrum and proposed working mechanism is also included. Images reproduced from the work done by Ehrler <i>et al.</i> <sup>72</sup> .....	31
Figure 2-10	(a) Device structure and (b) $J$ - $V$ characteristic of bilayer solar cells based on perovskite/TiO <sub>2</sub> ; (c) Device structure and (d) $J$ - $V$ curves of bilayer solar cells based on perovskite/fullerene. Images reproduced from the works done by Etgar <i>et al.</i> <sup>77</sup> and by Jeng <i>et al.</i> <sup>78</sup> .....	33
Figure 3-1	(a) TEM image of CdSe NCs right after synthesis and (b) TGA plots of CdSe NCs before ligand exchange (CdSe-SA) and after ligand exchange (CdSe-BA).....	46

Figure 3-2	(a) Evolution of absorption spectra of P3HT in <i>p</i> -xylene as a function of time, (b) Absorption spectra of P3HT nanofiber solution before centrifugation, suspension of redispersed pure nanofiber powder, and reheated pure nanofiber solution.....	48
Figure 3-3	AFM topographical images of P3HT nanofibers aged for (a) 1 h, (b) 8 h, and (c) 24 h. XRD patterns of P3HT film, P3HT film (thermal annealed), and P3HT nanofiber film (d).....	49
Figure 3-4	(a) Current density-voltage ( <i>J</i> - <i>V</i> ) characteristic of solar cells base on P3HT:CdSe and P3HT nanofiber:CdSe under one sun illumination, and (b) their corresponding EQE profiles.....	52
Figure 3-5	AFM height image (a) and phase image (b) of P3HT:CdSe solar cells; and AFM height image (c) and phase image (d) of P3HT nanofiber:CdSe solar cells.....	53
Figure 3-6	Synthesis route to prepare P3HT <sub>L</sub> -py.....	56
Figure 3-7	<sup>1</sup> H NMR spectra of (a) P3HT <sub>L</sub> and (b) P3HT <sub>L</sub> -py in CDCl <sub>3</sub> .....	57
Figure 3-8	(a) Solutions of P3HT <sub>L</sub> -py (1), CdSe NCs (2) and P3HT <sub>L</sub> -py:CdSe (3) in chlorobenzene as sonicated (top) and after one day (bottom), and (b) XPS profiles of CdSe NCs, P3HT <sub>L</sub> :CdSe and P3HT <sub>L</sub> -py:CdSe.....	59
Figure 3-9	(a) AFM image and (b) TEM image of assembled P3HT nanofiber:CdSe hybrid nanostructure.....	61
Figure 3-10	<i>J</i> - <i>V</i> characteristic of solar cells with the incorporation of assembled P3HT nanofiber without and with the presence of P3HT <sub>L</sub> -py under light illumination.....	63
Figure 4-1	(a) XRD pattern from CH <sub>3</sub> NH <sub>3</sub> PbI <sub>3</sub> thin film and (b) its crystal structure.....	76
Figure 4-2	(a) AFM height image and (b) AFM phase image of CH <sub>3</sub> NH <sub>3</sub> PbI <sub>3</sub> thin film with scan size of 4 μm x 4 μm. The high resolution images (500 nm x 500 nm) are shown in inset.....	77
Figure 4-3	(a) UV-Vis absorption spectra and (b) absorption coefficient spectra of CH <sub>3</sub> NH <sub>3</sub> PbI <sub>3</sub> thin film prepared on quartz substrates.....	78
Figure 4-4	Refractive index <i>n</i> and extinction coefficient <i>k</i> determined for CH <sub>3</sub> NH <sub>3</sub> PbI <sub>3</sub> .....	79
Figure 4-5	Step profiles of the thickness of the CH <sub>3</sub> NH <sub>3</sub> PbI <sub>3</sub> (black) film, CH <sub>3</sub> NH <sub>3</sub> PbI <sub>3</sub> /PC <sub>61</sub> BM (red) and CH <sub>3</sub> NH <sub>3</sub> PbI <sub>3</sub> /spiro-OMeTAD (blue) bilayer films.....	82
Figure 4-6	(a) Steady-state PL spectra and (b) Time-resolved PL decay transients measured at 760 ± 10 nm for CH <sub>3</sub> NH <sub>3</sub> PbI <sub>3</sub> (black), CH <sub>3</sub> NH <sub>3</sub> PbI <sub>3</sub> /PC <sub>61</sub> BM (red), and CH <sub>3</sub> NH <sub>3</sub> PbI <sub>3</sub> /spiro-OMeTAD (blue) after excitation at 600 nm (1 KHz, 150 fs). The solid lines in B are the single-exponential fit for the PL decay transients.....	86

Figure 4-7	Differential transmission ( $\Delta T/T$ ) spectra for (a) $\text{CH}_3\text{NH}_3\text{PbI}_3$ , (b) $\text{CH}_3\text{NH}_3\text{PbI}_3/\text{PC}_{61}\text{BM}$ , and (c) $\text{CH}_3\text{NH}_3\text{PbI}_3/\text{spiro-OMeTAD}$ films in vacuum after excitation at 600 nm (1 KHz, 150 fs, $13 \mu\text{J}/\text{cm}^2$ ): red (1 ps), green (100 ps), blue (500 ps), and cyan (1 ns). Normalized bleaching kinetics at (d) 480 nm and (e) 760 nm for the films in vacuum after excitation at 600 nm (1 KHz, 150 fs, $1.3 \mu\text{J}/\text{cm}^2$ ).....	89
Figure 4-8	Schematics of the possible energy levels associated with the two peaks (480 nm and 760 nm) observed in the TA spectra.....	91
Figure 4-9	Normalized bleaching kinetics at 480 and 760 nm in a short time range show the intervalence band hot-hole cooling for $\text{CH}_3\text{NH}_3\text{PbI}_3$ film after excitation at (a) 400 nm and (B) 600 nm. (b) A schematic illustration the hot-hole cooling and charge recombination within $\text{CH}_3\text{NH}_3\text{PbI}_3$ and charge separation at the $\text{CH}_3\text{NH}_3\text{PbI}_3/\text{PC}_{61}\text{BM}$ and $\text{CH}_3\text{NH}_3\text{PbI}_3/\text{spiro-OMeTAD}$ interfaces. The approximated positions of VB1 and VB2 were obtained from the TA measurement.....	92
Figure 4-10	(a) Differential transmission ( $\Delta T/T$ ) spectra of $\text{CH}_3\text{NH}_3\text{PbI}_3$ film, $\text{CH}_3\text{NH}_3\text{PbI}_3/\text{PC}_{61}\text{BM}$ film, and $\text{CH}_3\text{NH}_3\text{PbI}_3/\text{CdSe}$ film after excitation at 600 nm and probed at 760 nm and (b) Energy level diagram of the $\text{CdSe}/\text{CH}_3\text{NH}_3\text{PbI}_3$ bilayer solar cell.....	94
Figure 4-11	(a) $J$ - $V$ characteristic and (b) EQE profile of $\text{CdSe}/\text{CH}_3\text{NH}_3\text{PbI}_3$ bilayer devices.....	96
Figure 4-12	(a) $J$ - $V$ characteristic and (b) the $V_{oc}$ trend of $\text{CH}_3\text{NH}_3\text{PbI}_3/\text{CdSe}$ hybrid solar cells with the $\text{CH}_3\text{NH}_3\text{PbI}_3$ layer annealed at 30s, 2 min and 5 min.....	97
Figure 4-13	$J$ - $V$ characteristic of $\text{CH}_3\text{NH}_3\text{PbI}_3$ based solar cells with (a) various thickness of CdSe layer or (b) various thickness of P3HT layer.....	98
Figure 5-1	The schematic drawings of (a) the device layout and (b) the energy level diagram of $\text{CH}_3\text{NH}_3\text{PbI}_3/\text{PC}_{61}\text{BM}$ bilayer solar cell. The energy offset of the LUMO levels of $\text{CH}_3\text{NH}_3\text{PbI}_3$ and $\text{PC}_{61}\text{BM}$ is noted as $\Delta E$ .....	111
Figure 5-2	(a) Cross-sectional TEM image of $\text{CH}_3\text{NH}_3\text{PbI}_3/\text{PC}_{61}\text{BM}$ bilay solar cell in the bright-field mode (b) HRTEM image of the $\text{CH}_3\text{NH}_3\text{PbI}_3$ layer...	112
Figure 5-3	EDX spectra from the $\text{CH}_3\text{NH}_3\text{PbI}_3/\text{PC}_{61}\text{BM}$ bilayer solar cell. Areas A-E correspond to regions in the Al, $\text{PC}_{61}\text{BM}$ , $\text{CH}_3\text{NH}_3\text{PbI}_3$ , PEDOT:PSS and ITO layers, respectively.....	113
Figure 5-4	UV-Vis absorption spectra of standalone $\text{CH}_3\text{NH}_3\text{PbI}_3$ film, pure $\text{PC}_{61}\text{BM}$ film and the $\text{CH}_3\text{NH}_3\text{PbI}_3/\text{PC}_{61}\text{BM}$ bilayer film.....	114
Figure 5-5	(a) $J$ - $V$ characteristic and (b) EQE spectra of ITO/PEDOT:PSS/ $\text{CH}_3\text{NH}_3\text{PbI}_3/\text{PC}_{61}\text{BM}/\text{Al}$ bilayer solar cell in dark and under AM 1.5G illumination.....	116

Figure 5-6	Steady-state photoluminescence spectra of pure $\text{CH}_3\text{NH}_3\text{PbI}_3$ film, $\text{CH}_3\text{NH}_3\text{PbI}_3/\text{PC}_{61}\text{BM}$ bilayer and $\text{CH}_3\text{NH}_3\text{PbI}_3/\text{PEDOT:PSS}$ bilayer ( $\lambda_{\text{ex}} = 600 \text{ nm}$ ).....	118
Figure 5-7	$J$ - $V$ characteristic of $\text{CH}_3\text{NH}_3\text{PbI}_3$ based devices with and without top $\text{PC}_{61}\text{BM}$ layer both in dark and under light. The light and dark electrical characteristics of $\text{ITO}/\text{PEDOT:PSS}/\text{CH}_3\text{NH}_3\text{PbI}_3/\text{Al}$ device are also shown as inset image.....	120
Figure 5-8	(a) Total reflection and total absorption spectra of the bilayer solar cell, (b) calculated parasitic absorptions of individual non-active layer ITO, PEDOT:PSS and Al using the transfer-matrix formalism based on device constructure: ITO (270 nm)/PEDOT:PSS (30 nm)/ $\text{CH}_3\text{NH}_3\text{PbI}_3$ (45 nm)/ $\text{PC}_{61}\text{BM}$ (45 nm)/Al (100 nm).....	122
Figure 5-9	(a) Parasitic absorption spectra of non-active layers and the active absorption spectra of the bilayer solar cell. The total absorption is also included in comparison. (b) The active absorption, EQE and the resulting IQE profiles of the bilayer solar cell.....	123
Figure 5-10	Temperature-dependent integrated PL intensity of the $\text{CH}_3\text{NH}_3\text{PbI}_3$ film under the excitation of a 532 nm continuous-wave laser beam. The solid line is the best fit based on the Arrhenius equation.....	125
Figure 5-11	UV-vis absorption spectra of as-cast (NA) and heat-treated (TA) $\text{CH}_3\text{NH}_3\text{PbI}_3$ films. The heat treatment was done at 100 °C for 30 s. The inset shows an image of the as-cast (left) and heat-treated (right) $\text{CH}_3\text{NH}_3\text{PbI}_3$ films.....	126
Figure 5-12	Cross-sectional TEM images of the as-cast and heat-treated $\text{CH}_3\text{NH}_3\text{PbI}_3$ films from the corresponding bilayer devices. For comparison, only the perovskite layers are shown.....	127
Figure 5-13	AFM images of as-cast (a,b) and heat-treated (c,d) $\text{CH}_3\text{NH}_3\text{PbI}_3$ prepared on $\text{ITO}/\text{PEDOT:PSS}$ substrates. The images on the left (a,c) are height images, while the images on the right (b,d) are phase images.....	128
Figure 5-14	(a) $J$ - $V$ characteristic and (b) EQE spectra of the as-cast (NA) and heat-treated (TA) $\text{CH}_3\text{NH}_3\text{PbI}_3/\text{PC}_{61}\text{BM}$ bilayer solar cells under AM 1.5G illumination.....	130
Figure S1	TEM image of CdSe nanocrystals (large).....	147
Figure S2	TGA plots of CdSe NCs before ligand exchange (CdSe-SA) and after ligand exchange (CdSe-BA) (marked).....	148
Figure S3	MALDI-TOF profile of low molecular weight P3HT ( $\text{P3HT}_L$ ) used for end functionalization.....	149
Figure S4	PL spectra of thin films of P3HT nanofiber:CdSe (w/o $\text{P3HT}_L$ -py) and hybrid nanostructure (w $\text{P3HT}_L$ -py).....	150



Figure S5	ADF-STEM image of FIB sample of ITO/PEDOT:PSS/CH <sub>3</sub> NH <sub>3</sub> PbI <sub>3</sub> /PC <sub>61</sub> BM/Al bilayer device. The bright spots observed in the CH <sub>3</sub> NH <sub>3</sub> PbI <sub>3</sub> layer correspond to the material with high atomic number (Z) elements.....	151
Figure S6	EDX spectra from the CH <sub>3</sub> NH <sub>3</sub> PbI <sub>3</sub> /PC <sub>61</sub> BM bilayer solar cell. Areas A-E correspond to regions in the Al, PC <sub>61</sub> BM, CH <sub>3</sub> NH <sub>3</sub> PbI <sub>3</sub> , PEDOT:PSS and ITO layers respectively (large).....	153
Figure S7	Electric field intensity distribution in the CH <sub>3</sub> NH <sub>3</sub> PbI <sub>3</sub> /PC <sub>61</sub> BM hybrid bilayer solar cell for monochromatic illumination simulated using the transfer matrix model. The position of the local maxima for each wavelength is different.....	154
Figure S8	EQE spectra of the as-cast (NA) and heat-treated (TA) CH <sub>3</sub> NH <sub>3</sub> PbI <sub>3</sub> /PC <sub>61</sub> BM bilayer solar cells (600 nm - 800 nm) under AM 1.5G illumination.....	154
Figure S9	Dark semilog current density-voltage ( <i>J</i> - <i>V</i> ) characteristics of the as-cast (NA) and heat-treated (TA) CH <sub>3</sub> NH <sub>3</sub> PbI <sub>3</sub> /PC <sub>61</sub> BM hybrid bilayer solar cells. The dotted lines are fits to the <i>J</i> - <i>V</i> characteristics with the ideal diode equation to extract the reverse-saturation current density ( <i>J</i> <sub>0</sub> ) and ideality factor ( <i>n</i> ).....	155

## List of Tables

Table 3.1	Binding energy of Cd 3d core level in CdSe, P3HT <sub>L</sub> :CdSe, and P3HT <sub>L</sub> -py:CdSe.....	60
Table S1	Summary of XRD parameters of P3HT (NA), P3HT(TA), P3HT nanofiber films.....	148
Table S2	Summary of device performances based on P3HT:CdSe NCs device (non-fiber system) and P3HT nanofiber:CdSe NCs (fiber system), their <i>J</i> - <i>V</i> characteristic shown in chapter 3.....	149
Table S3	Summary of device performances based on P3HT nanofiber:CdSe NCs (w/o P3HT <sub>L</sub> -py) and hybrid nanostructure (with P3HT <sub>L</sub> -py), their <i>J</i> - <i>V</i> characteristic shown in chapter 3.....	150
Table S4	Summary of performance parameters of both as-cast and heat-treated CH <sub>3</sub> NH <sub>3</sub> PbI <sub>3</sub> /PC <sub>61</sub> BM hybrid bilayer solar cells, the CH <sub>3</sub> NH <sub>3</sub> PbI <sub>3</sub> thin film was prepared from a 9 wt% solution by spincoating. The heat treatment was performed at 100 °C for 30s.....	155

## List of Abbreviations

1D	One dimensional
AFM	Atomic force microscopy
BA	Butylamine
BHJ	Bulk heterojunction
CB	Chlorobenzene
CdSe	Cadmium selenide
CH <sub>3</sub> NH <sub>2</sub>	Methylamine
CH <sub>3</sub> NH <sub>3</sub> I	Ammonium iodide
CH <sub>3</sub> NH <sub>3</sub> PbI <sub>3</sub>	Methylammonium lead iodide
CODs	Colloidal quantum dots
CT	Charge transfer
D-A	Donor-acceptor
DMF	Dimethylformamide
EDX	Energy dispersive X-ray spectroscopy
EQE	External quantum efficiency
FESEM	Field emission scanning electron microscopy
FF	Fill factor
FRET	Fluorescence resonance energy transfer
HI	Hydroiodic acid
HOMO	Highest occupied molecular orbital
HSC	Hybrid solar cell
IQE	Internal quantum efficiency
ITO	Indium tin oxide
LUMO	Lowest unoccupied molecular orbital
Mw	Molecular weight
NC	Nanocrystal
NMR	Nuclear magnetic resonance
NR	nanorod
OSC	Organic solar cell
P3HT	Poly(3-hexylthiophene)
P3HT <sub>L</sub>	Low molecular weight poly(3-hexylthiophene)
P3HT <sub>L</sub> -py	Pyridine end functionalized low molecular weight P3HT
PbI <sub>2</sub>	Lead(II) iodide
PB	Photobleach
PC <sub>61</sub> BM	[6,6]-phenyl-C <sub>61</sub> -butyric acid methyl ester
PCE	Power conversion efficiency
PL	Photoluminescence
PEDOT:PSS	Poly(3,4-ethylenedioxythiophene)-poly(styrenesulfonate)
py	pyridine

R <sub>RMS</sub>	Root mean square roughness
R <sub>s</sub>	Series resistance
SA	Stearic acid
Spiro-OMeTAD	2,2',7,7'-Tetrakis-(N,N-di-4-methoxyphenylamino)-9,9'-spirobifluorene
TAS	Transient absorption spectroscopy
TD	Tetrapod
TEM	Transmission electron microscopy
TGA	Thermogravimetric analysis
TOP	Trioctylphosphine
TOPO	Trioctylphosphine oxide
TRPL	Time-resolved photoluminescence spectroscopy
UV-vis	UV-visible
XPS	X-ray photoelectron spectroscopy
XRD	X-ray diffraction

## List of Symbols

$2\theta$	Bragg angle
$\alpha$	Absorption coefficient
$\lambda$	Wavelength of light
$\tau_o$	Time constant
$\tau_{CT}$	Charge transfer time
$\eta_{CT}$	Charge transfer efficiency
$\Delta E_{LUMO}$	LUMO difference between donor and acceptor
$J_{sc}$	Short-circuit current
$k$	Extinction coefficient
$L_D$	Diffusion length
$N$	Ideality factor
$V_{oc}$	Open-circuit voltage

## Abstract

Hybrid solar cells (HSCs) combine the advantages of both organic and inorganic materials, and can therefore have the potential to realize high performance at low production cost. Nevertheless, the performance of state-of-the-art HSCs is still low currently, mainly due to a lack of percolation pathways for charge transport in the photoactive layer after thin film deposition. On top of this, the physical distance between conjugated polymers and inorganic nanocrystals (NCs) is large and can therefore retard the charge transfer between them. In this thesis, two different approaches have been developed to address these issues. In the first approach, the integration of self-assembled nanostructures into HSCs to boost device performance has been demonstrated. It was found that after the incorporation of pre-assembled poly(3-hexylthiophene) (P3HT) nanofiber, solar cells based on cadmium selenide (CdSe) NCs showed better performance than those solar cells containing non-assembled P3HT. The enhanced efficiency mainly resulted from the increase in  $J_{SC}$ , which could be attributed to the enhanced light absorption and better charge transport due to the presence of P3HT nanofiber. To improve the interaction between P3HT nanofiber and CdSe NCs, pyridine terminated low molecular weight P3HT (P3HT<sub>L</sub>-py) has been synthesized and incorporated into solar cells. The presence of favorable interaction between P3HT<sub>L</sub>-py and CdSe NCs was confirmed by solution stability study and XPS study. An ordered hybrid nanostructure was then prepared by co-assembly of P3HT and P3HT<sub>L</sub>-py in solution, followed by the attachment of CdSe NCs around the preformed functionalized nanofiber. When devices were fabricated from such hybrid solutions, the PCE increased by more than 20% compared to those devices based on pure P3HT nanofiber and CdSe NCs. It was believed

that the enhanced performance was related to a more intimate donor-acceptor (D-A) interface, due to the presence of the additional interaction force. In another approach, methylammonium lead iodide ( $\text{CH}_3\text{NH}_3\text{PbI}_3$ ) has been synthesized and explored for photovoltaic application aiming to bypass challenges in obtaining optimal morphology in HSCs. It has been found that  $\text{CH}_3\text{NH}_3\text{PbI}_3$  exhibited excellent optical properties, with wide absorption window and large absorption coefficient. Besides, experiments based on ultrafast laser spectroscopy have shown that  $\text{CH}_3\text{NH}_3\text{PbI}_3$  had large and balanced electron and hole diffusion lengths. To evaluate the photovoltaic performance of  $\text{CH}_3\text{NH}_3\text{PbI}_3$ , it was first coupled with CdSe NCs to make HSCs. It was found that solar cells based on such material combination could show decent performance (PCE of 2.6%). However, low fill factor (FF) limited the device performance, which was attributed to the high series resistance in the CdSe layer. To avoid this issue, subsequently  $\text{PC}_{61}\text{BM}$  was applied to replace CdSe NCs to make solar cells. It has been found that  $\text{CH}_3\text{NH}_3\text{PbI}_3/\text{PC}_{61}\text{BM}$  bilayer solar cells could show a PCE of up to 5.23%, which is quite amazing considering the bilayer device structure adopted. The high performance was because the internal quantum efficiency (IQE) of the bilayer solar cell was close to 100%. This implied almost all the absorbed light contributed to the output current in such system.

# Chapter 1

---

## Introduction



## **1.1 Background and Motivation**

The global energy demand is increasing every year due to the growth of world population and economy. According to Statistical Review of World Energy by British Petroleum (BP) published online in 2013, there is a 2.3% of growth in the world energy consumption compared to that in the previous year, and the developing countries already hold 56.5% share of the global energy consumption. The energy needs for the industrialization of the developing countries are still huge in a long period of time. The world energy supply is mainly provided by the non-renewable (primary) energy sources such as oil, coal, and natural gas. Nevertheless, the reserves of non-renewable energy sources are quite limited. This raises the concern that the world's energy supply may not meet its demands in the long run, which will be a big disaster for the modern civilization. On the other hand, greenhouse gases emission and other environmental issues are related to the consumption of the non-renewable energy sources. To meet this challenge, huge investments have been going to projects across the world to seek energy that is clean, sustainable and cheap.

Sustainability in the urban environment is always an important issue for Singapore due to its constrained land space and a lack of natural resources. Singapore has to import the natural gas (70%) and crude oil (30%) from other countries for its power generation. In 2007, the government committed to invest more than S\$1 billion on the research and development (R&D) of the renewable energy technologies. As Singapore has good clean technology infrastructure across the island and is located within the Asian Sunbelt, it is a good place to demonstrate new energy solutions before they are scaled up in the rest of world, especially in Asia. The test-bed achievements can be readily transferred to many

other Asian cities. The impact can be significant as half of the world's population is in Asia.

One of the most promising solutions to the world energy crisis is harvesting of solar energy and converting it directly into electricity since this form of energy is both clean and renewable. Currently, commercially available solar cells are mostly made of inorganic materials (e.g. silicon and CIGS), and they can provide high efficiency with long term stability. Nevertheless, the high production cost and long payback time of these inorganic solar cells make them less competitive than those tradition energy sources, and limit their share in the energy market. As a result, excitonic solar cells including dye-sensitized solar cells (DSSCs), organic solar cells (OSCs) and organic/inorganic hybrid solar cells (HSCs) are being developed. OSCs offer several advantages over inorganic solar cells. They can be readily fabricated on large substrates via solution processing techniques to reduce the production cost. Besides, they can be printed on plastic substrates to offer flexible and light weight solar cells, which are compatible with portable consumable electronics. In addition, they can have good performance even in low light conditions, which is suitable for indoor application.

In general, conjugated polymers are applied as donor material for OSCs (e.g. poly(3-hexylthiophene, P3HT); while fullerene derivative such as [6,6]-phenyl-C<sub>61</sub>-butyric acid methyl ester (PC<sub>61</sub>BM) are used as electron acceptor. When fullerene molecules are replaced by inorganic semiconducting nanocrystals (NCs) (e.g. CdSe), the blend system is often known as HSCs. Inorganic NCs can offer several benefits when they are integrated into solar cells, such as tunable bandgap to provide complementary light absorption, high electron affinities for more efficient charge transfer, high electron

mobility for better charge transport, and good stability for longer device lifetime. For state-of-the-art organic/hybrid solar cells, donor and acceptor materials are commonly blended together to form the photoactive layer, adopting a bulk heterojunction (BHJ) device structure. Although HSCs have supreme properties over OSCs in theory, their device performances are rather low to date. The main problem in HSCs is that it is difficult to achieve interpenetrating percolation pathways for hole and electron transport in the blend film simultaneously, due to the different nature of organic and inorganic materials. Besides, the long physical distance between polymer and NCs can impede charge transfer between them, which results from surface ligands on NCs and alkyl chains of polymers. Two strategies are often applied to improve the performance of HSCs. The first one is to make use of the geometry of these NCs. It has been shown that NCs in rod shape can improve charge transport in the blend film due to the reduced hopping steps for electrons. The second strategy is the surface treatment of inorganic NCs - replacing the long bulky ligand necessary for the synthesis with small molecules. Post-synthesis ligand exchange can improve charge transfer between polymer and NCs and charge transport among NCs, and this is already an essential step for hybrid device fabrication. But this treatment often causes a reduction in the colloidal stability and induces the aggregation of NCs during film formation. Various organic molecules have been evaluated with the aim to achieve high conductivity while maintaining high stability for NCs, but they have not yielded device performance better than OSCs so far. Morphology and interface control of the blend film in HSCs is a great challenge. New strategies need be explored to achieve highly efficient solution-processed HSCs.

## 1.2 Objectives and Scope

To address the issues mentioned above, the main objectives and scope of this thesis are:

**(a) To demonstrate the possibility of using self-assembled nanostructure to improve HSCs.** Rather than depending on the phase separation occurring in-situ during the drying process, polymer nanostructure will be incorporated into HSCs to create a partially organized morphology. This will create more percolated pathways for charge transport. Solution-assembled P3HT nanofibers will be prepared and fully characterized, and their effect on the performance of HSCs will be studied. Subsequently, hybrid nanostructure will be prepared by using polymer nanostructure as soft template for NCs to graft onto, and they will be integrated into HSCs. Low molecular weight P3HT (P3HT<sub>L</sub>) bearing pyridine functional groups to provide favorable interaction force will be synthesized and fully characterized. Structured P3HT/CdSe nanocomposite will be prepared by co-assembly of P3HT and P3HT<sub>L</sub> to form functionalized P3HT nanofiber, followed by the attachment of CdSe NCs. The morphology of hybrid nanocomposite will be characterized by AFM and TEM, and its effect in solar cells will be investigated.

**(b) To bypass morphology control for HSCs and take the advantage of bilayer structure.** New materials with high exciton diffusion length will be explored for photovoltaic application. Hybrid lead halide in perovskite structure will be prepared, and fully characterized by optical spectroscopy, XRD, AFM. The photophysics response of these materials will be examined by ultrafast optical spectroscopic techniques. Hybrid perovskite will be then used as donor material coupled with both CdSe NCs and PC<sub>61</sub>BM in bilayer structure to look at how these HSCs perform. Parameters affecting device

performance such as film thickness and thermal treatment will be investigated. The operation mechanism of their corresponding good devices will be studied in detail.

### **1.3 Thesis Organization**

This thesis consists of six chapters. The first chapter provides an overview of the research field and elaborates the initial motivation behind the research work.

In chapter two, the historical development of solar cells is introduced at first. The operation mechanism, important device parameters, and characterization techniques of organic/hybrid solar cells are also reviewed. The challenges and the strategies to improve the performance of current state-of-the-art HSCs are highlighted as well.

Chapter three presents a general strategy for morphology and interface control in HSCs by taking the benefits of *p*-type nanostructure. The effect of the incorporation of solution assembled P3HT nanofiber on device performance has been discussed. A pyridine-terminated low molecular weight P3HT (P3HT<sub>L</sub>-py) has been synthesized as compatibilizer to improve the interaction between polymer nanofiber and CdSe NCs. Finally, solar cells based on the organized hybrid nanostructure were demonstrated.

In chapter four, the synthesis of hybrid perovskite methylammonium lead iodide (CH<sub>3</sub>NH<sub>3</sub>PbI<sub>3</sub>) is presented and the important properties of this material for solar energy harvesting are fully studied. The characterization studies include looking into the optical properties, structural properties, and thin film morphology. The fundamental optoelectronic properties of CH<sub>3</sub>NH<sub>3</sub>PbI<sub>3</sub> probed by transient photoluminescence and absorption techniques are also presented. In addition, the performance of HSCs using

$\text{CH}_3\text{NH}_3\text{PbI}_3$  as the absorber and donor and CdSe NCs as the electron acceptor has been evaluated.

Chapter five demonstrates a highly efficient solution-processed hybrid solar cells based on  $\text{CH}_3\text{NH}_3\text{PbI}_3$  and  $\text{PC}_{61}\text{BM}$  in bilayer structure. The devices have been carefully examined by TEM, FESEM and EDX to confirm its structure. The functions of important layers in the devices have been investigated. The origin of the high performance in the device has also been explored and discussed.

In the last chapter, an overall summary of the thesis is provided, and recommendations on other further studies in this research area are present.

# Chapter 2

---

## Literature Review

## 2.1 Organic and Hybrid Solar Cells

The world energy consumption is increasing every year while the supply of conventional energy sources such as oil and natural gas is limited. To meet this challenge, new technologies should be adopted to reduce energy loss during daily usage; and new renewable energy sources should be exploited. Solar energy is the one of the most abundant and sustainable energy source available.<sup>1</sup> Solar energy can be harvested as thermal power using solar heating and cooling (SHC) or using concentrated solar power (CSP) technologies; or as electricity using solar cell technologies. In recent years, the frequent occurrence of extreme weather events in the world due to energy-related greenhouse gas emissions forced governments all over the world to implement stronger policies to encourage the expansion of the renewable energy portion in the energy sector.<sup>2</sup> Under such environment, solar cells are expected to become one of the major players in the energy markets in the long run.

Although the photovoltaic behavior was discovered in the early 19<sup>th</sup> century, the first solar cell based on silicon was only reported in 1954 by Chapin *et al.*<sup>3</sup> To date, these monocrystalline silicon (*m*-Si) based solar cells can have power conversion efficiency (PCE) as high as up to 25%.<sup>4</sup> However, the production cost of crystalline silicon solar cells is very high even if polycrystalline silicon (*p*-Si) is used rather than *m*-Si as the growth of silicon crystals with high purity is both difficult and energy intensive. To reduce the cost for solar cells, second generation solar cells based on thin film technology was developed and the cost was kept lower because less material was used in these solar cells and cheaper fabrication processes were developed. This category basically includes three types of solar cells: amorphous silicon (*a*-Si), cadmium telluride (CdTe) and copper indium gallium



selenide (CIGS). Nevertheless, their efficiency drops compared to those of the first generation solar cells. The best performance of the devices based on *a*-Si, CdTe and CIGS are confirmed to be 10.1%, 19.6% and 19.6% respectively.<sup>4</sup> Despite the high efficiency, these inorganic solar cells suffer the problems of scarcity in the raw material, material toxicity and relatively high production cost. In recent decades, several emerging technologies have evolved in the field of PV and are expected to produce high efficient solar cells at low cost. These new generation solar cells include dye-sensitized solar cell (DSSC),<sup>5</sup> organic solar cells (OSCs)<sup>6</sup> and organic-inorganic hybrid solar cells (HSCs).<sup>7</sup>

Organic solar cells (OSCs) are made from conjugated molecules and they work fundamentally differently from the inorganic solar cells from the perspective of photocurrent generation. Inorganic solar cells are based on p-n junctions, and light absorption results in the direct formation of free electrons and holes, which can readily stored or made use of. By contrast, when light is absorbed by OSCs, it leads to the formation of tightly bounded electron-hole pairs commonly known as excitons. To generate electrical current, excitons have to dissociate into free electron and hole pairs first. Though free charges cannot be generated so easily compared to inorganic solar cells, OSCs have several advantages. First of all, conjugated polymers have very high absorption coefficient (usually  $> 10^5$  /cm in the UV-Vis region), therefore, OSCs can be very effective as thin film devices and this implies low consumption of materials.<sup>8</sup> Secondly OSCs can be manufactured on lightweight flexible substrates using low cost techniques such as roll-to-roll processing because organic semiconductors can dissolve in various solvents easily. In addition, due to their unique nature, OSCs can perform well under high temperature and low light conditions.<sup>9</sup> Therefore, OSCs have strong potential for the application in

consumer electronics especially since the efficiency of these cells has been improving substantially in recent years. Lately, it has been reported by Toray Industries Inc that OSCs based on their thin polymer film can reach a PCE of up to 10.6%.<sup>4</sup> Despite the enormous success of OSCs, further improvements are required to boost their device performance and stability so that they become a competitive technology to bulk/thin film inorganic solar cells.

In general, charge carrier mobilities of organic semiconductors are much lower than that of the inorganic semiconductors. For example, the hole and electron mobilities of silicon are  $475 \text{ cm}^2/(\text{Vs})$  and  $1500 \text{ cm}^2/(\text{Vs})$  respectively; while hole mobilities of conjugated polymers range from  $10^{-7}$  to  $10^{-1} \text{ cm}^2/(\text{Vs})$ ,<sup>10-12</sup> and their electron mobilities are from  $10^{-9}$  to  $10^{-4} \text{ cm}^2/(\text{Vs})$ .<sup>11,13</sup> As such, hybrid solar cells (HSCs) are developed to make use of the advantage of the inorganic material - high charge mobility of inorganic semiconductors while maintaining the solution processability of organic thin films.

### **2.1.1 Device characteristics**

Power conversion efficiency (PCE) is one of the most important parameters to evaluate the performance of a solar cell. It refers to the percentage of incident light that is converted into electricity by the solar cell. Figure 2-1 shows the current density-voltage ( $J$ - $V$ ) characteristics of a typical solar cell under illumination. Several basic parameters can be extracted from the curve. (1) Short circuit current ( $J_{sc}$ ):  $J_{sc}$  is the current generated under light at zero bias, denoted by the intersection of the curve with the y-axis. (2) Open-circuit voltage ( $V_{oc}$ ):  $V_{oc}$  is the applied voltage at zero current, denoted by the intersection of the curve with the x-axis. (3) Maximum power output ( $P_{max}$ ):  $P_{max}$  of the solar cell is the product of  $J_{max}$  and  $V_{max}$ , which is shown as the largest rectangle area fitting under the  $J$ -

V curve. The PCE is defined as the ratio of  $P_{\max}$  to the power input from the sun ( $P_{in}$ ), which can be given by

$$PCE = \frac{P_{max}}{P_{in}} = \frac{J_{max} \times V_{max}}{P_{in}} = \frac{J_{sc} \times V_{OC} \times FF}{P_{in}}$$

where the fill factor (FF) is defined as

$$FF = \frac{J_{max} \times V_{max}}{J_{sc} \times V_{OC}}$$

Quantum efficiency (QE) is another important parameter to characterize the performance of a solar cell. It is the ratio of the number of charge carriers collected per incident photon by the solar cell under short circuit condition. It is also known as the incident photon-to-current efficiency (IPCE), which can be expressed as

$$EQE = \frac{\text{number of electrons}}{\text{number of photons}} = \frac{J_o/e}{P_{in}/\frac{hc}{\lambda}} = \frac{hc}{e\lambda} \times \frac{J_{sc}}{P_{in}}$$

where  $J_o$  is the current density (in A/cm<sup>2</sup>),  $P_{in}$  is the illumination (in W/cm<sup>2</sup>),  $h$  is the Planck constant,  $c$  is the speed of light in vacuum,  $e$  is the elementary charge and  $\lambda$  is the wavelength. Note that not all the incident light can be absorbed by solar cells and some portion of the light will be lost due to the reflection at the surface, and/or transmission through the device. If only the absorbed light is taken into account for the calculation of quantum efficiency, then the term is known as internal quantum efficiency (IQE), which is defined as

$$IQE = \frac{\text{number of electrons}}{\text{number of absorbed photons}} = \frac{EQE}{1 - \text{Reflection} - \text{Transmission}}$$

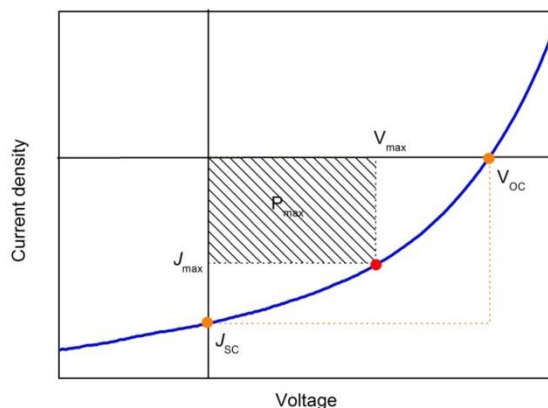


**Figure 2-1:** Current density-voltage ( $J$ - $V$ ) characteristics of a typical solar cell.

### 2.1.2 Device physics

In the first organic solar cells fabricated, the photoactive layer only comprised of one single organic semiconductor. For a long period of time, the efficiency of OSCs stayed extremely low in the order of 0.1%.<sup>14</sup> It is found that the work function difference between the two electrodes is insufficient to dissociate the excitons generated in the organic semiconductors into free charge carriers. For instance, in polymer thin film made of poly[2-methoxy-5-(2-ethylhexyloxy)-1,4-phenylenevinylene] (MEH-PPV), 90% of the excitons generated from the light recombine and do not contribute to the generation of free carrier in the end.<sup>15</sup> A significant breakthrough was achieved in 1985 by Tang, who demonstrated OSC based on copper phthalocyanine (CuPc) and perylene tetracarboxylic derivative can obtain an efficiency of up to 1%.<sup>16</sup> The increased performance was attributed to the efficient exciton dissociation at the CuPc/PV interface. Since then, two materials of different electron affinity and ionization potential are used to make OSCs. Therefore, one material shows electron-donating behavior and the other material can acceptor electrons easily. The

material with low ionization potential is the electron donor (D); while the material with high electron affinity is the electron acceptor (A). For OSCs, the donor material is often conjugated polymers or small molecules; and the acceptor material is usually fullerene derivatives, such as [6,6]-phenyl-C<sub>61</sub> butyric acid methyl ester (PC<sub>61</sub>BM). While for hybrid solar cells, the electron acceptor is normally inorganic semiconductor nanocrystals (NCs).

The photocurrent generation in organic/hybrid solar cells is a multistep process as shown in Figure 2-2.<sup>17</sup> In brief, there are four fundamental steps involved for the state-of-the-art heterojunction organic/hybrid solar cells:

(1) *Photon absorption and exciton formation.* When incident light reaches solar cells, it is absorbed mainly by the donor material and partially by the acceptor material. Photons with energy  $h\nu$  (where  $h$  is the Planck's Constant,  $\nu$  is the frequency of the photon) larger than or equal to the bandgap ( $E_g$ ) of the donor can excite the electrons from the highest occupied molecular orbital (HOMO) level to the lowest unoccupied molecular orbital (LUMO) level and leave behind holes, giving rise to excitons with a binding energy typically about 0.2-0.5 eV.<sup>18</sup> In comparison, the thermal energy at room temperature is only 0.025 eV which is not sufficient to dissociate the excitons into free electron-hole pairs. These excitons are often referred as singlet excitons, and the lifetime of these is very short in the nanosecond (ns) range. Some excitons with longer lifetime in the microsecond ( $\mu$ s) range can be also created, and these are the triplet excitons.

(2) *Exciton diffusion.* To generate separated electrons and holes, excitons must diffuse to the donor/acceptor (D/A) interface. Since excitons are neutral species, their movement is

not affected by the electric field, rather they are driven by the concentration gradient. Excitons diffuse randomly in the donor phase via long-range Förster resonant energy transfer (FRET), and have typical diffusion length of around 10 nm.<sup>19</sup> Excitons that cannot reach the D/A within their lifetime will decay and do not contribute to the output photocurrent.

*(3) Exciton dissociation and charge generation.* For the charge dissociation to happen, donor and acceptor must form type-II heterojunction where the HOMO level of the donor is lying between the LUMO level and the HOMO level of the acceptor, and the LUMO level of the donor is higher than that of the acceptor. Besides, the energy offsets of both HOMO and LUMO levels must be larger than the exciton binding energy.<sup>20,21</sup> If the charge transfer is energetically favored at the interface, electron is transferred to the acceptor while the hole remains at the donor, forming a charge transfer (CT) state after exciton dissociation. The electron-hole pair remains bound at the interface due to the Coulombic attraction. Subsequently, these CT states can separate into free electrons and holes, or decay via nonradiative or radiative recombination.

*(4) Charge transport and charge collection.* After the dissociation, electrons and holes stay in the acceptor and donor phases respectively, and they will be transported towards their respective electrodes in the opposite direction, driven by an internal electric field resulting from the difference in Fermi level of the two electrodes. However, the separated electrons and holes may recombine at defect sites and this reduces the output electrical current of the devices. And the efficiency of charge transport within the active layer strongly depends on the mobilities of charge carriers in the film.

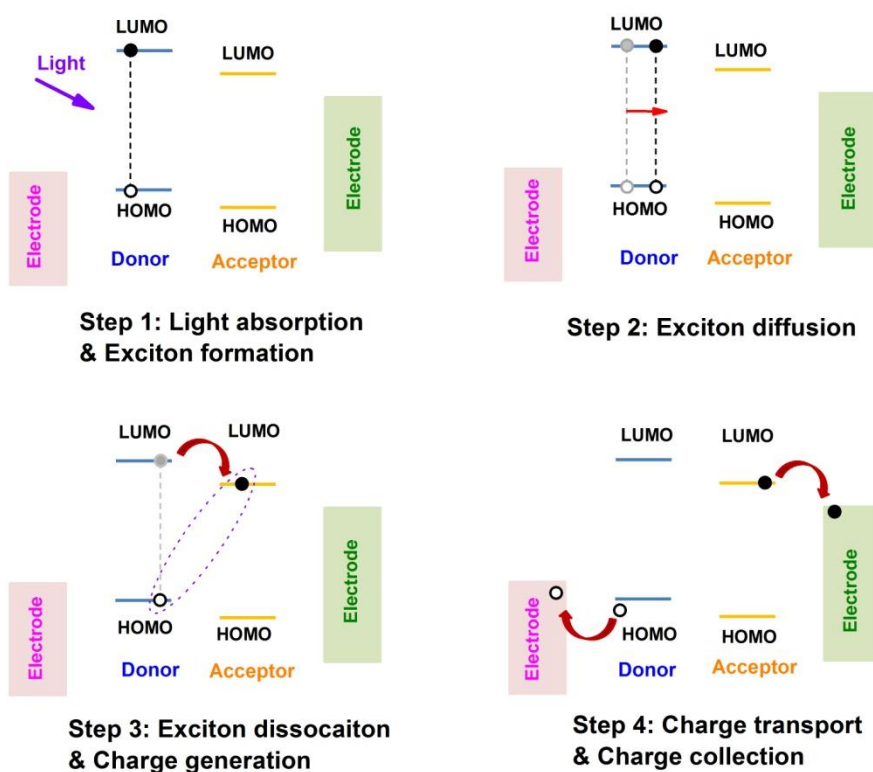


**Figure 2-2:** Schematic drawing of the important processes in organic/hybrid solar cells.

### 2.1.3 Device structure

Solar cells are thin film optoelectronic devices with photoactive layer sandwiched between two electrodes and the polarity of the solar cells in most cases depends on the relative work function of the electrodes. Indium tin oxide (ITO) with high work function is often used as anode. The photoactive layer with film thickness of ~100 nm can be solution or vacuum deposited on ITO substrates. The top metal electrodes (e.g. Al, Ag, Au) can be deposited on the top of photoactive layer in high vacuum. To provide better energy level match for

charge collection or device stability, additional anode and/or cathode buffer layer can be prepared between photoactive layer and the electrode.

Depending on the construction of the photoactive layer, the state-of-the-art organic/hybrid solar cells can be divided into two categories: bilayer devices and bulk heterojunction (BHJ) devices. These two architectures are the most basic device structures.

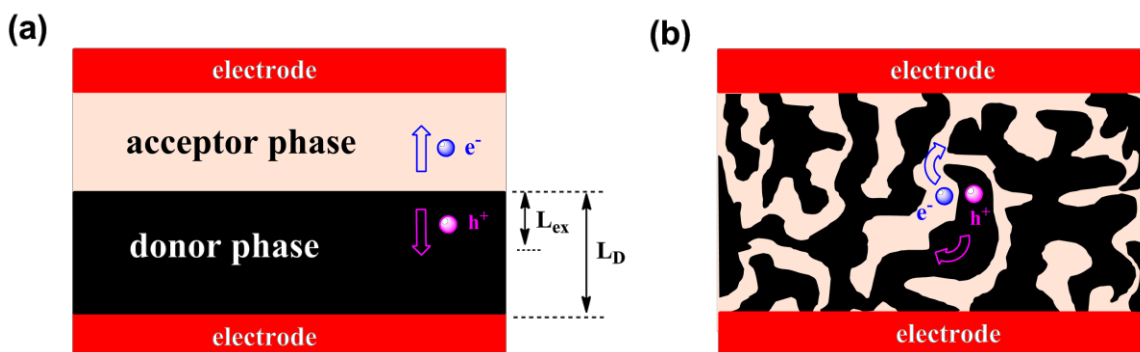


**Figure 2-3:** (a) Bilayer device structure and (b) bulk heterojunction (BHJ) device structure.

*1) Bilayer device.* In a bilayer solar cell, two separate layers of donor and acceptor materials are stacked on top of each other to form the photoactive layer, shown in Figure 2-3a. As mentioned earlier, the exciton diffusion length ( $L_e$ ) of conjugated molecules is very short ( $\sim 10$  nm) and excitons can only dissociate at the D/A heterojunction. Excitons can be collected efficiently only in the region close to the interface within the range of excitation diffusion length, and the excitons generated beyond will decay to the ground states. Hence, to maximize the efficiency of exciton generation in the solar cell, the thickness of polymer film should be comparable to the exciton diffusion length. However, to ensure effective light absorption, the film thickness ( $L$ ) of organic semiconductor should be in the range of 100-200 nm, according to the extinction coefficients. This length scale is much larger than



that of exciton diffusion length. Therefore, the performance of bilayer solar cells is limited by charge generation. Once free charges carriers are created, they can be transported to their respective electrodes efficiently. The transport in pure transport layers minimizes the possibility of recombination losses.

2) *Bulk heterojunction device*. To overcome the problem that not all the excitons can reach the heterojunction, donor and acceptor materials can be intimately mixed together to increase the D/A interfaces. This method was first introduced by Yu *et al.*<sup>22</sup> and the resulting device architecture is often referred to as a bulk heterojunction (BHJ) structure (Figure 2-3b). In the new design, as the interfacial area of electron donor and acceptor is dramatically increased, excitons do not have to travel a long distance to reach the interfaces. The possibility of exciton recombination before dissociation becomes much smaller. However, in BHJ structure, domain islands of donor or acceptor may form, as illustrated in Figure 2-4a. Charges generated on the islands get stuck, and cannot contribute to the output current. In general, the performance of BHJ solar cell is mainly limited by the charge transport due to the lack of continuous charge transport pathways. Therefore, morphology control is vital for BHJ solar cells in terms of device performance, and extensive studies have been done to optimize the morphology via various techniques (e.g solvent annealing, additive) and characterization tools (e.g AFM, TEM). Now it is widely accepted that an interdigitated donor-acceptor configuration is the “ideal” BHJ morphology that should be achieved. As shown in Figure 2-4b, in such “ideal” morphology, interpenetrating networks of the donor should form in the acceptor phase, and vice versa. The width of continuous transport paths consisting of either donor or acceptor material for holes or electrons should be on the same order as the exciton diffusion length, and a thin layer of donor film above

the anode and acceptor film below cathode is formed to suppress interfacial charge recombination and ensure efficient charge collections. Currently, two approaches are commonly adopted to realize the “ideal” BHJ morphology. In approach one, inorganic nano-arrays (could be acting as acceptor) are printed first by lithography technology, then infiltrated with conjugated molecules.<sup>23</sup> In the second approach, polymer brush grown directly from the substrates, sequentially grafted with inorganic nanocrystals.<sup>24</sup> However, both methods face some critical problems. The issue with the first approach is the size of the arrays is limited by the precision of lithography; and with the second approach, it is challenging to make thick standing polymer film for sufficient light absorption. The resulting device architecture is generally not considered as standard BHJ structure and the details of these techniques are beyond this review. The focus of the research works is on the morphology control of blend films in which donor and acceptor materials are deposited simultaneously.

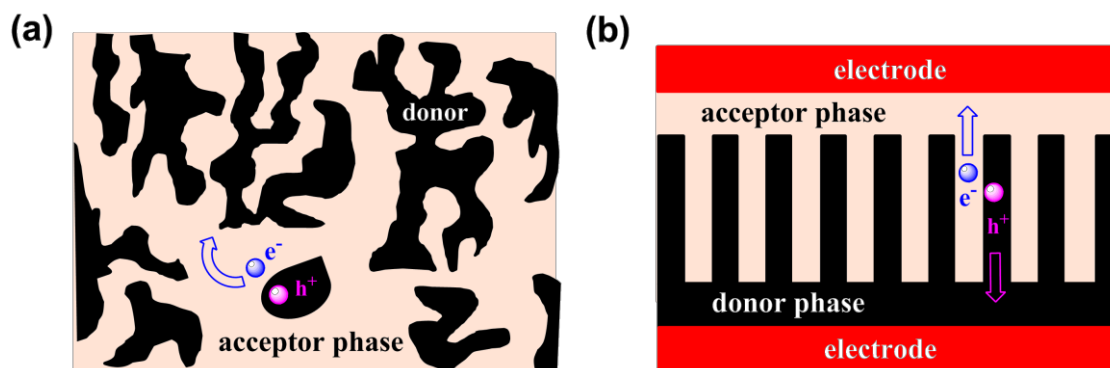


**Figure 2-4:** (a) Domains of “dead ends” in general BHJ structure and (b) proposed “ideal” BHJ structure.

## 2.2 BHJ Hybrid Solar Cells

The bulk heterojunction (BHJ) structure has a strong advantage over bilayer structure in terms of charge generation because of the large interfacial area available for excitons to split. This is the structure that currently most hybrid solar cells are based on. BHJ hybrid solar cells are generally made from the blend solution of conjugated polymers and inorganic semiconductor nanocrystals (NCs), which are commonly synthesized via hot coordinating/non-coordinating solvents method. Various types of inorganic NCs, such as ZnO,<sup>25</sup> TiO<sub>2</sub>,<sup>26</sup> CdSe,<sup>27</sup> CdS,<sup>28</sup> CdTe,<sup>29</sup> PbS,<sup>30</sup> and PbSe,<sup>31</sup> have been employed as electron acceptors for BHJ hybrid solar cells. Metal oxide NCs are interesting as they are less toxic and can be synthesized in large quantities easily. It has been shown that devices based on ZnO NCs and polymer poly[2-methoxy-5-(3',7'-dimethyloctyloxy)-1,4-phenylenevinylene](MDMO-PPV) can reach a PCE of 1.4%,<sup>32</sup> and the devices made of blends of TiO<sub>2</sub> NCs modified with dye molecule and poly(3-hexylthiophene) (P3HT) can also show a PCE of 1.2%.<sup>33</sup> However, as metal oxides have relative large bandgap, NCs based on metal oxides cannot contribute to light absorption. Besides, the solubility of metal oxide NCs in organic solvent is low in general, which is bad for device processing and further optimization. Low bandgap NCs (e.g. CdTe, PbS, PbSe) that can absorb light in the infrared region have been explored for photovoltaic application too. Xu *et al.* have shown that the performance of P3HT/PbSe NCs hybrid solar cells is 0.14%, with  $V_{oc}$  of 0.35V.<sup>34</sup> In general, the performance of BHJ hybrids solar cells based on low bandgap NCs at present are limited by their low operating voltage because energy transfer rather than electron transfer often happens between polymer and the low bandgap NCs.<sup>35</sup> In comparison, CdSe NCs have several advantages as electron acceptors for BHJ hybrid solar

cells. First, NCs absorb in the UV-Vis region, which is complementary to the absorption of polymer donors. Second, they are good electron acceptors for conjugated polymers. Third, CdSe NCs with high crystallinity and good size distribution can be synthesized easily. As a result, extensive studies of BHJ hybrid solar cells have been undertaken based on CdSe NCs.

For solar cells based on BHJ structure, the performance of devices strongly depends on the morphology of the active layer because the efficiency of charge generation, charge transport and charge collection are determined by the nanomorphology of the blend film.<sup>36</sup> Morphology control to achieve interpenetrating networks of donor phase and acceptor phase is always the key focus for BHJ solar cells. Phase separation should be optimized to balance between charge separation and charge transport. Similar to OPV, processing solvent has a strong impact on the film morphology of hybrid solar cells and their device performance. The dependence of morphology and efficiency of hybrid solar cells on processing solvents are well demonstrated by Huynh *et al.*<sup>37</sup> In this study, a two solvent system - chloroform and pyridine was used to control the morphology of P3HT and CdSe NCs films. It was found that by adjusting the amount of pyridine in chloroform, the phase separation of the blend film can be varied significantly. As shown in Figure 2-5, at low pyridine concentration (1% v/v), large phase separation can be clearly observed in the phase image of blend film and the film is very rough; while at high pyridine concentration (8% v/v), the film has small phase separated regions and it is much smoother. The EQE of the devices was strongly related with the roughness of the film. It was found that the highest EQE was obtained for devices containing the smoothest blend film. The smoothest film resulting from the smallest phase separation ensures the formation of large donor-acceptor

interface, which is beneficial for the charge transfer and separation between polymer and NCs. In addition, the processing solvent also can affect the organization of polymers. Sun *et al.* demonstrated that the performance of P3HT:CdSe NCs solar cells prepared from trichlorobenzene (TCB) was twice that of devices prepared from chloroform.<sup>38</sup> The higher efficiency is due to the organization of P3HT into fibrillar structures during the slow drying process of high boiling point TCB, which is good for charge transport.

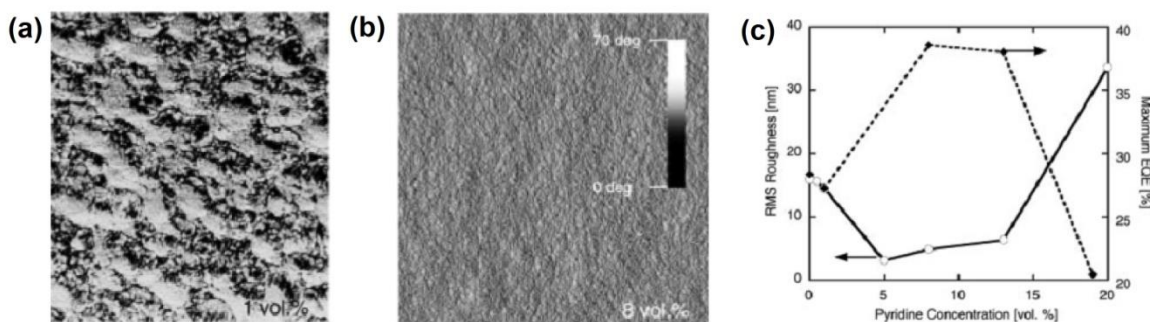


**Figure 2-5:** AFM phase images of P3HT and CdSe NCs blend films casted from (a) 1% v/v pyridine in chloroform and (b) 8% v/v pyridine in chloroform; surface roughness of P3HT and CdSe NCs blend films prepared from various concentration of pyridine in chloroform and the EQE of their corresponding devices (c). Images reproduced from the work done by Huynh *et al.*<sup>37</sup>

### 2.2.1 Geometry effect of nanocrystals

Quite different from BHJ organic solar cells, the performance of BHJ hybrid solar cells is not only affected by the morphology, but also affected by many other factors due to the complex interplay between conjugated polymer, ligand, and inorganic NCs. There are a few approaches designed to improve the efficiency of BHJ hybrid solar cells. Geometry control of NCs is one of them. It has been found that the size and shape of NCs can have a strong impact on the performance of HSCs.

Brandenburg *et al.* have compared the solar cells made of the blend of P3HT and quasi-spherical CdSe QDs with different sizes ( $< 5$  nm), and found that  $V_{oc}$  of devices could increase as high as 50% when smaller QDs were used.<sup>39</sup> It was because smaller QDs have larger bandgaps and high lying LUMO levels and  $V_{oc}$  of donor-acceptor BHJ solar cells is determined by the difference between the donor HOMO and the acceptor LUMO.<sup>40</sup> In general, the devices based on smaller particles yielded lower FF, which is compensated by the gain in  $V_{oc}$ . As a result, the PCE of devices was independent of the particles size. Similar conclusion was drawn by other groups.<sup>41</sup>

Shape of NCs has also been proven to influence the device efficiency of hybrid BHJ solar cells by many research groups. Typically, devices based on spherical QDs always show poor performance as the electron transport between nanoparticles via hopping mechanism could be difficult. Huynh *et al.* demonstrated that device based on P3HT and CdSe could perform significantly better when CdSe QDs were replaced with CdSe nanorods (NR). Figure 2-6 showed a comparison of the external quantum efficiency (EQE) of the devices with different CdSe NCs morphologies and the TEM images of a cross section of devices made of NCs with different morphologies.<sup>42</sup> It was found that the EQE signal increased as the aspect ratio of CdSe NCs increased from spherical shape to rod-like shape. Compared to spherical nanoparticles, the one-dimensional nanorods could improve band conduction and reduce hopping steps of electrons due to the extended physical structure, leading to a much reduced charge recombination in the photovoltaic devices. However, NCs with rod-like shape tend to lie in the plane of the blend film, resulting in better charge transport in the parallel direction with respect to the substrate; while vertical charge transport is preferred for solar cells. To overcome the problem, NCs with a terapod-shape was

proposed. Sun *et al.* have reported solar cells based on poly (p-phenylenvinylene) (PPV) derivative and CdSe tetrapods (TPs) could reach an efficiency of 2.8%, which is one the of highest reported performance for polymer/CdSe hybrid solar cells.<sup>43</sup> TEM study found that in such devices, CdSe tetrapods preferentially segregate at the top surface of the film, which is beneficial for efficient electron collection. In addition, hyberbranched CdSe NCs, which exhibit a dendritic structure with many branch points, are also blended with conjugated polymers to make BHJ hybrid solar cells. For example, Gur *et al.* reported hybrid solar cells using hyperbranched particles could show PCE up to 2.18%, which were better than those of nanorod based device.<sup>44</sup> These results show in general that inorganic nanocrystals with 3-D structures can form better percolation network for charge transport in hybrid solar cells.

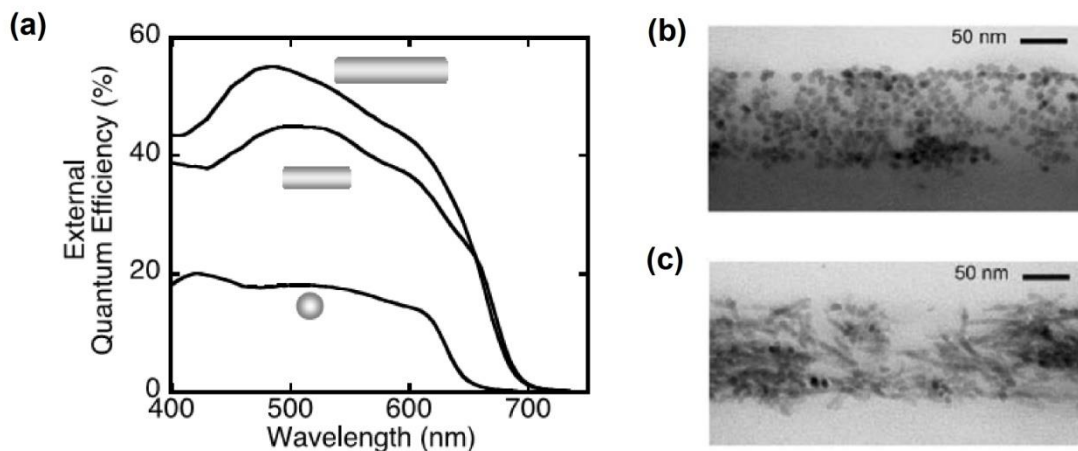


**Figure 2-6:** (a) EQE signals of devices based on P3HT and 7-nm-diameter CdSe NCs with length of 7 nm, 30 nm, 60 nm; TEM cross section images of blend films based on P3HT and CdSe NCs of (b) dot shape (c) rod shape. Images reproduced from the work done by Huynh *et al.*<sup>42</sup>

Although NRs and TPs have been proven to be capable to improve the device performance, in recent publications, it has been shown that spherical NCs need be reconsidered for the

application in BHJ hybrid solar cells. Yang *et al.* demonstrated that by simply using large spherical NCs (7.1 nm) treated with acid, devices based on PCPDTBT and CdSe could reach a high efficiency of 3.1%.<sup>41</sup> This study suggests that spherical NCs could possibly form good electron transport pathway in the blend film. In another study by Ren *et al.*, he showed that by carefully controlling the phase separation of polymer and spherical QDs, devices based on P3HT and CdS QDs could reach a PCE of 4.1%.<sup>45</sup>

### **2.2.2 Surface treatment of nanocrystals**

Many studies have shown that the performance of BHJ hybrid solar cells strongly depends on the capping ligand on the surface of NCs. It is because the dispersibility of NCs in solution and the miscibility of polymer and NCs are both controlled by the capping ligand. Besides, charge separation between NCs and polymers is also affected by the ligands. It is believed that the insulating long ligand (e.g. oleic acid, trioctylphosphine oxide) on the NC surface, which is used to prevent aggregation during NC synthesis, reduces the charge transport in the photoactive layer and limits the device performance of BHJ hybrid solar cells. Ginger *et al.* found the electron mobilities of thin films of spherical CdSe NCs covered with ligand trioctylphosphine oxide (TOPO) was only in the order of  $10^{-5} \text{ cm}^2 \text{V}^{-1} \text{s}^{-1}$ ; while the electron mobility of bulk CdSe film was in the order of  $10^2 \text{ cm}^2 \text{V}^{-1} \text{s}^{-1}$ .<sup>46</sup> In order to solve this issue, extensive studies have been done to modify the surface of NCs by exchanging the original insulating ligand with various short conducting ligands to promote charge transfer between polymer and NCs, as well as charge transport among the NCs. Greenham *et al.* investigated the photoluminescence (PL) quenching of polymer MEH-PPV by CdS NCs either covered by TOPO or pyridine.<sup>47</sup> They found that when TOPO was used, no PL quenching was observed; while significant quenching of PL signals was



observed when pyridine capped NCs were used. This implied charge transfer was much more efficient between polymer and NCs when TOPO was replaced with pyridine. Since then, pyridine is commonly used as capping ligand for improving device performance and many hybrid devices with high performance have been reported.<sup>42,48</sup> However, recently several ligands based on other small molecules have been reported to perform better than pyridine. Olson *et al.* have shown that butylamine (BA) may be a good candidate as effective ligand for NCs in hybrid solar cells, as the devices based on P3HT and butylamine treated CdSe NC exhibited a high PCE of 1.8%.<sup>49</sup> In another study, Greaney *et al.* demonstrated that the  $V_{oc}$  of P3HT:CdSe hybrid devices could be enhanced when capping ligand pyridine was replaced by tert-butylthiol (t-BT).<sup>50</sup> This was the result of raised LUMO level of CdSe NCs induced by tert-butylthiol. Besides, Seo *et al.* designed a thermally cleavable solubilizing ligand tert-butyl-N-(2-mercaptoethyl) carbamate to replace the typical initial ligand TOPO on CdSe NCs by ligand exchange and the modified CdSe NCs are then blended with P3HT to make hybrid solar cells.<sup>51</sup> Thermal annealing was later applied to reduce the length of the ligand in the hybrid films, resulting in a closer contact between the CdSe NCs and also between NCs and P3HT. As a result, the devices showed an improved efficiency due to the better charge transport. In addition, ligand exchange can be carried out not only for NCs in solution, but also for polymer/NC blend films. Wu *et al.* found that after benzenedithiol vapor treatment of P3HT/CdSe NRs devices, the PCE could increase from 1.56% to 2.65%.<sup>52</sup> Fu *et al.* demonstrated a highly efficient hybrid solar cells based on P3HT:CdSe QD could be achieved via film treatment with acetonitrile solution of n-butylthiol.<sup>53</sup>

Many studies have shown that ligand exchange on the surface of NCs cannot be 100% and the remaining long ligands can still be harmful for charge transport. Therefore, several other approaches have been developed. In their pioneering work, Zhou *et al.* established a non-ligand-exchanged method to bypass the predicament of ligand exchange, as shown in Figure 2-7a.<sup>54</sup> In this study, as-synthesized CdSe NCs covered with long ligand hexadecylamine (HDA) were first washed with hexanoic acid (HA) and then mixed with P3HT to make hybrid solar cells. It turned out solar cells based on non-ligand-exchanged CdSe NCs could perform very well. The authors proposed that during the acid treatment, the immobilized excess HDA on NCs forms a salt with the acid. In the end, the ligand shell on the NCs is effectively reduced in size, which is beneficial for charge transfer between P3HT and CdSe QDs, confirmed by the strong photoluminescence quenching. However, the “ideal” ligands for NCs are still elusive for high performance BHJ hybrid solar cells. To avoid ligand exchange, direct growth of NCs in polymer matrix without the presence of stabilizing ligand has been proposed.<sup>55,56</sup> The principle behind this is that conjugated polymers can act as the stabilizing agent for NCs. A good demonstration is shown by Liao *et al.*, who reported a device of PCE as high as 2.9% using P3HT and in-situ grown CdS nanorods (Figure 2-7b).<sup>57</sup> It is found that the aspect ratio of CdSe NRs could be well controlled using the P3HT polymer matrix by adjusting the ratio of the cosolvent mixture during synthesis. Long NRs well embedded in the P3HT phase can be prepared this way. This improves the interface and creates more percolated electron transport paths, both contributing to the high device performance. In another work, Leventis *et al.* introduced a low-temperature route to prepare in-situ grown NCs in polymer matrix for photovoltaic application.<sup>58</sup> The active layer consists of P3HT and Cd-xanthate-based precursor, which

can be transformed into P3HT/CdSe NCs composite simply by thermal treatment at 150°C. In the end, an interpenetrating network of CdS NCs in P3HT matrix was formed for photoactive layer, exhibiting high charge generation.

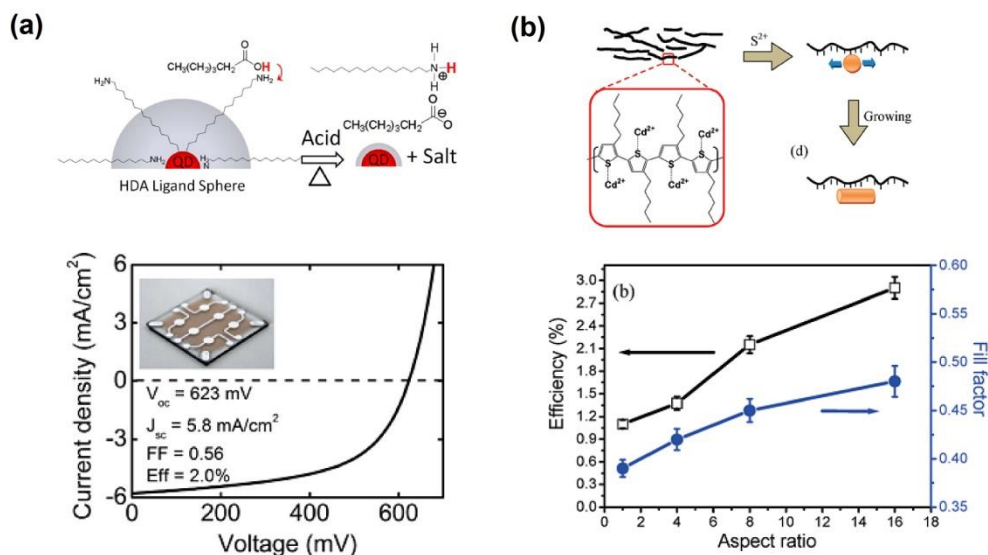


**Figure 2-7:** (a) *J-V* characteristic of devices based on P3HT and non-ligand-exchanged CdSe QDs; and the proposed QDs sphere model. (b) The dependence of device performance on the aspect ratio of CdS NCs grown in P3HT; and the proposed synthesis scheme of CdS NCs grown in P3HT matrix. Images reproduced from the works done by Zhou *et al.*<sup>54</sup> and Liao *et al.*<sup>57</sup>

### 2.2.3 Functionalization of polymers

As we have seen so far, to ensure efficient exciton dissociation in hybrid solar cells, polymer and NCs must be in close contact, as charge transfer is a very short-range interaction. Besides replacing long ligand with short ligand on the surface of NCs to reduce the distance between polymer and NCs, functionalizing the polymer with ligand moieties (e.g. amine group, thiol group) is another promising approach. Skaff *et al.* have demonstrated that the ligand on CdSe NCs could act as the initiator for the polymerization

of poly(para-phenylene vinylene) (PPV) and achieved a polymer-NC composite with uniform dispersion of NCs.<sup>59</sup> In another approach, the Lin group has shown polymer P3HT can be directly grafted onto the surface of CdSe NCs via the Heck reaction of vinyl-terminated P3HT with the capping ligand arylbromide-functionalized phosphine oxides or thiols. (Figure 2-8a)<sup>60,61</sup> The devices made by the functionalized polymer and NCs have also been studied. Liu *et al.* have shown devices based on amine-functionalized P3HT and pyridine-capped CdSe NRs could exhibit a PCE of 1.4%.<sup>62</sup> The functionalized group enables intimate contact between CdSe NCs and P3HT via covalent interactions and enhances the miscibility between the two components; resulting a favorable morphology for charge transport even at a low loading of NCs. The effect of functional end-group of the polymer on device performance have been reported by Palaniappan *et al.*<sup>63</sup> They found that compared to standard devices based on P3HT and CdSe QDs, devices based on thiol-terminated P3HT and CdSe QDs can show better performance. Very recently, it is found that by using the unique self-assembly nature of conjugated polymers, co-axial nanostructure based on functionalized polymer and inorganic NCs can be created. Such hybrid composite is beneficial both for charge generation and charge transport.<sup>64</sup> For example, Pentzer *et al.* have shown CdSe QDs can reside nicely around the wire edges of P3HT nanofibrils after solution assembly, forming a unique well-organized nanocomposite good both for electron and hole transport (Figure 2-8b).<sup>65</sup> However, devices based on such hybrid composites have not been reported yet up to date.

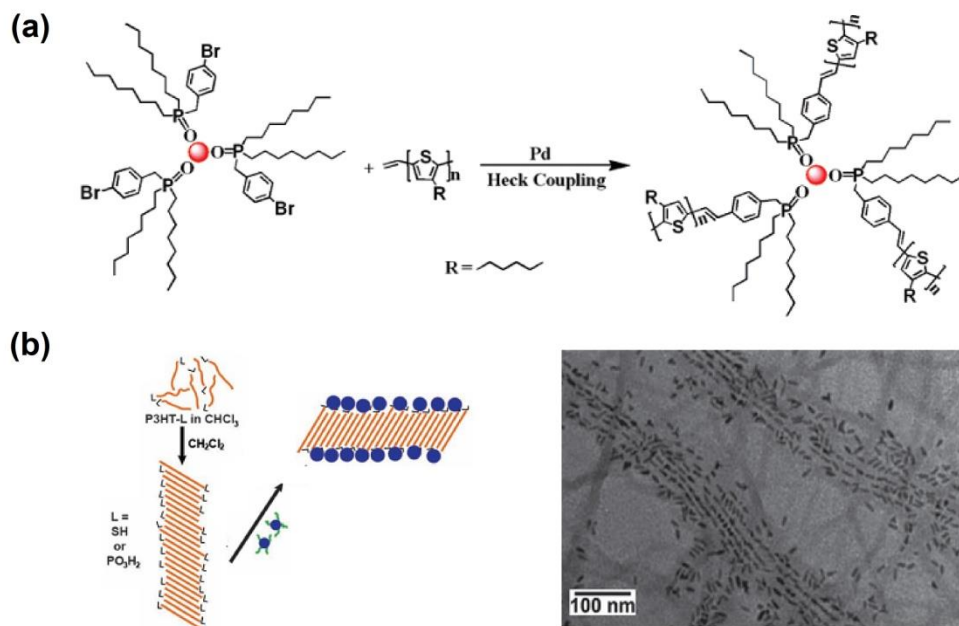


**Figure 2-8:** (a) Synthetic scheme of grafting vinyl-terminated P3HT onto DOPO-Br functionalized CdSe QDs (b) Schematic drawing of the formation of P3HT/CdSe QDs nanocomposites and representative TEM images of P3HT/CdSe QDs nanocomposites. Images reproduced from the works done by Xu *et al.*<sup>60</sup> and Pentzer *et al.*<sup>65</sup>

## 2.3 Bilayer Hybrid Solar Cells

In the previous section, the development and the challenge of BHJ hybrid solar cells based on inorganic nanocrystals (NCs) have been reviewed. Due to the complex interplay between conjugated polymer, ligands and NCs, the morphology of BHJ hybrid solar cells are unoptimized and their performance are mainly limited by the charge transport issue which is common in BHJ, as well as charge transfer issue especially for hybrid solar cells. Thus, bilayer configuration is also considered as a possibility for high performance hybrid solar cells. As discussed earlier, solar cells in bilayer architecture are limited by the low charge carrier generation, which results from the small donor/acceptor interfacial areas.

Nevertheless, the distinct and continuous phase domains ensure the efficient charge transport of both electrons and holes in the photoactive layer, minimizing the recombination of charge carriers. In general, the adverse effect of poor charge generation outweighs the benefit of good charge transport for bilayer solar cell. If low charge generation due to lack of interface area can be positively compensated by increasing the number of excitons reaching the interface for dissociation to happen, the bilayer solar cell has the potential to perform very well. The challenge of delicate morphology control of hybrid solar cells in BHJ structure can be circumvented. Currently, two approaches may be used to realize such objective. One is to focus on increasing the number of excitons generated per photon absorbed; the other is to enhance the excitonic diffusion length of the absorber to generate more free charges at the interface.

### **2.3.1 Exciton multiplication**

To overcome the drawback of low photocurrent generation in bilayer solar cells, one way is to amplify the number of charge carriers through more efficient utilization of absorbed photons. This may be achieved by using of two optical phenomena in hybrid solar cells: multiple exciton generation (MEG) in inorganic nanocrystals and singlet exciton fission (SEF) in organic materials. MEG is a process that takes place in semiconductor NCs, where more than one electron-hole pairs could be generated for every photon absorbed due to impact ionization.<sup>66</sup> In this process, the excess energy of hot electrons created in the NCs is used to excite another electron across the bandgap rather than thermalizing. MEG was first demonstrated in PbSe QDs in 2004<sup>67</sup> and over the next few years, a range of materials in different nanocrystal types, such as PbS,<sup>68</sup> CdSe<sup>69</sup> and PbTe,<sup>70</sup> was also observed to

show MEG effect. It is believed that as two or more excitons per single absorbed photons can be created in MEG based solar cells and higher production of free charge carrier in the solar cells can be obtained. Recently, Semonin *et al.* have demonstrated that due to the MEG effect in PbSe QDs based solar cells, the peak EQE signal of the devices can exceeded 100% and their corresponding photocurrent was also enhanced.<sup>71</sup> In a separate study, Qi *et al.* claimed that the MEG kinetic was observed in MEH-PPV:PbSe device, evident with an EQE up to 150% at negative biases.<sup>72</sup> However, hybrid solar cell with reasonable efficiency due to MEG effect has not been reported up to date.

An alternative approach to improve the utilization efficiency of absorbed photons for bilayer solar cell can be achieved through singlet exciton fission (SEF) in organic materials. SEF is a process happening in organic semiconductor, whereby pairs of triplets are generated from singlet excitons.<sup>73</sup> Up to date, pentacene is the most studied material for SEF effect as singlet fission in pentacene is ultrafast compared to the other decay processes.<sup>74</sup> Besides, it has been shown by many groups that bilayer organic solar cells based on pentacene, which has a excitonic diffusion length of about 70 nm,<sup>75</sup> can exhibit high external and internal quantum efficiency.<sup>76,77</sup> Recently, the group from Greenham demonstrated that hybrid bilayer solar cell based on pentacene and PbS nanocrystals (NCs) can have a PCE of 1%, with internal quantum efficiency (IQE) exceeding 50%.<sup>78</sup> The device structure and energy diagram are shown in Figure 2-9. It has been identified that triplet excitons created by singlet fission in pentacene can dissociate at the organic-inorganic interface and generate additional photocurrent. Nevertheless, at present, solar cells based on singlet fission are in their infancy and further investigation is needed to understand and optimize the operation of such devices.

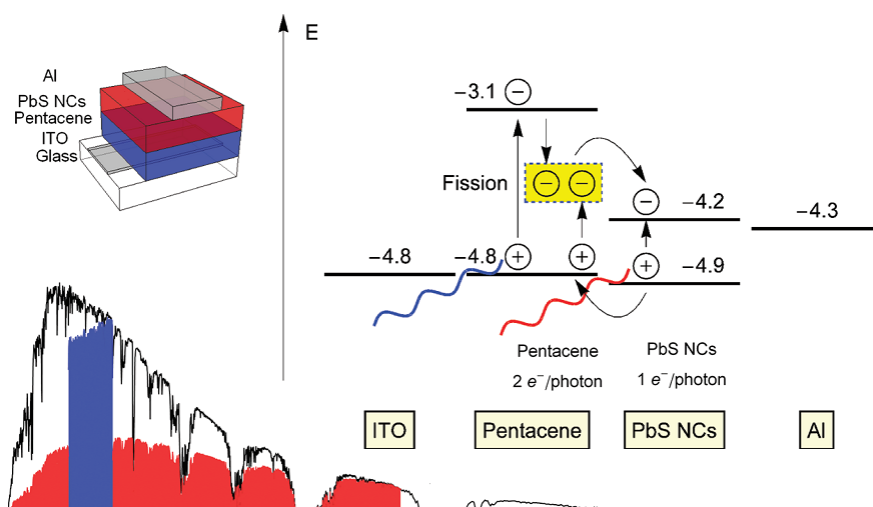


**Figure 2-9:** Device structure and energy diagram of solar cells based on bilayer device of ITO/Pentacene/PbS/Al. The absorption region of device in respective of solar spectrum and proposed working mechanism is also included. Images reproduced from the work done by Ehrler *et al.*<sup>78</sup>

### 2.3.2 Materials with long exciton diffusion length

The performance of hybrid solar cells are strongly dependent the exciton diffusion in the photoactive materials. If a material with high exciton diffusion length is used as light absorber, thick film can be constructed for increased in light absorption without the disadvantage of more photoexcited excitons not being able to reach the interface, thus both charge generation and device performance can be improved. Recently, hybrid material organolead halides (e.g.  $\text{CH}_3\text{NH}_3\text{PbX}_3$ , X = halogen) have been synthesized and was found to be highly suitable for application in solar cells as they have excellent intrinsic optoelectronic properties – they have a direct bandgap, large absorption coefficient and high carrier mobility.<sup>79,80</sup> It has been found that semiconductor organolead halides have a perovskite crystal structure ( $\text{ABX}_3$ ), therefore they are more commonly referred as perovskites in the literatures. Optical, electronic, and mechanical properties of perovskites



can be easily tailored by varying the organic and inorganic components.<sup>81,82</sup> For example, Noh *et al.* have demonstrated that the bandgap of  $\text{CH}_3\text{NH}_3\text{PbX}_3$  could be fine-tuned by changing the chemical composition of the material, resulting in a range of device performance and stability.<sup>83</sup> In addition, perovskites are ambipolar, which means they can transport both electrons and holes. For instance, Lee *et al.* demonstrated that  $\text{CH}_3\text{NH}_3\text{PbI}_2\text{Cl}$  in the  $\text{CH}_3\text{NH}_3\text{PbI}_2\text{Cl}$ /spiro-OMeTAD bilayer solar cell could work as a light absorber and an electron conductor simultaneously.<sup>84</sup> While Etgar *et al.* demonstrated that when  $\text{CH}_3\text{NH}_3\text{PbI}_3$  is used in conjunction with a compact  $\text{TiO}_2$  layer,  $\text{CH}_3\text{NH}_3\text{PbI}_3$  can act as a light harvester and transport holes as well in the  $\text{CH}_3\text{NH}_3\text{PbI}_3/\text{TiO}_2$  bilayer solar cells.<sup>85</sup> This interesting attribute can make perovskite be coupled with a range of n-type and p-type organic semiconductors for photovoltaic application. Perovskites were originally used as light absorber in dye-sensitized solar cells (DDSC), which contain complex nanostructure of metal oxide as the photoanode. Very recently, it has been shown that perovskites are capable of working well in the simplest architecture – bilayer device structure. For example, Etgar *et al.*  $\text{CH}_3\text{NH}_3\text{PbI}_3/\text{TiO}_2$  heterojunction solar cells based on thick compact  $\text{TiO}_2$  layer can achieve a PCE of 5.5%, which is a new high record for bilayer solar cells.<sup>85</sup> In another study, Jeng *et al.* demonstrated that bilayer solar cells based on perovskite  $\text{CH}_3\text{NH}_3\text{PbI}_3$  and various organic fullerene molecules ( $\text{C}_{60}$ ,  $\text{PC}_{61}\text{BM}$  and ICBA) could exhibit PCE between 2% and 4%, too.<sup>86</sup> (Figure 2-10) Therefore, more attention should be paid to bilayer solar cells based on perovskites, which are promising to achieve high performance at low cost.

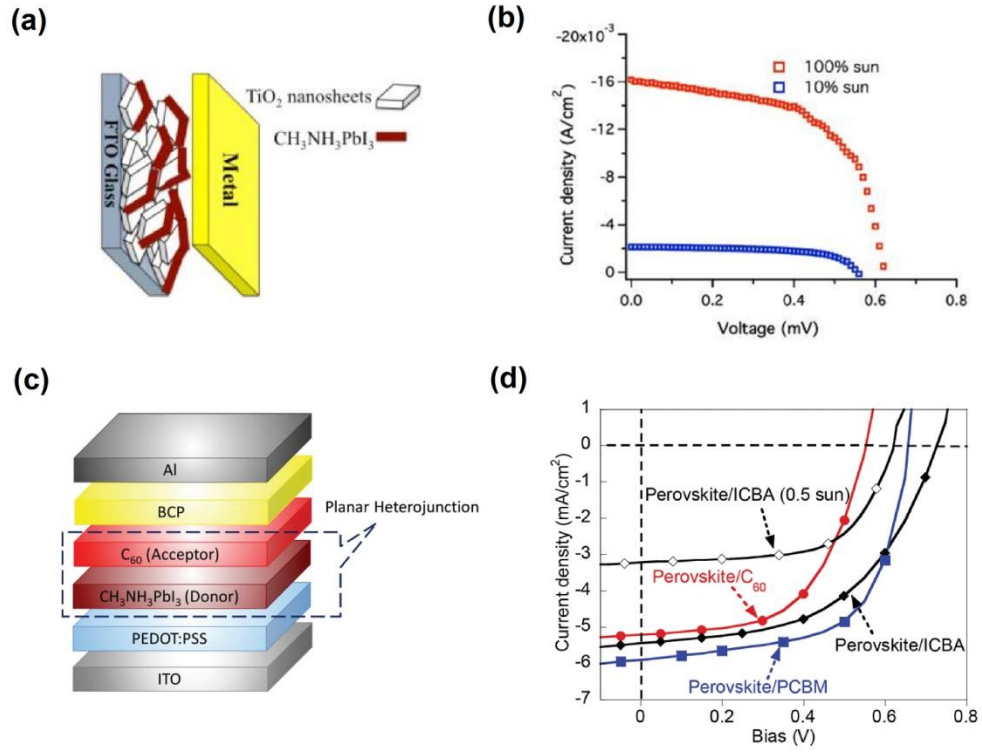


**Figure 2-10:** (a) Device structure and (b)  $J$ - $V$  characteristic of bilayer solar cells based on perovskite/TiO<sub>2</sub>; (c) Device structure and (d)  $J$ - $V$  curves of bilayer solar cells based on perovskite/fullerene. Images reproduced from the works done by Etgar *et al.*<sup>85</sup> and by Jeng *et al.*<sup>86</sup>

## 2.4 References

- (1) International Energy Agency **2011**.
- (2) International Energy Agency **2013**.
- (3) Chapin, D. M.; Fuller, C. S.; Pearson, G. L. *J. Appl. Phys.* **1954**, 25, 676.
- (4) Green, M. A.; Emery, K.; Hishikawa, Y.; Warta, W.; Dunlop, E. D. *Progress in Photovoltaics: Research and Applications* **2013**, 21, 827.
- (5) Hardin, B. E.; Snaith, H. J.; McGehee, M. D. *Nat Photon* **2012**, 6, 162.
- (6) Zhang, M.; Gu, Y.; Guo, X.; Liu, F.; Zhang, S.; Huo, L.; Russell, T. P.; Hou, J. *Advanced Materials* **2013**, 25, 4944.
- (7) Liu, Z.; Sun, Y.; Yuan, J.; Wei, H.; Huang, X.; Han, L.; Wang, W.; Wang, H.; Ma, W. *Advanced Materials* **2013**, 25, 5772.
- (8) Skompska, M. *Synthetic Metals* **2010**, 160, 1.
- (9) Steim, R.; Ameri, T.; Schilinsky, P.; Waldauf, C.; Dennler, G.; Scharber, M.; Brabec, C. J. *Solar Energy Materials and Solar Cells* **2011**, 95, 3256.
- (10) Bao, Z.; Lovinger, A. J.; Dodabalapur, A. *Applied Physics Letters* **1996**, 69, 3066.
- (11) Bozano, L.; Carter, S. A.; Scott, J. C.; Malliaras, G. G.; Brock, P. J. *Applied Physics Letters* **1999**, 74, 1132.
- (12) Sirringhaus, H.; Tessler, N.; Friend, R. H. *Science* **1998**, 280, 1741.
- (13) Babel, A.; Jenekhe, S. A. *Advanced Materials* **2002**, 14, 371.
- (14) Yu, G.; Zhang, C.; Heeger, A. J. *Applied Physics Letters* **1994**, 64, 1540.
- (15) Miranda, P. B.; Moses, D.; Heeger, A. J. *Physical Review B* **2001**, 64, 081201.
- (16) Tang, C. W. *Applied Physics Letters* **1986**, 48, 183.
- (17) Brédas, J.-L.; Norton, J. E.; Cornil, J.; Coropceanu, V. *Accounts of Chemical Research* **2009**, 42, 1691.
- (18) Barth, S.; Bäessler, H. *Physical Review Letters* **1997**, 79, 4445.
- (19) Halls, J. J. M.; Pichler, K.; Friend, R. H.; Moratti, S. C.; Holmes, A. B. *Applied Physics Letters* **1996**, 68, 3120.
- (20) Halls, J. J. M.; Cornil, J.; dos Santos, D. A.; Silbey, R.; Hwang, D. H.; Holmes, A. B.; Brédas, J. L.; Friend, R. H. *Physical Review B* **1999**, 60, 5721.
- (21) Savoie, B. M.; Jackson, N. E.; Marks, T. J.; Ratner, M. A. *Physical Chemistry Chemical Physics* **2013**, 15, 4538.

- (22) Yu, G.; Gao, J.; Hummelen, J. C.; Wudl, F.; Heeger, A. J. *Science* **1995**, 270, 1789.
- (23) Greene, L. E.; Law, M.; Tan, D. H.; Montano, M.; Goldberger, J.; Somorjai, G.; Yang, P. *Nano Letters* **2005**, 5, 1231.
- (24) Snaith, H. J.; Whiting, G. L.; Sun, B.; Greenham, N. C.; Huck, W. T. S.; Friend, R. H. *Nano Letters* **2005**, 5, 1653.
- (25) Shao, S.; Zheng, K.; Zidek, K.; Chabera, P.; Pullerits, T.; Zhang, F. *Solar Energy Materials and Solar Cells* **2013**, 118, 43.
- (26) Serap, G.; Nenad, M.; Jovan, M. N.; Niyazi Serdar, S. *Nanotechnology* **2008**, 19, 424009.
- (27) Lokteva, I.; Radychev, N.; Witt, F.; Borchert, H.; Parisi, J. r.; Kolny-Olesiak, J. *The Journal of Physical Chemistry C* **2010**, 114, 12784.
- (28) Liu, X.; Jiang, Y.; Lan, X.; Zhang, Y.; Liu, C.; Li, J.; Wang, B.; Yu, Y.; Wang, W. *physica status solidi (a)* **2012**, 209, 1583.
- (29) Verma, D.; Ranga Rao, A.; Dutta, V. *Solar Energy Materials and Solar Cells* **2009**, 93, 1482.
- (30) Günes, S.; Fritz, K. P.; Neugebauer, H.; Sariciftci, N. S.; Kumar, S.; Scholes, G. D. *Solar Energy Materials and Solar Cells* **2007**, 91, 420.
- (31) Sharma, S. N.; Mehta, A.; Kumar, U.; Chand, S. *Physica E: Low-dimensional Systems and Nanostructures* **2014**, 57, 103.
- (32) Beek, W. J. E.; Wienk, M. M.; Janssen, R. A. J. *Advanced Materials* **2004**, 16, 1009.
- (33) Liao, H.-C.; Lee, C.-H.; Ho, Y.-C.; Jao, M.-H.; Tsai, C.-M.; Chuang, C.-M.; Shyue, J.-J.; Chen, Y.-F.; Su, W.-F. *Journal of Materials Chemistry* **2012**, 22, 10589.
- (34) Cui, D.; Xu, J.; Zhu, T.; Paradee, G.; Ashok, S.; Gerhold, M. *Applied Physics Letters* **2006**, 88, 183111.
- (35) Zhou, Y.; Eck, M.; Kruger, M. *Energy & Environmental Science* **2010**, 3, 1851.
- (36) Jo, J.; Na, S.-I.; Kim, S.-S.; Lee, T.-W.; Chung, Y.; Kang, S.-J.; Vak, D.; Kim, D.-Y. *Advanced Functional Materials* **2009**, 19, 2398.
- (37) Huynh, W. U.; Dittmer, J. J.; Libby, W. C.; Whiting, G. L.; Alivisatos, A. P. *Advanced Functional Materials* **2003**, 13, 73.
- (38) Sun, B.; Greenham, N. C. *Physical Chemistry Chemical Physics* **2006**, 8, 3557.

- (39) Brandenburg, J. E.; Jin, X.; Kruszynska, M.; Ohland, J.; Kolny-Olesiak, J.; Riedel, I.; Borchert, H.; Parisi, J. *J. Appl. Phys.* **2011**, *110*, 064509.
- (40) Scharber, M. C.; Mühlbacher, D.; Koppe, M.; Denk, P.; Waldauf, C.; Heeger, A. J.; Brabec, C. J. *Advanced Materials* **2006**, *18*, 789.
- (41) Yang, J.; Tang, A.; Zhou, R.; Xue, J. *Solar Energy Materials and Solar Cells* **2011**, *95*, 476.
- (42) Huynh, W. U.; Dittmer, J. J.; Alivisatos, A. P. *Science* **2002**, *295*, 2425.
- (43) Sun, B.; Snaith, H. J.; Dhoot, A. S.; Westenhoff, S.; Greenham, N. C. *J. Appl. Phys.* **2005**, *97*, 014914.
- (44) Gur, I.; Fromer, N. A.; Chen, C.-P.; Kanaras, A. G.; Alivisatos, A. P. *Nano Letters* **2006**, *7*, 409.
- (45) Ren, S.; Chang, L.-Y.; Lim, S.-K.; Zhao, J.; Smith, M.; Zhao, N.; Bulović, V.; Bawendi, M.; Gradečak, S. *Nano Letters* **2011**, *11*, 3998.
- (46) Rode, D. L. *Physical Review B* **1970**, *2*, 4036.
- (47) Greenham, N. C.; Peng, X.; Alivisatos, A. P. *Physical Review B* **1996**, *54*, 17628.
- (48) Celik, D.; Krueger, M.; Veit, C.; Schleiermacher, H. F.; Zimmermann, B.; Allard, S.; Dumsch, I.; Scherf, U.; Rauscher, F.; Niyamakom, P. *Solar Energy Materials and Solar Cells* **2012**, *98*, 433.
- (49) Olson, J. D.; Gray, G. P.; Carter, S. A. *Solar Energy Materials and Solar Cells* **2009**, *93*, 519.
- (50) Greaney, M. J.; Das, S.; Webber, D. H.; Bradforth, S. E.; Brutchey, R. L. *ACS Nano* **2012**, *6*, 4222.
- (51) Seo, J.; Kim, W. J.; Kim, S. J.; Lee, K.-S.; Cartwright, A. N.; Prasad, P. N. *Applied Physics Letters* **2009**, *94*, 133302.
- (52) Wu, Y.; Zhang, G. *Nano Letters* **2010**, *10*, 1628.
- (53) Fu, W.; Shi, Y.; Qiu, W.; Wang, L.; Nan, Y.; Shi, M.; Li, H.; Chen, H. *Physical Chemistry Chemical Physics* **2012**, *14*, 12094.
- (54) Zhou, Y.; Riehle, F. S.; Yuan, Y.; Schleiermacher, H.-F.; Niggemann, M.; Urban, G. A.; Krüger, M. *Applied Physics Letters* **2010**, *96*, 013304.
- (55) Dayal, S.; Kopidakis, N.; Olson, D. C.; Ginley, D. S.; Rumbles, G. *Journal of the American Chemical Society* **2009**, *131*, 17726.

- (56) De Girolamo, J.; Reiss, P.; Pron, A. *The Journal of Physical Chemistry C* **2007**, *111*, 14681.
- (57) Liao, H.-C.; Chen, S.-Y.; Liu, D.-M. *Macromolecules* **2009**, *42*, 6558.
- (58) Leventis, H. C.; King, S. P.; Sudlow, A.; Hill, M. S.; Molloy, K. C.; Haque, S. A. *Nano Letters* **2010**, *10*, 1253.
- (59) Skaff, H.; Sill, K.; Emrick, T. *Journal of the American Chemical Society* **2004**, *126*, 11322.
- (60) Xu, J.; Wang, J.; Mitchell, M.; Mukherjee, P.; Jeffries-El, M.; Petrich, J. W.; Lin, Z. *Journal of the American Chemical Society* **2007**, *129*, 12828.
- (61) Zhao, L.; Pang, X.; Adhikary, R.; Petrich, J. W.; Jeffries-El, M.; Lin, Z. *Advanced Materials* **2011**, *23*, 2844.
- (62) Liu, J.; Tanaka, T.; Sivula, K.; Alivisatos, A. P.; Fréchet, J. M. J. *Journal of the American Chemical Society* **2004**, *126*, 6550.
- (63) Palaniappan, K.; Murphy, J. W.; Khanam, N.; Horvath, J.; Alshareef, H.; Quevedo-Lopez, M.; Biewer, M. C.; Park, S. Y.; Kim, M. J.; Gnade, B. E.; Stefan, M. C. *Macromolecules* **2009**, *42*, 3845.
- (64) Bokel, F. A.; Sudeep, P. K.; Pentzer, E.; Emrick, T.; Hayward, R. C. *Macromolecules* **2011**, *44*, 1768.
- (65) Pentzer, E. B.; Bokel, F. A.; Hayward, R. C.; Emrick, T. *Advanced Materials* **2012**, *24*, 2254.
- (66) Beard, M. C.; Luther, J. M.; Semonin, O. E.; Nozik, A. J. *Accounts of Chemical Research* **2012**, *46*, 1252.
- (67) Schaller, R. D.; Klimov, V. I. *Physical Review Letters* **2004**, *92*, 186601.
- (68) Stewart, J. T.; Padilha, L. A.; Qazilbash, M. M.; Pietryga, J. M.; Midgett, A. G.; Luther, J. M.; Beard, M. C.; Nozik, A. J.; Klimov, V. I. *Nano Letters* **2011**, *12*, 622.
- (69) Schaller, R. D.; Petruska, M. A.; Klimov, V. I. *Applied Physics Letters* **2005**, *87*, 253102.
- (70) Murphy, J. E.; Beard, M. C.; Norman, A. G.; Ahrenkiel, S. P.; Johnson, J. C.; Yu, P.; Mićić, O. I.; Ellingson, R. J.; Nozik, A. J. *Journal of the American Chemical Society* **2006**, *128*, 3241.

- (71) Semonin, O. E.; Luther, J. M.; Choi, S.; Chen, H.-Y.; Gao, J.; Nozik, A. J.; Beard, M. C. *Science* **2011**, *334*, 1530.
- (72) Qi, D.; Fischbein, M.; Drndić, M.; Šelmić, S. *Applied Physics Letters* **2005**, *86*, 093103.
- (73) Smith, M. B.; Michl, J. *Chemical Reviews* **2010**, *110*, 6891.
- (74) Lee, J.; Jadhav, P.; Reusswig, P. D.; Yost, S. R.; Thompson, N. J.; Congreve, D. N.; Hontz, E.; Van Voorhis, T.; Baldo, M. A. *Accounts of Chemical Research* **2013**, *46*, 1300.
- (75) Yoo, S.; Potscavage, W. J.; Domercq, B.; Han, S.-H.; Levi, D.; Kippelen, B. *MRS Online Proceedings Library* **2006**, *965*, null.
- (76) Yoo, S.; Potscavage Jr, W. J.; Domercq, B.; Han, S.-H.; Li, T.-D.; Jones, S. C.; Szoszkiewicz, R.; Levi, D.; Riedo, E.; Marder, S. R.; Kippelen, B. *Solid-State Electronics* **2007**, *51*, 1367.
- (77) Yoo, S.; Domercq, B.; Kippelen, B. *Applied Physics Letters* **2004**, *85*, 5427.
- (78) Ehrler, B.; Wilson, M. W. B.; Rao, A.; Friend, R. H.; Greenham, N. C. *Nano Letters* **2012**, *12*, 1053.
- (79) Heo, J. H.; Im, S. H.; Noh, J. H.; Mandal, T. N.; Lim, C.-S.; Chang, J. A.; Lee, Y. H.; Kim, H.-j.; Sarkar, A.; NazeeruddinMd, K.; Gratzel, M.; Seok, S. I. *Nat Photon* **2013**, *7*, 486.
- (80) Etgar, L.; Gao, P.; Xue, Z.; Peng, Q.; Chandiran, A. K.; Liu, B.; Nazeeruddin, M. K.; Grätzel, M. *Journal of the American Chemical Society* **2012**, *134*, 17396.
- (81) Mitzi, D. B.; Feild, C. A.; Harrison, W. T. A.; Guloy, A. M. *Nature* **1994**, *369*, 467.
- (82) Kagan, C. R.; Mitzi, D. B.; Dimitrakopoulos, C. D. *Science* **1999**, *286*, 945.
- (83) Noh, J. H.; Im, S. H.; Heo, J. H.; Mandal, T. N.; Seok, S. I. *Nano Letters* **2013**, *13*, 1764.
- (84) Lee, M. M.; Teuscher, J.; Miyasaka, T.; Murakami, T. N.; Snaith, H. J. *Science* **2012**, *338*, 643.
- (85) Etgar, L.; Gao, P.; Xue, Z.; Peng, Q.; Chandiran, A. K.; Liu, B.; Nazeeruddin, M. K.; Grätzel, M. *J. Am. Chem. Soc.* **2012**, *134*, 17396.
- (86) Jeng, J.-Y.; Chiang, Y.-F.; Lee, M.-H.; Peng, S.-R.; Guo, T.-F.; Chen, P.; Wen, T.-C. *Adv. Mater.* **2013**, *25*, 3727.





# Chapter 3

---

**P3HT:CdSe BHJ Solar Cells**

### 3.1 Introduction

Solar cells provide a possible solution to the global energy crisis with minimum environmental impact by directly converting sunlight into electricity. Among all the existing photovoltaic technologies developed so far, solution-processed organic/hybrid solar cells are particularly appealing because they can be fabricated on large flexible substrates at low temperature and hence keep the production cost of the solar cells low. Hybrid solar cells (HSCs) work in the same way as organic solar cells (OSCs), where conjugated molecules work as both light absorber and electron donor. Generally, they only differ by the material used for the electron acceptor: in OSCs, fullerene derivatives are commonly chosen as the electron-accepting material; while inorganic semiconducting nanocrystal (NCs) are used as the electron acceptor in HSCs. There are several advantages in replacing fullerene derivatives with inorganic NCs for photovoltaic application: (1) Devices can have broader absorption spectrum as NCs with well-tuned bandgap can contribute to different ranges of light absorption.<sup>1,2</sup> (2) As inorganic NCs have higher dielectric constant, charge transfer in the blend system can be better due to the decrease in coulombic interactions between electrons and holes.<sup>3</sup> (3) Devices can potentially have better charge transport since inorganic semiconductors possess larger electron mobility.<sup>4,5</sup> (4) Device can have longer lifetime as inorganic NCs have much better chemical stability.<sup>6</sup>

Various inorganic semiconducting nanocrystals (NCs) have been employed as electron acceptors for HSCs, such as cadmium sulfide (CdS), cadmium selenide (CdSe), cadmium telluride (CdTe), lead sulfide (PbS), lead selenide (PbSe), titania oxide (TiO<sub>2</sub>), and zinc oxide (ZnO).<sup>7-11</sup> Among them, CdSe is one of the most widely studied colloidal inorganic

NCs so far. It has been reported that HSCs based on low bandgap conjugated polymer and CdSe NCs could achieve a PCE as high as 3.6%.<sup>12</sup> In general, high quality inorganic NCs for HSCs application are synthesized via hot coordinating/non-coordinating solvents method, which are always passivated by organic surfactants. These surfactant ligands have long bulky alkyl chains (e.g. trioctylphosphine oxide), which are essential for the synthesis and beneficial in preventing the agglomeration of NCs in the solution. Nevertheless, they can act as insulating barriers to hinder charge transfer between NCs and conjugated polymers, and charge transport between NCs. As a result, surface modification (i.e ligand exchange) of NCs by replacing the original ligands with small molecules must be carried out first before they are incorporated into HSCs. The enhancement in the physical contact eventually leads to better electronic properties of the blend film and higher device performance. Although ligands are of paramount importance for HSCs, but to date, which material is considered to be an ideal ligand is unknown because of the conflicting requirements. Currently, amine based ligands are commonly adopted for post-synthesis treatment of NCs in solution prior to their application in HSCs and these devices have shown decent performance. Although in most work, pyridine is selected as the capping ligand for colloidal NCs,<sup>13-16</sup> some groups suggested that butylamine may be a more effective ligand as it will induce fewer hole traps on inorganic NCs after surface modification.<sup>17,18</sup> Therefore, butylamine-capped CdSe NCs were chosen for the study of solution-processed HSCs in this work.

For the state-of-the-art HSCs, colloidal inorganic NCs are often blended with conjugated polymer to construct the photoactive layers; as a result these cells are referred to as bulk heterojunction (BHJ) HSCs. The adoption of BHJ can overcome the limitation of short

diffusion lengths (*ca.* 10 nm) in conjugated polymers,<sup>19-21</sup> hence increase the amount of photogenerated excitons (i.e. bounded electron-hole pairs) reaching the donor-acceptor (D-A) interface, and improve charge generation in these solar cells. High performance solution-processed HSCs are all BHJ based at the moment. Nonetheless, isolated domains of donor and/or acceptor tend to form in the blend film, which hampers charge transport and collection in HSCs. Thus, numerous approaches have been developed to manipulate the morphology of the blend film in order to achieve an interdigitated D-A configuration with suitable domain size. In such an ideal morphology, the whole photovoltaic process is expected to be efficient. However, morphology control is very challenging for HSCs in practical. There is always a lack of percolation paths for charge transport in the photoactive layer of HSCs, resulting from the poor miscibility of the blend components due to the different nature in the materials used and the poor dispersion stability of NCs after ligand exchange in solution.

One of the common ways to enhance charge transport in the blend film is by increasing anisotropy in the shape of NCs. It has been reported that HSCs based on spherical CdSe NCs (i.e. quantum dots) can only achieve a PCE of 0.25%.<sup>22</sup> The low performance was attributed to inefficient electron transport between adjacent NCs via hopping mechanism. In comparison, when nanorods (NRs) CdSe was adopted, device efficiency could be increased to 1.7%.<sup>14</sup> It is because one-dimensional (1-D) NRs can reduce electron hopping steps during charge transport due to their extended physical structure. However, NRs tend to lie parallel to the substrate surface which is beneficial for charge transport parallel to the film; while vertical charge transport in the film is preferred for solar cells. To solve this issue, tetrapod NCs (TD) was later introduced into HSCs. It was found that

HSCs based on CdSe TDs could reach an efficiency of 2.8%.<sup>23</sup> So far, TP is considered as the best structure for inorganic NCs when they are applied in HSCs. However, two problems are associated with NCs in complex structure. First, their synthesis becomes more complicated. Second, their stability in the solution will be reduced due to the enhanced dipole-dipole interaction, which is not good for obtaining an optimal organization of NCs in the blend.

Another strategy to improve charge transport in HSCs is to utilize the self-assembly capability of conjugated polymer to control the thin film morphology of the hybrid blend at nanoscale level. Two levels of molecular organization may be achieved. Similar to colloidal NRs, the application of self-assembled polymer nanofiber in HSCs can create a more ordered morphology and provide directional transport in the first place. In addition, assembled polymer nanofibers may act as soft templates for NCs to “graft” onto; together they can form organized hybrid composites bearing a core-shell nanostructure, which is beneficial for both for charge generation and charge transport. Semi-crystalline conjugated polymer poly(3-hexylthiophene)s (P3HT), one of the most widely applied donor materials for organic/hybrid solar cells due to the combination of good optoelectronic properties, facile processability, and environmental stability,<sup>24</sup> which is also well known for its self-organization both in thin film and solution, can be a good candidate for the study of nanomorphology control. For instance, after thermal annealing, the crystallinity level and the hole mobility of P3HT in the photoactive layer of organic/hybrid solar cells were significantly improved due to the reorganization of the polymer molecules.<sup>25</sup> In recent years, preassembling P3HT into nanofibers in the solution has attracted a lot of attention as it can achieve a high degree of molecular order in P3HT

at low temperature, which is suitable for application in flexible solar cells.<sup>26-28</sup> It has been reported that the incorporation of preassembled P3HT nanofiber in OSCs can yield efficiency up to 3%.<sup>26</sup> However, little study has been done to investigate the application of P3HT nanofiber in HSCs.

An important characteristic of assembled P3HT nanofiber is that its fiber width is *ca.* 20 nm, which is about twice the distance of its exciton diffusion length. Such molecular nanostructure can guarantee almost all the excitons generated inside of P3HT molecules reach the D-A interface if hybrid composites are prepared based on it. However, alkyl chains of P3HT and ligands on the surface of NCs can prevent the two components getting into close proximity, which is harmful for the preparation of well-organized hybrid composite. Additional attractive force is required to overcome this barrier to induce the organization of n-type NCs on P3HT nanofiber. This may be achieved by the attachment of functional groups to P3HT molecules, which are selected based on ligand moieties. After solution-based crystallization, these functionalized P3HT nanofiber can act as the macromolecular ligand to facilitate the dispersion of NCs in the solution. To promote the polymer-NC interaction rather than NC-NC interaction in favor of the organization of hybrid composite, small NCs in sphere shape (i.e. QDs) can be a better choice.

In this chapter, material system based on P3HT and CdSe NCs were selected to investigate nanomorphology control and interface control in HSCs via the application of ordered *p*-type nanostructure. The effect of the incorporation of solution assembled P3HT nanofiber into CdSe NCs based solar cells is discussed first. A pyridine end-terminated low molecular weight P3HT (P3HT<sub>L</sub>-py) has been synthesized as the compatibilizer to

improve the organic-inorganic interface. Its interaction with CdSe NCs was characterized by solution stability and XPS studies. The results of its application in hybrid nanostructure and HSCs are presented as well.

## **3.2 Results and Discussion**

### **3.2.1 P3HT nanofiber and its application in HSCs**

#### **CdSe NCs and ligand exchange**

CdSe nanocrystals (NCs) were synthesized in the organic medium via hot coordinating solvent approach. After the synthesis, the morphology of CdSe NCs was studied using TEM. From the TEM image as shown in Figure 3-1a, it can be observed that as-synthesized CdSe NCs have uniform spherical shape with a mean diameter of *ca.* 4.5 nm, and their size distribution is very small. The distinct lattice fringes observed in these NCs indicate that they are highly crystalline, which is a crucial characteristic for good device performance. To make efficient HSCs, the long bulky ligand on the surface of NCs, which has adverse effect on the coupling between conjugated polymer and colloidal NCs and between NCs itself, must be replaced by small molecules. In this study, butylamine (BA) was used to replace the original ligands stearic acid (SA) and trioctylphosphine oxide (TOPO) on CdSe NCs. Thermogravimetric analysis (TGA) was used to probe the amount of organic molecules on the surface of NCs before and after ligand exchange. Serving as a reference, the boiling points of BA, SA, and TOPO are 78 °C, 350 °C, and 212 °C respectively. As shown in Figure 3-1b, two-step weight loss was observed both in CdSe-SA NCs sample and CdSe-BA NCs sample. For CdSe-SA NC sample, the small weight drop at *ca.* 200 °C can be attributed to the weight loss of phosphonic species (e.g.

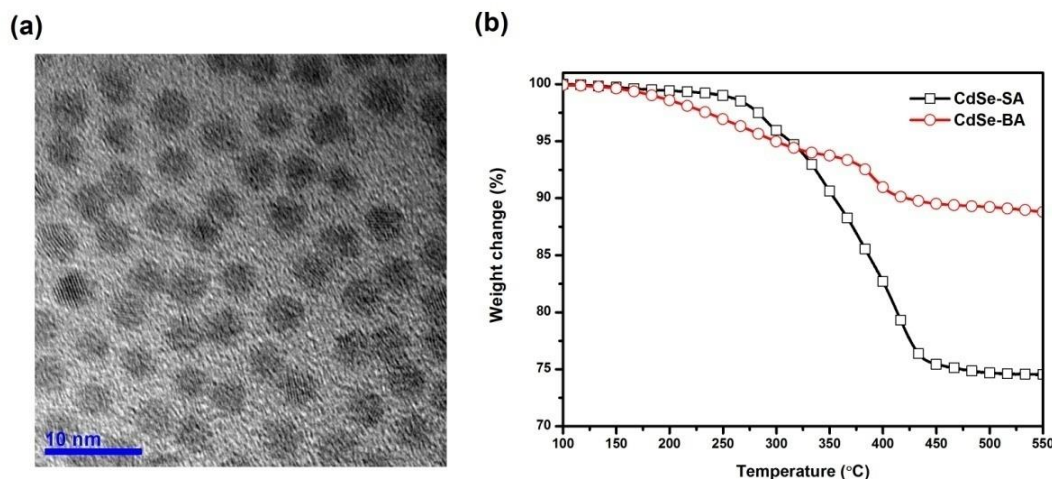


**Figure 3-1:** (a) TEM image of CdSe NCs right after synthesis and (b) TGA plots of CdSe NCs before ligand exchange (CdSe-SA) and after ligand exchange (CdSe-BA).

trioctylphosphine), which are loosely attached on the surface of CdSe NCs.<sup>29</sup> The prominent drop at around 350 °C can be assigned to the decomposition of stearic acid molecules; while a small fraction of organic substances could be TOPO. It is because that SA has stronger binding strength on the Cd surfaces compared to TOPO, which needs higher temperature to break the bonds.<sup>30,31</sup> For CdSe-BA, the weight loss between 200 °C and 350 °C is due to the desorption of butylamine, and the weight loss from 350 °C to 420 °C is due to the decomposition of residual ligand (stearic acid). In summary, before ligand exchange, organic species on CdSe NCs (i.e. CdSe-SA) makes up 25% of the total weight. While after ligand change, they are reduced to *ca.* 10%. It should be mentioned that although alkylamine has been applied as capping ligands for CdSe NCs in the application of solar cells, pyridine treatment was always employed as an intermediate step before ligand exchange with alkylamine.<sup>17,18</sup> Radychev *et al.* claimed that such additional step can help to remove the high molecular weight species on CdSe NCs. However, comparing our TGA curve with theirs, there is no much difference in the



degree of replacement. We believe that direct surface modification of colloidal NCs with butylamine can be a suitable method with respect to photovoltaic application.

### **Characterization of P3HT nanofiber**

P3HT nanofiber can be obtained via gradual cooling of the well-dissolved P3HT solution from temperature of *ca.* 80°C to room temperature, which is driven by the  $\pi$ - $\pi$  interchain interaction between P3HT main chains and solubility change during the cooling process. During this process, the interaction between P3HT molecules and solvent changes from solvophilic to solvophobic. There is always a color change and an increase in solution viscosity associated with the transition of P3HT. In general, absorption spectroscopy is applied to monitor the growth of P3HT nanofiber. Figure 3-2a shows the absorption spectra of P3HT in *p*-xylene as a function of ageing time starting right after the heating-cooling cycle. At the beginning, P3HT solution only shows a single absorption peak ( $P_1$ ) at *ca.* 460 nm, indicating well-dissolved polymer chains in solvent *p*-xylene. After 20 min, the solution starts to show a weak absorption peak ( $S_2$ ) at 610 nm. This peak is a direct evidence of the presence of ordered P3HT chains, its relative intensity with respect to the main absorption peak at 460 nm can be correlated to the extent of nanofiber formation.<sup>32</sup> The second vibronic peak ( $S_1$ ) at 560 nm becomes significant after 1 h. Both peaks increase with the aging time and saturate at 24 h. It is interesting to notice that the isobestic point at 475 nm can be clearly observed in the image, which is an indication of the transformation of polymeric chains from well-dissolved states to the aggregated form. The change in the color of P3HT solutions at 0 h and 24 h can be observed in the inset in

Figure 3-2a. It can be seen that the color of dilute P3HT solution is orange while dilute P3HT nanofiber solution shows a light purple color.

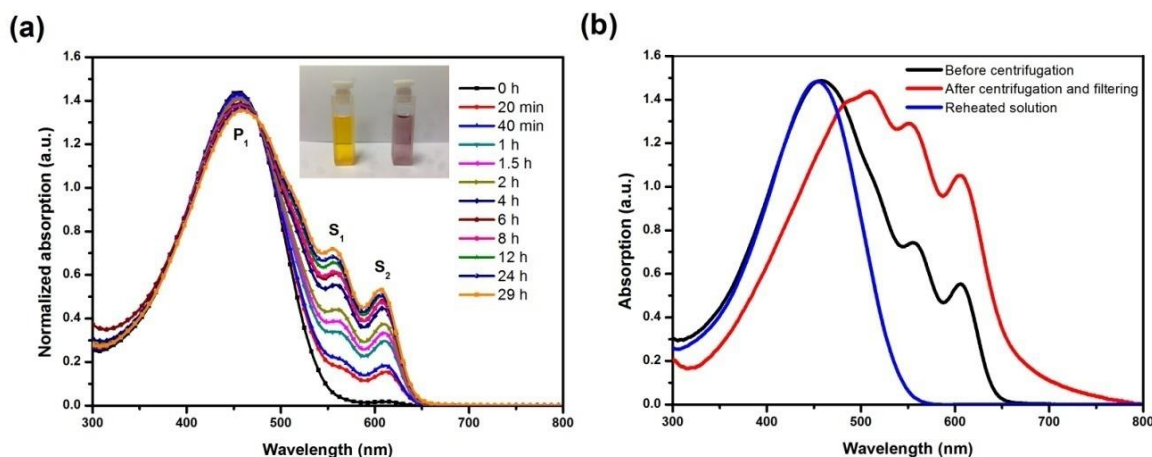


**Figure 3-2:** (a) Evolution of absorption spectra of P3HT in *p*-xylene as a function of time (b) Absorption spectra of P3HT nanofiber solution before centrifugation, suspension of redispersed pure nanofiber powder, and reheated pure nanofiber solution.

It should be noted that P3HT nanofiber solution used for the optical study includes a certain percentage of amorphous P3HT even for the solution aged for more than 24 h. Pure P3HT nanofiber in the form of dry powder can be obtained by successive centrifugation to remove the supernatant solution and wash the deposited substances with pure solvent up to five times, followed by filtration of the final solution. Pure P3HT nanofibers can be redispersed in *p*-xylene to form a stable suspension easily. Figure 3-2b shows the absorption spectra of P3HT nanofiber solution after growth before centrifugation, suspension solution of P3HT nanofiber powder after centrifugation and filtering and its reheated solution. It can be seen that the absorption profile of pure P3HT nanofiber has much more distinct vibronic peaks at 560 nm and 610 nm, with lower absorption intensity below 475-nm-wavelength point, compared to that of the impure

nanofiber solution. And P3HT nanofiber can be fully restored to amorphous P3HT easily by heating up the solution again, identified by the absorption spectra. As the process to obtain pure P3HT nanofiber is tedious and involves exposing the solution to air which may result in oxidation, saturated nanofiber solutions (i.e. 24 h) with fixed crystalline level grown under identical condition were used for photovoltaic fabrication.

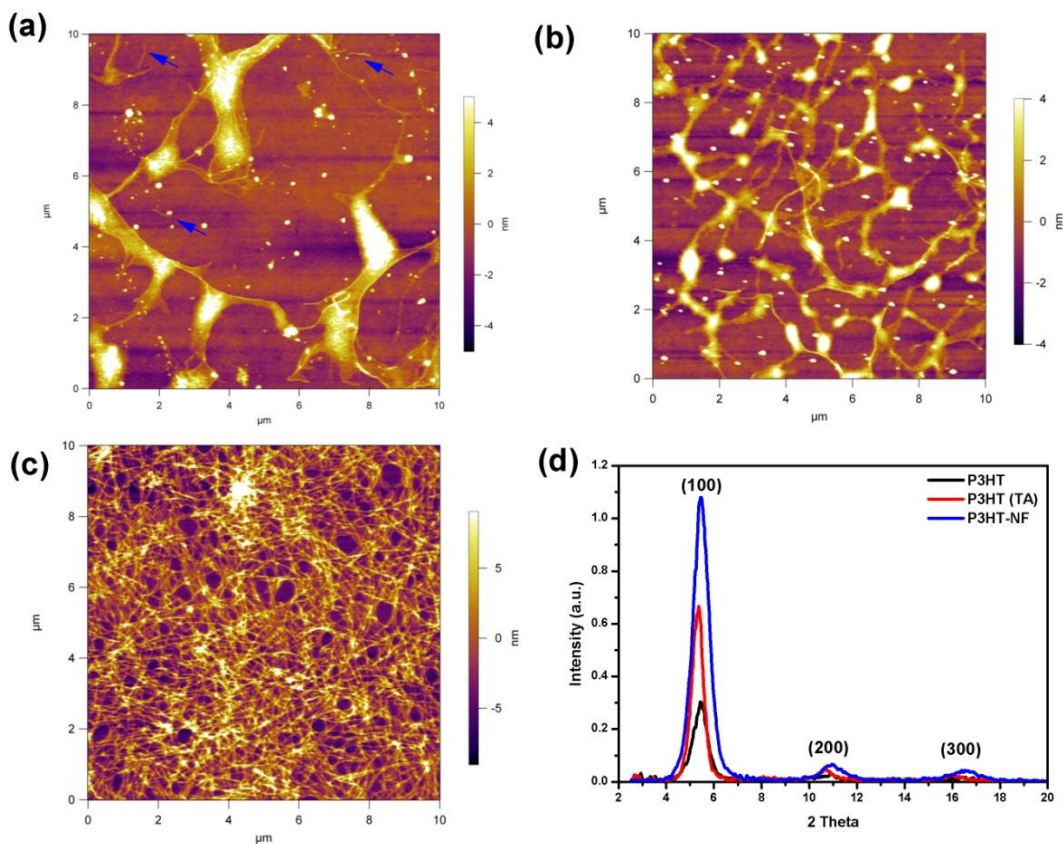


**Figure 3-3:** AFM topographical images of P3HT nanofibers aged for (a) 1 h, (b) 8 h, and (c) 24 h. XRD patterns of P3HT film, P3HT film (thermal annealed), and P3HT nanofiber film (d).

The morphology evolution of P3HT nanofiber can be characterized by AFM. Figure 3-3a to 3c show the topographic AFM images of spin-casted thin films of fiber suspensions aged for different time period, which were diluted to the same degree. At early growth

stage (1 h), although some long fibers (1-5  $\mu\text{m}$ ) can be observed on the substrates, most of P3HT stay in the form of amorphous clusters amongst these nanofibers. Many tiny fibers (less than 1  $\mu\text{m}$ ) can be seen across the whole film (indicated by the arrows in the figure). The widths of the fibers are between 10 nm and 20 nm. At 8 h, more fibers are observed, forming networks connected by domains of amorphous P3HT. By 24 h, the amount of nanofibers increases significantly, and nanofibers with length more than 5  $\mu\text{m}$  are present. But the widths of these fibers remain the same. These series of images suggest that self-assembly of P3HT chains mainly occurs along the length of fiber during nanofiber growth. The increase in the nanofiber length and nanofiber density can be correlated to the increase in the peak intensity at 610 nm (Figure 3-2a).

XRD were used to characterize the crystal structure of thin films consisting of P3HT nanofiber. For comparison, thin films spin-casted from P3HT solution without heat treatment and with thermal treatment were also examined. Figure 3-3d shows the XRD spectra of thin film of P3HT (not annealed, NA), thin film of P3HT (thermal annealed, TA), and thin films of P3HT nanofiber (NF). Diffraction peaks can be clearly observed at three  $2\theta$  positions -  $5.4^\circ$ ,  $11^\circ$ , and  $16^\circ$ , which are corresponded to (100), (200) and (300) reflections respectively. These diffraction peaks arise from the distances between the interdigitated alkyl chains on P3HT molecules.<sup>26</sup> Besides, the crystalline in thin films of P3HT (NA), P3HT (TA), P3HT-nanofiber (NF) are estimated to be 0.20, 0.37, and 0.84 respectively, by calculating the product of the peak intensity and full-width at half maximum in the diffractograms. Compared to thin films cast from P3HT solution, thin film of P3HT nanofiber shows much higher degree of order, even higher than P3HT thin film that undergone thermal treatment. The high crystallinity in P3HT nanofiber can

eventually lead to good charge transport in the thin film when they are incorporated into solar cells.

#### **Device based on CdSe NCs and P3HT nanofiber**

As P3HT nanofiber possesses good optical, structural and electronic properties; its incorporation into hybrid solar cells can be beneficial to the device performance. To obtain consistent results, only solutions of P3HT nanofiber aged for 24 h was selected for the device study. Figure 3-4a shows the current density-voltage ( $J$ - $V$ ) characteristic of solar cells based on P3HT:CdSe and P3HT nanofiber:CdSe under AM 1.5G illumination, which consisted of the same polymer-NCs weight ratio (1:9). It is found that non-fiber device showed a power conversion efficiency (PCE) of 1.07% with short-circuit current ( $J_{sc}$ ) of 4.05 mA/cm<sup>2</sup>, open-circuit voltage ( $V_{oc}$ ) of 0.71 V, and fill factor (FF) of 0.37. While device based on nanofiber system demonstrated a PCE of 1.33%, with  $J_{sc}$  of 4.88 mA/cm<sup>2</sup>,  $V_{oc}$  of 0.67 V, and FF of 0.40. The enhancement in PCE for P3HT nanofiber:CdSe devices results from the increase in  $J_{sc}$  and FF. Two reasons may contribute to the high  $J_{sc}$ . Firstly, when P3HT assemble into nanofiber, its bandgap become smaller because of the increase in the conjugation length. Thus, P3HT nanofiber can harvest more photons than unassembled P3HT, which contributes to higher  $J_{sc}$ . Secondly, charge transport can be improved in the photoactive layer due to the incorporation of more ordered P3HT nanofibers, which also account for better FF in the devices. The smaller  $V_{oc}$  in solar cell based on P3HT nanofiber and CdSe NCs can be attributed to the higher lying HOMO energy level after the assembly of P3HT, as  $V_{oc}$  of BHJ solar cells is determined by the difference between the HOMO level of donor and

the LUMO level of acceptor.<sup>33</sup> From the slopes of the  $J$ - $V$  curves of a solar cell near the open circuit voltage under light, its series resistance can be extracted. It is found that P3HT:CdSe device has a  $R_s$  of  $86 \Omega \text{ cm}^2$  while  $R_s$  of P3HT nanofiber:CdSe device is  $52 \Omega \text{ cm}^2$ . In general, higher series resistance of a solar cell can be a result of poor charge transport in the blend film due to poor morphology or mobility, and/or rougher interface between the hybrid film and electrodes. From the AFM images (Figure 3-5), it can be seen that the blend films of non-fiber system and fiber system have very similar roughness, indicating the interface contact resistance should be similar. Thus, lower series resistance in P3HT nanofiber:CdSe device may be attributed to better charge transport in the film due to the incorporation of P3HT nanofiber.

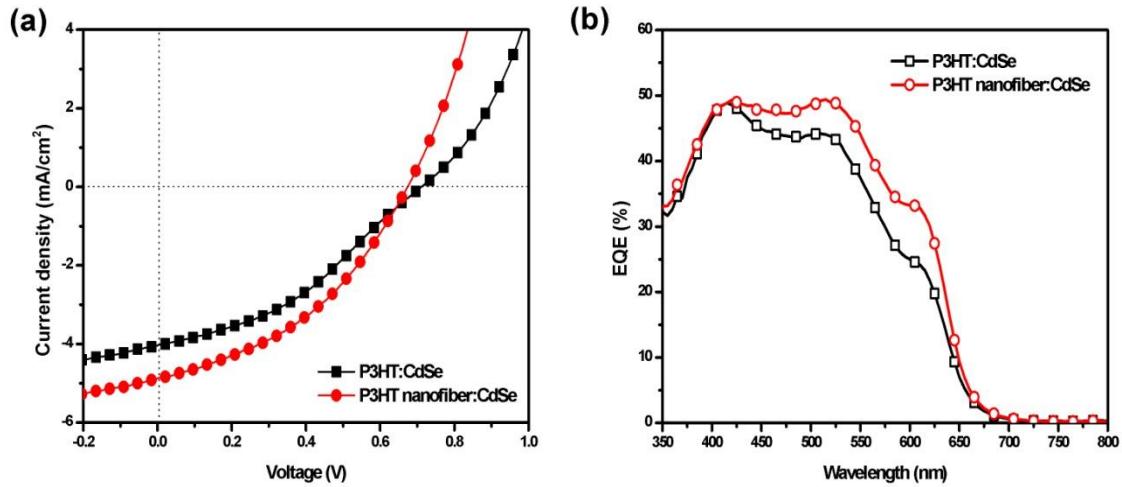


**Figure 3-4:** (a) Current density-voltage ( $J$ - $V$ ) characteristic of solar cells base on P3HT:CdSe and P3HT nanofiber:CdSe under one sun illumination, and (b) their corresponding EQE profiles.

External quantum efficiency (EQE) technique, which is a measurement of the number of charge carriers collected per incident photon by a solar cell, was also applied to characterize both devices. The obtained EQE profiles as a function of wavelength for

P3HT:CdSe device and P3HT nanofiber:CdSe device are shown in Figure 3-4b. It is found that device based on nanofiber system can give higher EQE response than that based on non-fiber system in the wavelength range between 450 nm and 650 nm. The increase in EQE agrees well with the increase in  $J_{sc}$ . The integrated  $J_{sc}$  of the EQE spectra is calculated to be 3.89 mA/cm<sup>2</sup> and 4.70 mA/cm<sup>2</sup> respectively for P3HT:CdSe device and P3HT nanofiber:CdSe device. Besides, device based on P3HT nanofiber:CdSe has a pronounced shoulder peak at wavelength of *ca.* 610 nm, which is corresponded to the absorption peak of P3HT nanofiber in absorption spectra shown above.

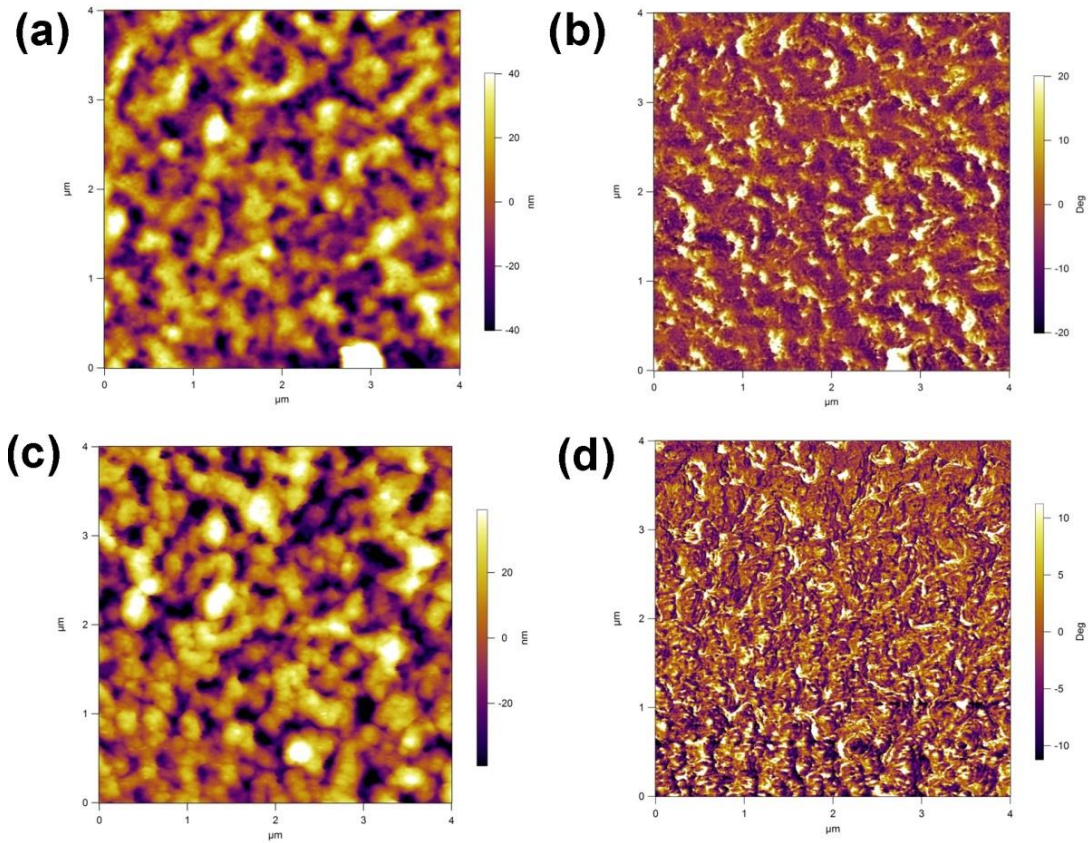


**Figure 3-5:** AFM height image (a) and phase image (b) of P3HT:CdSe solar cells; and AFM height image (c) and phase image (d) of P3HT nanofiber:CdSe solar cells.



Atomic force microscopy (AFM) was used to characterize the film morphology of both non-fiber device and fiber device, and their images are shown in Figure 3-5. Both images exhibit similar features, in which clusters of CdSe NCs (size of *ca.* 4.5 nm) are well distributed across the films. The absence of nanofiber (height of *ca.* 15 nm, width of 10-20 nm, length of a few micrometers) in thin film cast from P3HT nanofiber:CdSe blend is likely to be due to the fact that high loading of CdSe NCs preferentially segregate to the top of the films covering P3HT phase. The root-mean-square (RMS) roughness ( $R_{\text{RMS}}$ ) calculated from the topographical images of non-fiber blend film and fiber blend film are 19.8 nm and 21.1 nm respectively. The slightly rougher film in P3HT nanofiber:CdSe may result from the imperfect random stacking of *p*-type nanostructure, forming a slightly less compact film, considering the fact that both thin films have similar thickness. However, the phase image of P3HT nanofiber:CdSe blend film exhibits smaller aggregate domains, suggesting a better dispersion of colloidal NCs in the polymer phase. It may be due to the fact that the physical entanglement of P3HT nanofiber forms polymer networks, which can “trap” NCs in these networks because of the presence of weak interaction between exposed alkyl chains on P3HT nanofibers and ligands on the surface of CdSe NCs.

In summary, the incorporation of solution assembled P3HT nanofibers into hybrid solar cells is advantageous to the device performance due to the enhanced light absorption and better charge transport. Nevertheless, the improvement in the film morphology by the presence of P3HT nanostructure is not significant, which can be attributed to the lack of favorable interaction between P3HT molecules and colloidal CdSe NCs. Thus, material compatibility enhancement via molecular modification is needed to improve the hybrid



interface so that thin films consisting of well ordered organic-inorganic nanostructure can be achieved by simple solution deposition. Such high ordered morphology will be beneficial not only for charge transport, but also for charge generation.

### **3.2.2 End-chain functionalized low molecular weight P3HT (P3HT<sub>L</sub>)**

The previous section has demonstrated the merits of the incorporation of *p*-type organic nanostructure (i.e. P3HT nanofiber) in hybrid solar cells. It is well known that the device performance of a hybrid solar cell is not only affected by the structure of the donor phase, but also influenced by the donor-acceptor (D-A) interface and the phase structure of *n*-type acceptor. On top of maximizing the formation of crystalline polymer phase, it would be highly beneficial for device application if continuous electron transport pathways and large D-A interface can be achieved. Therefore, it is good to extend the organized nanostructure concept to the whole blend system. Nevertheless, the underlying different material nature tends to segregate polymer and NCs during film formation. A possible solution is to achieve assembled polymer nanofibers with functional groups accessible to NCs to let them preferentially interact with, and thus form a core-shell like hybrid nanostructure. It has been reported that end-group of low molecular weight (Mw) P3HT (P3HT<sub>L</sub>) can be chemically modified with different molecules by many groups.<sup>34-37</sup> On the other hand, large Mw P3HT can assemble into 1-D nanostructure much easier than P3HT<sub>L</sub> due to their higher degree of chain packing. Both properties are needed to construct a well-organized hybrid nanostructure. Thus, end-group functionalized P3HT<sub>L</sub> and high Mw P3HT can be added together during polymer self-assembly process so that

final polymer nanofibers contain anchoring sites to attract CdSe NCs to organize around them.

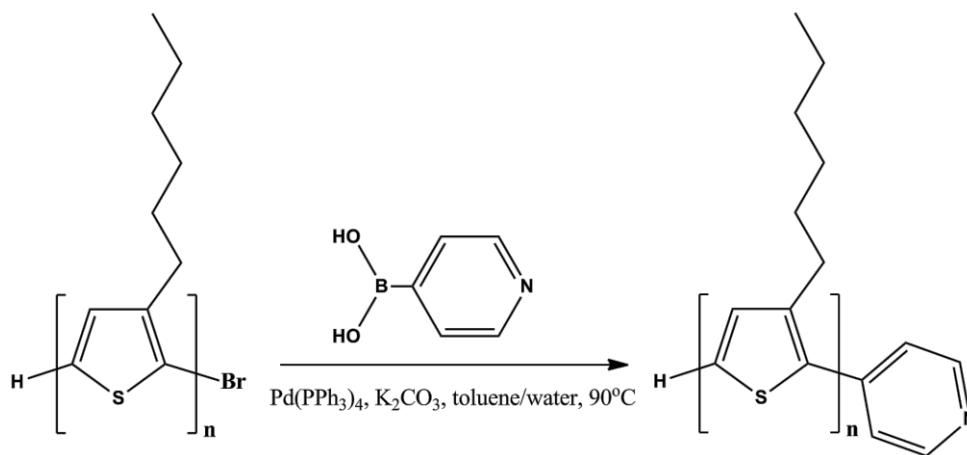


**Figure 3-6:** Synthesis route to prepare P3HT<sub>L</sub>-py

### Synthesis of pyridine-terminated P3HT (P3HT<sub>L</sub>-py)

Figure 3-6 shows the synthesis route to obtain pyridine-terminated P3HT (P3HT<sub>L</sub>-py). It was prepared using Suzuki coupling of 4-pyridinylboronic acid (PBA) with P3HT<sub>L</sub>, which is terminated with H and Br groups (MALDI-TOF results attached in Appendix). The raw material P3HT<sub>L</sub> was prepared by Grignard metathesis (GRIM) polymerization as described by McCullough and his co-workers.<sup>38</sup> Pyridine was selected as the functional moiety as it is one of the most suitable “conducting” ligands to replace original long ligands on the surface of inorganic NCs so far. It has been reported that colloidal NCs with surface modification by pyridine can give higher device performance compared to those without treatment. Compared to the work reported by Zhang *et al.*, who first synthesized functionalized ligand of 4-bromophenylmethyl dioctylphosphine oxide (TOPO-Br) and vinyl-terminated P3HT<sub>L</sub> (from H/Br terminated P3HT<sub>L</sub>) separately and

then coupled the two compounds to generate TOPO-terminated P3HT<sub>L</sub> via Heck coupling,<sup>39</sup> our approach is simpler. What's more, the attachment of pyridine moiety to P3HT<sub>L</sub> can be beneficial for charge transfer between polymer and NCs due to its having an aromatic structure.

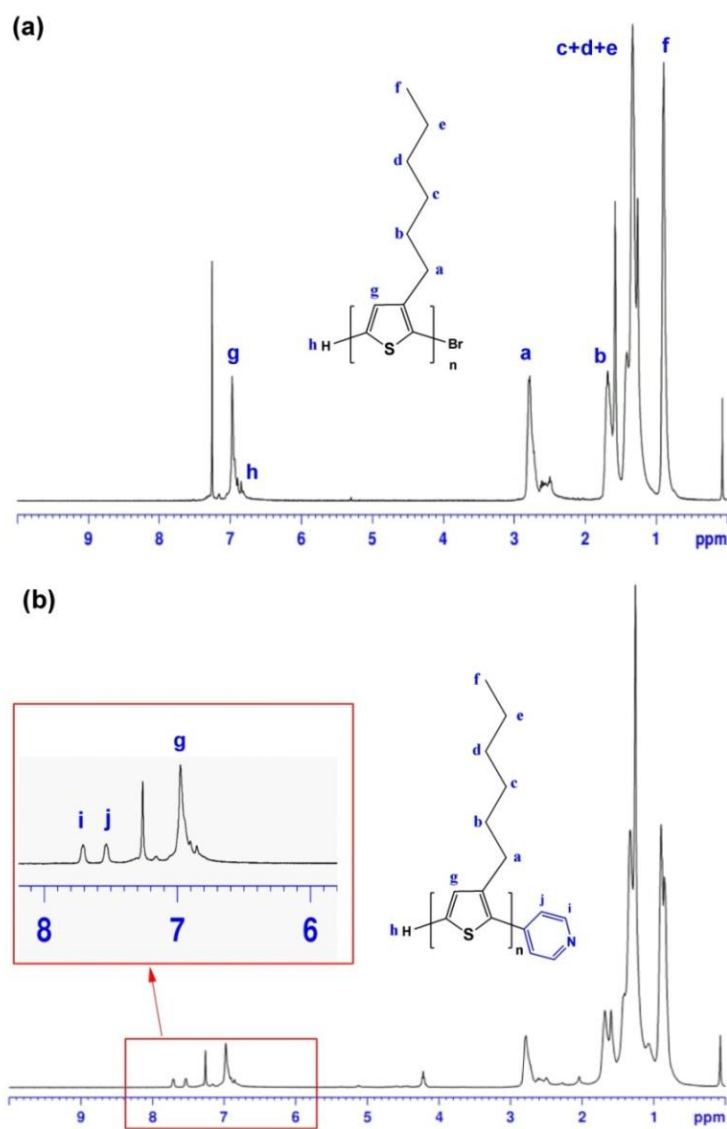


**Figure 3-7:** <sup>1</sup>H NMR spectra of (a) P3HT<sub>L</sub> and (b) P3HT<sub>L</sub>-py in CDCl<sub>3</sub>.

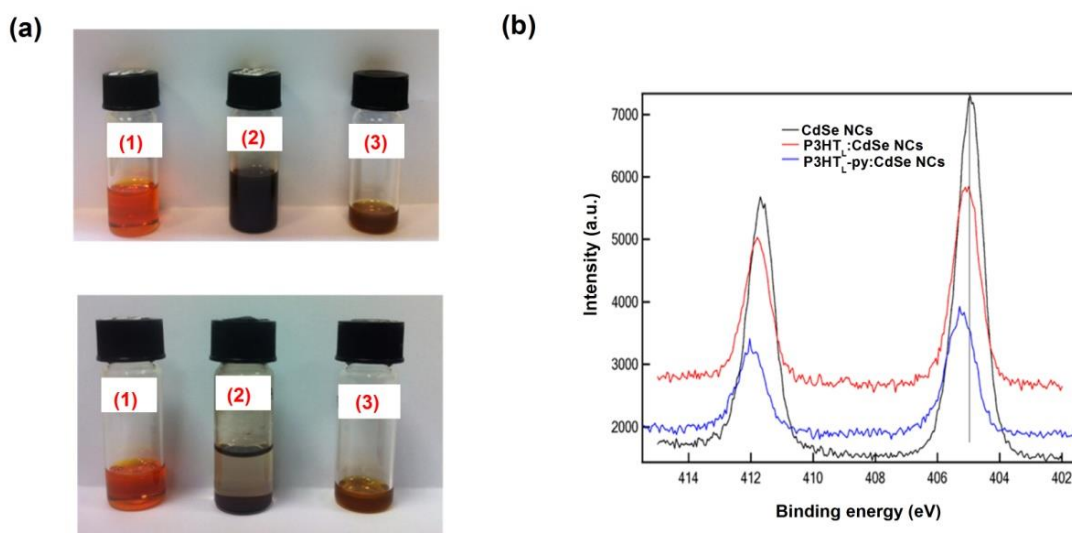
**Structure confirmation of P3HT<sub>L</sub>-py**

Figure 3-7 shows the <sup>1</sup>H NMR spectra of P3HT<sub>L</sub> and P3HT<sub>L</sub>-py dissolved in deuterated chloroform (CDCl<sub>3</sub>). Proton NMR spectroscopy is a common tool to probe the end group of P3HT polymer backbones, which can give sufficient sensitivity.<sup>40</sup> From the image, it can be observed that P3HT<sub>L</sub> has one sharp peak (marked as g) at chemical shift (δ) of 6.977 ppm, which originates from the proton in the aromatic ring of thiophene molecules. The proton peak at the end group of P3HT<sub>L</sub> main chains (marked as h) can be seen at the chemical shift of *ca.* 6.900 ppm. The peaks observed beyond chemical shift of 3 ppm can be attributed to the protons in the alkyl side chains of P3HT<sub>L</sub>. The large peak at chemical shift of ~ 7.24 ppm comes from the back group solvent CDCl<sub>3</sub>. By contrast, after functionalization, two distinct peaks appear at chemical shifts of 7.533 ppm and 7.708 ppm while the sharp peak of δ ~6.977 ppm remains. The two new peaks can be attributed to the two protons at different positions of the pyridine moiety bound to P3HT<sub>L</sub> molecules in P3HT<sub>L</sub>-py. Thus, pyridinylboronic acid (PBA) was successfully attached to the bromine end of H/Br-P3HT<sub>L</sub> via Suzuki coupling.

**Interaction between P3HT<sub>L</sub>-py and CdSe NCs**

**Solution stability** Solution stability test was carried out to confirm the favorable interaction between P3HT<sub>L</sub>-py and CdSe NCs. P3HT<sub>L</sub>-py was dissolved in chlorobenzene (CB) by stirring while CdSe NCs was dispersed in CB by sonication. Both solutions were prepared at the same concentration (1 mg/ml). The blend solution of P3HT<sub>L</sub>-py:CdSe NCs was prepared by mixing two single solutions at equal volume. Figure 3-8a shows solutions of P3HT<sub>L</sub>-py, CdSe NCs and P3HT<sub>L</sub>-py:CdSe NCs immediately after

sonication (top) and one day after sonication (bottom). It can be observed that all the solutions remained optically uniform right after sonication treatment. The P3HT<sub>L</sub>-py solution appeared to be orange, CdSe NCs solution was black, and P3HT<sub>L</sub>-py:CdSe blend was brownish in colour. However after sonication, CdSe NCs precipitated out of the solvent almost completely in a few hours, exhibiting only short-term stability. In contrast, no color change was observable in the P3HT<sub>L</sub>-py:CdSe blend solution and no precipitation was observed even after one day. This suggests that the addition of P3HT<sub>L</sub>-py could increase the solution stability of CdSe NCs. The binding of P3HT<sub>L</sub>-py onto the surface of CdSe NCs helped them to disperse better as P3HT molecules with long alkyl chain have much higher solubility in the solvent.



**Figure 3-8:** (a) Solutions of P3HT<sub>L</sub>-py (1), CdSe NCs (2) and P3HT<sub>L</sub>-py:CdSe (3) in chlorobenzene as sonicated (top) and after one day (bottom), and (b) XPS profiles of CdSe NCs, P3HT<sub>L</sub>:CdSe and P3HT<sub>L</sub>-py:CdSe.

**X-ray photoelectron spectroscopy (XPS)** The interaction between P3HT<sub>L</sub>-py and CdSe NCs was also verified using XPS study. Figure 3-8b shows the XPS spectra of Cd 3d

core level of thin films of CdSe NCs, P3HT<sub>L</sub>:CdSe, and P3HT<sub>L</sub>-py:CdSe. For CdSe NCs, the peak is at energy level of 405.0 eV. While for P3HT<sub>L</sub>:CdSe and P3HT<sub>L</sub>-py:CdSe, the XPS peaks are at 405.1 eV and 405.25 eV respectively. The binding energy shift of Cd 3d level means that the presence of P3HT<sub>L</sub> or P3HT<sub>L</sub>-py around CdSe NCs can induce some change on the surface electronic states of CdSe NCs. This shows that even for physically mixed P3HT<sub>L</sub> and CdSe NCs, the coordination interaction between CdSe NCs and sulfur atoms of the thiophene units in the polymer chains is present. Such finding has also been reported by Xu *et al.*<sup>41</sup> The higher binding energy shift (0.25 eV) of P3HT<sub>L</sub>-py:CdSe as compared to that of P3HT<sub>L</sub>:CdSe (0.1 eV) indicates the presence of pyridine end-functional group further enhance the interaction between the polymer and CdSe NCs. The measured XPS data agreed with the report value, where the XPS spectra of Cd3d core level of pyridine-capped CdSe is around 405.30 eV.<sup>42</sup> The binding energy between CdSe NCs and P3HT<sub>L</sub>-py is weaker than that of CdSe NCs and pyridine, which may be due to the long flexible polymer chains in P3HT<sub>L</sub>-py providing the steric hindrance for better interaction.

**Table 3-1:** Binding energy of Cd 3d core level in CdSe, P3HT<sub>L</sub>:CdSe, and P3HT<sub>L</sub>-py:CdSe

Sample	Binding energy
	(Cd 3d core level)
CdSe	405 eV
P3HT <sub>L</sub> :CdSe	405.1 eV
P3HT <sub>L</sub> -py:CdSe	405.25 eV

### Assembly of hybrid nanostructure

Once the favorable interaction between P3HT<sub>L</sub>-py and CdSe NCs has been determined, the self-assembled P3HT:CdSe NCs heterostructure was prepared using P3HT, P3HT<sub>L</sub>-

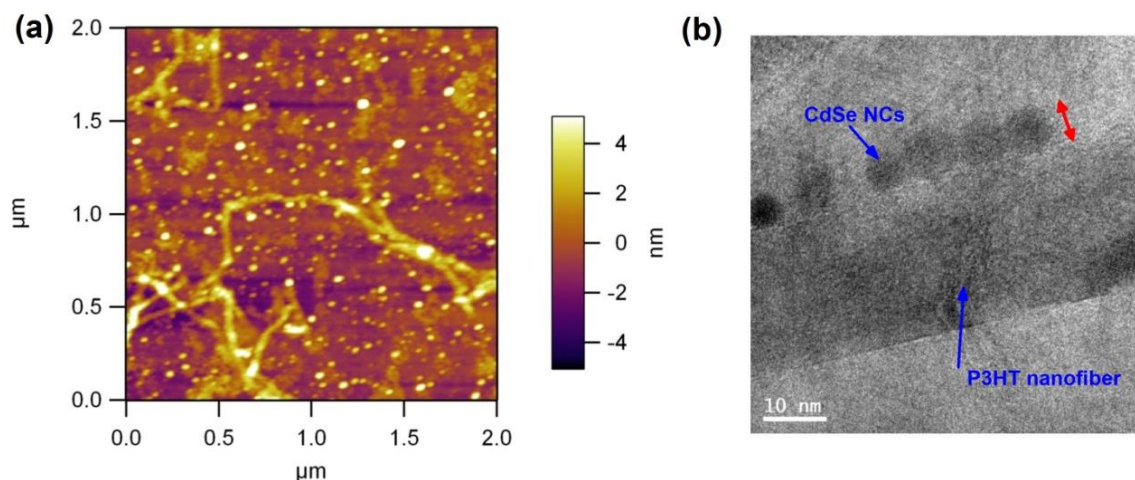


**Figure 3-9:** (a) AFM image and (b) TEM image of assembled P3HT nanofiber:CdSe hybrid nanostructure.

py and CdSe NCs. Functionalized P3HT nanofiber was grown by heating and cooling of P3HT solution in the presence of P3HT<sub>L</sub>-py. Due to the presence of intermolecular interaction between P3HT and P3HT<sub>L</sub>-py, P3HT<sub>L</sub>-py molecules can be inserted into P3HT nanofibers during the self-assembly process. Then, the enhanced fiber solution was blended with CdSe NCs solution to allow CdSe NCs to bind onto the surface of the polymer nanofibers because of the presence of pyridine groups on them. AFM and TEM were used to characterize the organized structures and the results are shown in Figure 3-9. From AFM images, it can be observed that some CdSe NCs are attached onto P3HT-nanofibers. TEM image also shows that some spherical CdSe NCs with diameter  $\sim 4.5$  nm were attached on P3HT-nanofibers with a width of  $\sim 20$  nm even after very high dilution. Both imaging characterization techniques showed that there were favorable interaction between P3HT-nanofiber and CdSe NCs. Nevertheless, the interaction between polymer nanofiber and CdSe NCs is not strong enough, as many CdSe NCs are still distributed on the substrates as shown by AFM image. The not-so-well-organized heterostructures may

either result from the incomplete functionalization of P3HT<sub>L</sub> or insufficient amount of P3HT<sub>L</sub>-py in the co-assembled nanofiber. But it should be noted that the hybrid system shown here are not fully optimized and more work is needed to improve polymer modification and take better control of the assembly process.

### **Device based on hybrid nanostructure**

P3HT-nanofiber assembled with the presence of P3HT<sub>L</sub>-py and that without the presence of P3HT<sub>L</sub>-py were blended with CdSe NCs to make solar cells. The obtained *J*-*V* characteristics of solar cells based on P3HT-nanofiber and solar cells based on co-assembled P3HT nanofiber are shown in Figure 3-10. P3HT-nanofiber:CdSe based solar cell (without P3HT<sub>L</sub>-py) shows a PCE of 1.23%, with *J*<sub>sc</sub> of 4.62 mA/cm<sup>2</sup>, *V*<sub>oc</sub> of 0.65, and FF of 0.40. In comparison, devices based hybrid nanostructure (with P3HT<sub>L</sub>-py) gives *J*<sub>sc</sub> of 5.12 mA/cm<sup>2</sup>, *V*<sub>oc</sub> of 0.64, FF of 0.49, and PCE of 1.59%. The enhancement in *J*<sub>sc</sub> and FF can be attributed to the increase in donor-acceptor interface due to the grafting of CdSe NCs around ordered P3HT nanofibers, and thus the formation of a better percolated nanomorphology. The larger interface is supported by the fact that the PL intensity of hybrid nanostructure film is significantly quenched, only about one-third of that of P3HT nanofiber:CdSe film, which is an indication of more efficient charge transfer (PL results attached in Appendix). Better charge transport is associated with the reduction in the series resistance of the hybrid films from 70 Ω cm<sup>2</sup> to 34 Ω cm<sup>2</sup> when P3HT<sub>L</sub>-py is present.

In summary, a solution assembled P3HT:CdSe hybrid nanostructure has been demonstrated via the attachment of CdSe NCs onto functionalized P3HT nanofiber,



which was prepared by co-assembly of P3HT and a new synthesized pyridine-terminated low molecular weight P3HT (P3HT<sub>L</sub>-py). It has been applied into solar cells to enhance the donor-acceptor interface and charge transport as well by taking the benefit of its material structure. However, PCE of the demonstrated HSCs is not very high, since the preparation of hybrid nanocomposite as well as device fabrication is not optimized yet. More work is needed to improve the material and device processing.

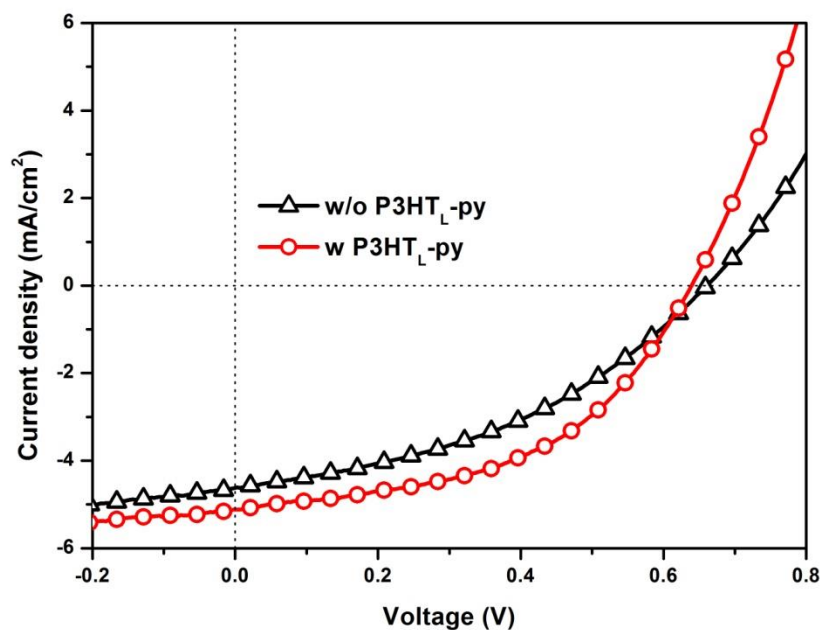


**Figure 3-10:** *J*-*V* characteristic of solar cells with the incorporation of assembled P3HT nanofiber without and with the presence of P3HT<sub>L</sub>-py under light illumination.

### 3.3 Conclusion

This chapter has demonstrated that the incorporation of P3HT nanofiber can contribute to higher  $J_{sc}$  and better device performance in HSCs due to enhanced light absorption and improved charge transport. In addition, a low molecule weight P3HT functionalized with amine moiety (P3HT<sub>L</sub>-py) has been successfully synthesized to encourage the interaction between the polymer and CdSe NCs, which was confirmed by solution stability study and XPS study. An ordered hybrid nanostructure has also been prepared in the solution by co-assembly of P3HT and P3HT<sub>L</sub>-py, followed by the attachment of CdSe NCs. The application of such hybrid nanostructure in HSCs was eventually beneficial for charge separation and charge transport due to the formation of more percolation paths. Although solar cells with higher performance are not achieved due to material and processing issues compared to P3HT:CdSe solar cells in similar condition (best PCE of 2.0%),<sup>18</sup> preparation of solution assembled hybrid nanocomposite can be a universal effective bottom-up approach to control nanomorphology in hybrid solar cells.

### 3.4 Experimental Section

**Materials** Cadmium selenide (CdSe) nanocrystals (NCs) were synthesized in organic medium via hot coordinating solvents method. In brief, 256 mg (2 mmol) of cadmium oxide (CdO, 99.95%, Fluka), 2.5 g of trioctylphosphine oxide (TOPO, 99%, Aldrich), 1.5 g of oleic acid (OA) were loaded into a three-necked flask equipped with a condenser and thermometer. The flask was loaded in a heating mantle and heated up to 330°C so that the color of the solution changed close to colorless (with slight yellowish), which is an indication of the formation of cadmium (II) complexes. The solution was then cooled to

310°C and the temperature was held constant for ten minutes. Afterwards fresh trioctylphosphine (TOP, 90%, Fluka) solution of selenium (Se, 99%, Kanto Chemical) was injected into the cadmium precursor solution. The CdSe nanocrystals were allowed to grow for 4 min and then the reaction was stopped by removing the reaction flask from the heating mantel. The ligand exchange method was modified based on literature. CdSe QDs in butylamine (40 mg/ml) were ultra-sonicated in ice-water for four hours and subsequently stirred overnight. Afterwards, nanocrystals were precipitated with excess acetone and dried under vacuum.

Pyridine-end functionalized P3HT<sub>L</sub> (P3HT<sub>L</sub>-py) was prepared via Suzuki coupling as following: Potassium carbonate (K<sub>2</sub>CO<sub>3</sub>) was dissolved in the solvent mixture of toluene (Sigma) and deionized (DI) water in a 50 ml flask. Then the solution was degassed for 20 min to remove dissolved oxygen molecules. In the glovebox, 30 mg of low molecular weight poly(3-hexylthiophene) (P3HT<sub>L</sub>, 1-Material Inc), 4-pyridinylboronic acid (PBA, Sigma), and tetrakis (triphenylphosphine) palladium (0) (Pd(PPh<sub>3</sub>)<sub>4</sub>, Sigma) were loaded into another flask. Afterwards, the flask of reagents were sealed and taken out of the glovebox, and injected with the K<sub>2</sub>CO<sub>3</sub> solution that had been previously degassed. The mixture was stirred on the hotplate at 90°C for two days under nitrogen protection in the dark. After the reaction, the mixture solution was poured into methanol to precipitate the polymer product. The functionalized P3HT (P3HT<sub>L</sub>-py) was finally purified by Soxhlet extraction with methanol (Sigma) and tetrahydrofuran (THF, Sigma).

P3HT (P3HT-rr) with Mw of 48300 g/mol (RMI-001 E/EE) was purchased from Rieke Metal Inc as donor material for device fabrication, which has a regioregularity approximately 96% or above.

P3HT nanofiber (9 mg/ml) was prepared by slow cooling of hot P3HT solution in *p*-xylene from 80 °C to 20 °C at a cooling rate of 10 °C/h by using a refrigerated circulator (Julabo F25-EC). After heating-cooling cycle, nanofiber solution was left in dark undisturbed for 24 h to ensure the saturation of nanofiber formation before device application. Co-assembled P3HT nanofiber was prepared similarly by heating-cooling of P3HT solution with the presence of P3HT<sub>L</sub>-py (1:1 by weight).

**Material characterization** The morphology of CdSe NCs was determined using transmission electron microscopy (TEM, JEOL 2010) with a LaB6 filament operating at an acceleration voltage of 200 kV. The amount of organic ligands in CdSe NCs samples was determined by thermal gravimetric analyzer (TGA Q500, TA Instruments). The weight loss was recorded by heating the samples from room temperature to 550 °C at a rate of 10 °C/min under nitrogen gas flow (60 mL/min). Atomic force microscopy (AFM, Asylum MFP-3D-BIO) in tapping-mode was used to probe the morphology of thin film samples, which was equipped with an Al reflex coated AFM probe (Olympus AC240TS) with a spring constant of 2 N m<sup>-1</sup> and tip radius of 9 nm. The X-ray photoelectron spectroscopy (XPS) spectra of thin film samples on silicon substrates were recorded by a homemade UHV system with a base pressure at 3 x 10<sup>-10</sup> Torr, which uses monochromatic Al K $\alpha$  x-ray as the excitation source and has a hemispheric electron analyzer (Omicron, EA125) to detect the photoelectrons.

**Device fabrication and characterization** For P3HT:CdSe devices, CdSe NCs (37.1 mg/ml) were first dispersed in a solvent mixture of chlorobenzene (CB, Sigma) and butylamine (BA, Fluka) by a volume ratio of 19:1; while P3HT (16.5 mg/ml) was dissolved in CB. Then, they were blended together to form the final photoactive solution

(33 mg/ml). For P3HT nanofiber:CdSe devices, CdSe NCs were dispersed in *p*-xylene and BA (5% v/v) while P3HT nanofiber was grown in *p*-xylene. Then, CdSe solution and P3HT-nanofiber solution were mixed together to form the blend solution (27 mg/ml) with 90 wt% CdSe. In a typical device fabrication process, indium tin oxide (ITO)-coated substrates (Kintec co, 7  $\Omega$ /sq) were first sequentially cleaned in detergent, de-ionized (DI) water, acetone and isopropyl alcohol (IPA) for 15 min each by ultrasonication. The ITO substrates were then blow-dried and cleaned by air plasma for 2 min. Afterwards, a layer of poly(3,4-ethylenedioxythiophene)-poly(styrenesulfonate) (PEDOT:PSS, CLEVIOS™ Al 4083, H.C. Stark) was spincoated on the ITO substrates at 3000 rpm for 60 s (thickness of  $\sim$  30 nm) and baked at 140 °C for 10 min. Next, the hybrid blend solution was spin-coated on PEDOT:PSS to form the photoactive layer in a N<sub>2</sub> filled glovebox. The substrates were then subject to heat treatment at 140 °C for 20 min. In the end, aluminium cathode was thermal deposited on the active layer through a shadow mask to form a device area of 0.07 cm<sup>2</sup> in the vacuum of  $2 \times 10^{-6}$  mbar.

The current density-voltage (*J*-*V*) characteristics of the devices were measured by a Keithley SMU 2400 source meter. Solar simulator (SAN-EI Electric) was used to generate the AM 1.5G illumination (100 mW cm<sup>-2</sup>). Before device testing, a digital Solar Meter (Daystar, DS-05A) was used to calibrate the light intensity. Merlin radiometer (Newport) with a monochromator-calibrated wavelength control was used to perform the external quantum efficiency (EQE) measurement and a calibrated silicon photodiode (Hamamatsu) was used to count the incident photons. All the device performance was measured in a N<sub>2</sub> filled glovebox.

### 3.5 References:

- (1) Nam, M.; Park, J.; Kim, S.-W.; Lee, K. *Journal of Materials Chemistry A* **2014**, *2*, 3978.
- (2) Talapin, D. V.; Lee, J.-S.; Kovalenko, M. V.; Shevchenko, E. V. *Chemical Reviews* **2009**, *110*, 389.
- (3) Guyot-Sionnest, P.; Hines, M. A. *Applied Physics Letters* **1998**, *72*, 686.
- (4) Saunders, B. R.; Turner, M. L. *Advances in Colloid and Interface Science* **2008**, *138*, 1.
- (5) Babel, A.; Jenekhe, S. A. *Advanced Materials* **2002**, *14*, 371.
- (6) Boucle, J.; Ravirajan, P.; Nelson, J. *Journal of Materials Chemistry* **2007**, *17*, 3141.
- (7) Xu, T.; Qiao, Q. *Energy & Environmental Science* **2011**, *4*, 2700.
- (8) Jangwon, S.; Sung Jin, K.; Won Jin, K.; Rohit, S.; Marek, S.; Alexander, N. C.; Paras, N. P. *Nanotechnology* **2009**, *20*, 095202.
- (9) Cui, D.; Xu, J.; Zhu, T.; Paradee, G.; Ashok, S.; Gerhold, M. *Applied Physics Letters* **2006**, *88*, 183111.
- (10) Wu, M.-C.; Chang, C.-H.; Lo, H.-H.; Lin, Y.-S.; Lin, Y.-Y.; Yen, W.-C.; Su, W.-F.; Chen, Y.-F.; Chen, C.-W. *Journal of Materials Chemistry* **2008**, *18*, 4097.
- (11) Shen, Q.; Ogomi, Y.; Das, S. K.; Pandey, S. S.; Yoshino, K.; Katayama, K.; Momose, H.; Toyoda, T.; Hayase, S. *Physical Chemistry Chemical Physics* **2013**, *15*, 14370.
- (12) Jeltsch, K. F.; Schädel, M.; Bonekamp, J.-B.; Niyamakom, P.; Rauscher, F.; Lademann, H. W. A.; Dumsch, I.; Allard, S.; Scherf, U.; Meerholz, K. *Advanced Functional Materials* **2012**, *22*, 397.
- (13) Lokteva, I.; Radychev, N.; Witt, F.; Borchert, H.; Parisi, J. r.; Kolny-Olesiak, J. *The Journal of Physical Chemistry C* **2010**, *114*, 12784.
- (14) Huynh, W. U.; Dittmer, J. J.; Alivisatos, A. P. *Science* **2002**, *295*, 2425.
- (15) Jun Yan, L.; Yeng Ming, L.; Jacek, N.; Mateusz, M. *Nanotechnology* **2012**, *23*, 315401.

- (16) Lek, J. Y.; Xing, G.; Sum, T. C.; Lam, Y. M. *ACS Applied Materials & Interfaces* **2013**, *6*, 894.
- (17) Olson, J. D.; Gray, G. P.; Carter, S. A. *Solar Energy Materials and Solar Cells* **2009**, *93*, 519.
- (18) Radychev, N.; Lokteva, I.; Witt, F.; Kolny-Olesiak, J.; Borchert, H.; Parisi, J. r. *The Journal of Physical Chemistry C* **2011**, *115*, 14111.
- (19) Halls, J. J. M.; Pichler, K.; Friend, R. H.; Moratti, S. C.; Holmes, A. B. *Applied Physics Letters* **1996**, *68*, 3120.
- (20) Shaw, P. E.; Ruseckas, A.; Samuel, I. D. W. *Advanced Materials* **2008**, *20*, 3516.
- (21) Mikhnenko, O. V.; Azimi, H.; Scharber, M.; Morana, M.; Blom, P. W. M.; Loi, M. A. *Energy & Environmental Science* **2012**, *5*, 6960.
- (22) Greenham, N. C.; Peng, X.; Alivisatos, A. P. *Physical Review B* **1996**, *54*, 17628.
- (23) Sun, B.; Snaith, H. J.; Dhoot, A. S.; Westenhoff, S.; Greenham, N. C. *J. Appl. Phys.* **2005**, *97*, 014914.
- (24) Sirringhaus, H.; Brown, P. J.; Friend, R. H.; Nielsen, M. M.; Bechgaard, K.; Langeveld-Voss, B. M. W.; Spiering, A. J. H.; Janssen, R. A. J.; Meijer, E. W.; Herwig, P.; de Leeuw, D. M. *Nature* **1999**, *401*, 685.
- (25) Jo, J.; Kim, S.-S.; Na, S.-I.; Yu, B.-K.; Kim, D.-Y. *Advanced Functional Materials* **2009**, *19*, 866.
- (26) Berson, S.; De Bettignies, R.; Bailly, S.; Guillerez, S. *Advanced Functional Materials* **2007**, *17*, 1377.
- (27) Li, L.; Lu, G.; Yang, X. *Journal of Materials Chemistry* **2008**, *18*, 1984.
- (28) Zhao, Y.; Shao, S.; Xie, Z.; Geng, Y.; Wang, L. *The Journal of Physical Chemistry C* **2009**, *113*, 17235.
- (29) Foos, E. E.; Wilkinson, J.; Mäkinen, A. J.; Watkins, N. J.; Kafafi, Z. H.; Long, J. P. *Chemistry of Materials* **2006**, *18*, 2886.
- (30) Rempel, J. Y.; Trout, B. L.; Bawendi, M. G.; Jensen, K. F. *The Journal of Physical Chemistry B* **2006**, *110*, 18007.
- (31) Peng, Z. A.; Peng, X. *Journal of the American Chemical Society* **2002**, *124*, 3343.

- (32) Chang, J.-F.; Clark, J.; Zhao, N.; Sirringhaus, H.; Breiby, D. W.; Andreasen, J. W.; Nielsen, M. M.; Giles, M.; Heeney, M.; McCulloch, I. *Physical Review B* **2006**, *74*, 115318.
- (33) Scharber, M. C.; Mühlbacher, D.; Koppe, M.; Denk, P.; Waldauf, C.; Heeger, A. J.; Brabec, C. J. *Advanced Materials* **2006**, *18*, 789.
- (34) Liu, J.; McCullough, R. D. *Macromolecules* **2002**, *35*, 9882.
- (35) Lohwasser, R. H.; Thelakkat, M. *Macromolecules* **2012**, *45*, 3070.
- (36) Lee, J.-Y.; Lin, C.-J.; Lo, C.-T.; Tsai, J.-C.; Chen, W.-C. *Macromolecules* **2013**, *46*, 3005.
- (37) Gilroy, J. B.; Lunn, D. J.; Patra, S. K.; Whittell, G. R.; Winnik, M. A.; Manners, I. *Macromolecules* **2012**, *45*, 5806.
- (38) Chen, T. A.; Rieke, R. D. *Journal of the American Chemical Society* **1992**, *114*, 10087.
- (39) Zhang, Q.; Russell, T. P.; Emrick, T. *Chemistry of Materials* **2007**, *19*, 3712.
- (40) Chen, T.-A.; Wu, X.; Rieke, R. D. *Journal of the American Chemical Society* **1995**, *117*, 233.
- (41) Xu, J.; Hu, J.; Liu, X.; Qiu, X.; Wei, Z. *Macromolecular Rapid Communications* **2009**, *30*, 1419.
- (42) Luo, X.; Liu, P.; Truong, N. T. N.; Farva, U.; Park, C. *The Journal of Physical Chemistry C* **2011**, *115*, 20817.



# Chapter 4

---

**CH<sub>3</sub>NH<sub>3</sub>PbI<sub>3</sub> for photovoltaic application**

## 4.1 Introduction

As mentioned in the previous chapter, similar to organic solar cells (OSCs), hybrid solar cells (HSCs) have the potential to combine good performance with low cost due to solution processability of these materials. HSCs should be able to achieve higher efficiency than OSCs because they have the added advantages of inorganic materials such as tunable absorption and better charge mobility. Generally, organic/hybrid solar cells worked based on the donor-acceptor (D-A) concept where two materials of different ionization potential and electron affinity are coupled to form the photoactive layer.<sup>1-4</sup> Charge transfer process occurs between the two selected components during device operation and hence the component that gives away electrons is referred to as the electron donor; while the other one that accepts electrons is known as the electron acceptor.

Depending on the construction of their photoactive layer, there are two cell architectures that are commonly encountered – bilayer structure and bulk heterojunction (BHJ) structure. If the photoactive part of the cells is constructed by stacking the donor and acceptor layers on top of each other, this is considered as the bilayer cell configuration. The photoactive layer can also be one single layer consisting of a blend of both donor and acceptor molecules, and this is therefore the bulk heterojunction (BHJ) structure. Although solar cells based on bilayer structure are developed first, they are not very much adopted until recently as they showed very poor cell performance. The reason is because the conjugated molecules, which are the main light absorber materials in organic/hybrid solar cells, have a short exciton diffusion length (*ca.* 10 nm),<sup>5-7</sup> and therefore the polymer layer has to have a thickness comparable to its exciton diffusion length to allow efficient charge generation, but this thickness is insufficient for light

absorption in these devices. Since BHJ structure consists of intimately mixed donor and acceptor regions, this structure can increase the number of excitons reaching the D/A interface, resulting in more efficient exciton dissociation compared to bilayer structure. Thus a much thicker photoactive film (up to a few hundred nanometers) can be used to enhance the light absorption. As a result, charge generation and device performance of solar cells are significantly improved. Currently, the state-of-the-art organic/hybrid solar cells make use of the BHJ structure to achieve high efficiencies.

In case of BHJ cells, there is a possibility for the formation of isolated donor and/or acceptor domains (i.e. lack of continuous transport paths). If this happens, charge carriers generated in such binary blend system can recombine easily and hence not contribute to the output photocurrent. Therefore, a substantial amount of research in the past few decades in BHJ solar cells has been focused on the optimization of the blend morphology to achieve interpenetrating networks of the donor and acceptor materials. It turns out that for efficient BHJ organics solar cells, one can easily make use of the large spectrum of molecule-solvent interactions to manipulate the morphology of the cast films. For hybrid BHJ solar cells (HSCs), on top of considering the conjugated molecules-solvent interactions, inorganic nanocrystals with capped ligands-solvent interactions and polymer-nanocrystals interactions have to be considered. Therefore, the morphology control in HSCs is much more challenging. There is always a lack of good electrical connectivity in the HSC films deposited from solution associated with the inefficient morphology control and this results in bad charge transport and collection. Thus although theoretically HSCs have the advantage of a wider spectrum of materials/materials control, still to date, the performance of HSCs with BHJ structure is much lower than those of

OSCs using similar donor polymer. To remove this dependence of device performance on good morphological control, bilayer architecture for HSCs might be a viable option. Charge transport and charge collection can be very efficient in this configuration since the donor and acceptor domains are well-defined. By employing a strongly light-absorbing inorganic or hybrid material with innate long exciton diffusion length ( $L_D$ ) comparable to the film thickness ( $t_{\text{film}}$ ) for optimal absorption, coupled with a material with selective charge affinity, both the light absorption and charge generation can be efficient. Thus, highly efficient hybrid bilayer solar cells may be achieved.

It has been shown that  $L_D$  of organic semiconductors is significantly influenced by the crystallinity of the film,<sup>8-10</sup> Organic-inorganic hybrid semiconductors also show such dependence,<sup>11</sup> and it is expected that hybrid compound with strong tendency self-assemble into well-organized nanostructures may exhibit long-range  $L_D$  characteristic. In recent years, some organometallic perovskite ( $\text{ABX}_3$ ) semiconductors (especially the lead based perovskite) have been shown to possess very good intrinsic properties for photovoltaic application. Thus hybrid organic-inorganic lead halide material class will be the focus in this chapter. These synthesized hybrid perovskite compounds will not only have good structural order resulting from the inorganic components, but also maintain its solution processability, making them especially suitable for high performance, low cost solar cells. On top of this, one of the advantages of these materials is that their bandgap can be tuned easily by varying the chemical composition of the organic and inorganic components.<sup>12</sup> Recently, highly efficient solar cells based on hybrid organic-inorganic lead halide have been reported. The best performing devices always consist of a mesoporous metal oxide scaffold which is processed at high temperature ( $\geq 300^\circ\text{C}$ ).<sup>13-15</sup> It

is useful to know whether this type of material can be used to achieve efficient solar cells using a simple planar heterojunction device without complex processing procedure. The fundamental property of this material class is not fully understood yet due to the rapid evolution in this field. In this chapter, the study on the charge generation dynamics and also the performance of such hybrid films will be presented. The common hybrid organic-inorganic lead halide, methylammonium lead iodide ( $\text{CH}_3\text{NH}_3\text{PbI}_3$ ) is selected for the investigation.

## **4.2 Results and Discussion**

As the behavior of the organic-inorganic lead halide thin film is strongly dependent on the structural property, the chemical synthetic route and the crystal structure of hybrid compound  $\text{CH}_3\text{NH}_3\text{PbI}_3$  will be first presented. The optical properties and the morphology of  $\text{CH}_3\text{NH}_3\text{PbI}_3$  thin film will then be discussed. To evaluate the potential of  $\text{CH}_3\text{NH}_3\text{PbI}_3$  in the field of photovoltaic application, its photophysical properties are investigated using the transient absorption/photoluminescence techniques. In addition, material system of  $\text{CH}_3\text{NH}_3\text{PbI}_3$  and CdSe QDs is chosen to investigate the behavior of  $\text{CH}_3\text{NH}_3\text{PbI}_3$  in solution-processable solar cells using a simple heterojunction bilayer structure. The dependence of the device performance on the annealing time of  $\text{CH}_3\text{NH}_3\text{PbI}_3$  film will also be presented.

### **4.2.1 Characterization of $\text{CH}_3\text{NH}_3\text{PbI}_3$ thin film**

To obtain  $\text{CH}_3\text{NH}_3\text{PbI}_3$ , organic salt ammonium iodide ( $\text{CH}_3\text{NH}_3\text{I}$ ) need be synthesized firstly by reacting methylamine ( $\text{CH}_3\text{NH}_2$ ) with hydroiodic acid (HI). Subsequently,

precursor components CH<sub>3</sub>NH<sub>3</sub>I and lead iodide (PbI<sub>2</sub>) were mixed in equimolar ratio to create a precursor solution of CH<sub>3</sub>NH<sub>3</sub>PbI<sub>3</sub>. As high chemical affinity is present between these organic and inorganic salts, upon the casting and solvent removal from the precursor on the substrates, a strong thermodynamic driving force will lead to the formation of the final perovskite compound. Subsequently, a polycrystalline perovskite film is formed by the intercalation of methylammonium cation (CH<sub>3</sub>NH<sub>3</sub><sup>+</sup>) into the slightly pre-deposited metal halide induced by gravity via the hydrogen/ionic interaction, and this is accompanied by a vivid color change from bright yellow to red during the drying of the film. Hence, thin films of methylammonium lead iodide (CH<sub>3</sub>NH<sub>3</sub>PbI<sub>3</sub>) can be prepared easily using the simple solution-deposition technique and this forms the photoactive layer of the solar cell. All the structural and optical characterizations are carried out directly on thin films of CH<sub>3</sub>NH<sub>3</sub>PbI<sub>3</sub>.

**Crystal Structure** X-ray diffraction (XRD) was used to examine the crystal structure of the CH<sub>3</sub>NH<sub>3</sub>PbI<sub>3</sub> thin film and the resulting XRD peak profile is presented in Figure 4-1a. Strong and sharp XRD peaks at  $2\theta$  angles of 13.95°, 28.35°, 31.70°, 40.45° and 43.05° can be identified, and they corresponded to the (110), (220), (310), (224), (314) planes of CH<sub>3</sub>NH<sub>3</sub>PbI<sub>3</sub> respectively. This indicates the CH<sub>3</sub>NH<sub>3</sub>PbI<sub>3</sub> thin films prepared this way have tetragonal perovskite structure. The lattice parameters of CH<sub>3</sub>NH<sub>3</sub>PbI<sub>3</sub> crystals can be calculated by using the two equations: (1) The Bragg's law equation:  $2d_{(hkl)} \sin \theta = \lambda$ , where  $h, k, l$ , are the Miller indices of the planes  $(hkl)$ , and  $d_{(hkl)}$  is the interplanar spacing between the two closest parallel planes  $(hkl)$ ;  $\theta$  is the Bragg angle and  $\lambda$  is the wavelength of the incoming x-ray radiation. (2) The tetragonal geometry is governed by

equation:  $\frac{1}{d_{(hkl)}^2} = \frac{h^2+k^2}{a^2} + \frac{l^2}{c^2}$ , and  $a = b$ , where  $a, b, c$  are the lattice constants of the unit cube. The lattice constants  $a$  and  $c$  of CH<sub>3</sub>NH<sub>3</sub>PbI<sub>3</sub> are 8.982 Å and 12.562 Å respectively. These values are very similar to those reported in literatures.<sup>15,16</sup> The structure of CH<sub>3</sub>NH<sub>3</sub>PbI<sub>3</sub> is depicted in Figure 4-1b, and the inorganic lead cations essentially occupy the center of the octahedron formed by halide anions; while the organic component - CH<sub>3</sub>NH<sub>3</sub> are located in the cuboctahedral coordination. As semiconductors in perovskite structure exhibit many interesting properties both in theory and in the real application, such as superconductivity and colossal magnetoresistance,<sup>17</sup> these hybrid perovskite CH<sub>3</sub>NH<sub>3</sub>PbI<sub>3</sub> may also have some interesting properties.

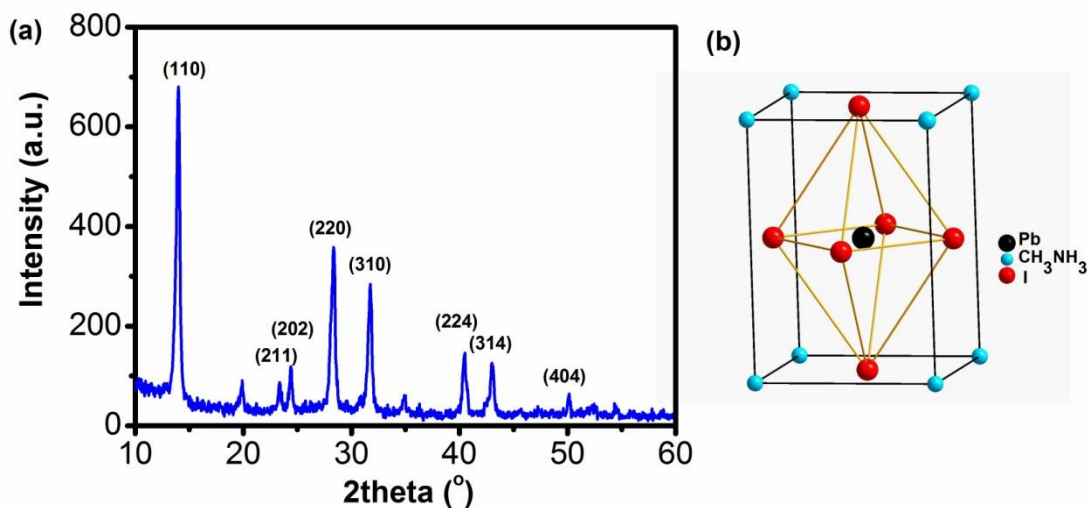


**Figure 4-1:** (a) XRD pattern from CH<sub>3</sub>NH<sub>3</sub>PbI<sub>3</sub> thin film and (b) its crystal structure.

**Film morphology** The surface morphology of CH<sub>3</sub>NH<sub>3</sub>PbI<sub>3</sub> thin film was probed by atomic force microscopy (AFM) operating in tapping mode and the obtained AFM images are shown in Figure 4-2. As shown, CH<sub>3</sub>NH<sub>3</sub>PbI<sub>3</sub> thin film is comprised of many small granular particles, and this often an evidence of three dimensional crystal growth in

these films. For the  $4\ \mu\text{m} \times 4\ \mu\text{m}$  scanning image, it can be observed that the film of  $\text{CH}_3\text{NH}_3\text{PbI}_3$  is quite homogenous and smooth, which has a surface RMS roughness ( $R_{\text{RMS}}$ ) of 14.9 nm. However, a number of small voids are present in the film that may result from the evaporation of dimethylformamide (DMF) solvent during film formation.<sup>18</sup> No significant differences in the morphology were observed when  $\text{CH}_3\text{NH}_3\text{PbI}_3$  are prepared on various substrates (e.g. ITO, PEDOT:PSS, and silicon). In the high resolution image ( $500\ \text{nm} \times 500\ \text{nm}$ ), the length and width of the small perovskite granular grains are estimated to be *ca.* 200 nm and *ca.* 80 nm.

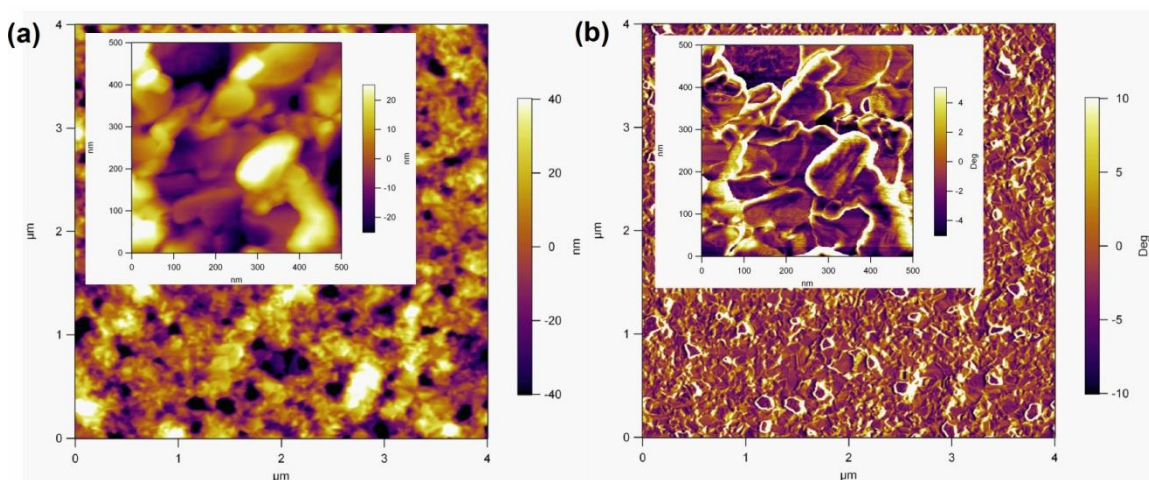


**Figure 4-2:** (a) AFM height image and (b) AFM phase image of  $\text{CH}_3\text{NH}_3\text{PbI}_3$  thin film with scan size of  $4\ \mu\text{m} \times 4\ \mu\text{m}$ . The high resolution images ( $500\ \text{nm} \times 500\ \text{nm}$ ) are shown in inset.

#### 4.2.2 Optical properties of $\text{CH}_3\text{NH}_3\text{PbI}_3$

The optical properties of  $\text{CH}_3\text{NH}_3\text{PbI}_3$  were studied using UV-Vis spectroscopy. The absorption profile obtained is shown in Figure 4-3a. The  $\text{CH}_3\text{NH}_3\text{PbI}_3$  thin film has a distinct absorption peak at *ca.* 360 nm and a broad shoulder peak at *ca.* 480 nm and 760 nm. The low energy absorption at 760 nm can be attributed to the direct bandgap



transition of this material. Besides, the film has a wide absorption extending the entire UV-Vis spectrum with an absorption onset at *ca.* 790 nm. To determine the effectiveness of the light absorption in a thin CH<sub>3</sub>NH<sub>3</sub>PbI<sub>3</sub> film, its absorption coefficient ( $\alpha$ ) is calculated using the methodology developed by Cesaria *et al.* specially for thin film system.<sup>19</sup> In this approach, when dealing with the absorption coefficient of the thin film, the non-measurable effect of the film-substrate interface is also taken account, which is particularly obvious for an ultrathin absorbing film (< 100 nm). In brief, the absorption coefficient of a thin film ( $\alpha_{film}$ ) can be obtained by subtracting the absorption coefficient of the bare substrate ( $\alpha_{sub}$ ) from that of the total substrate–film system ( $\alpha_{tot}$ ). The equation can be expressed as:

$$\alpha_{film} = \left( \frac{d_{sub}}{d_{film}} \right) (\alpha_{tot} - \alpha_{sub}) = \left( \frac{d_{sub}}{d_{film}} \right) \left[ \frac{1}{d_{tot}} \ln \left( \frac{1 - R_{tot}}{T_{tot}} \right) - \frac{1}{d_{sub}} \ln \left( \frac{1 - R_{sub}}{T_{sub}} \right) \right]$$

where  $d_{sub}$  is the substrate thickness,  $d_{film}$  is the film thickness of the absorbing material,  $d_{tot}$  is the total thickness of the substrate and the absorbing film;  $R_{sub}$  is the substrate reflectance and  $T_{sub}$  is the substrate transmittance;  $R_{tot}$  and  $T_{tot}$  are the total reflectance and the total transmittance of the film-substrate system.

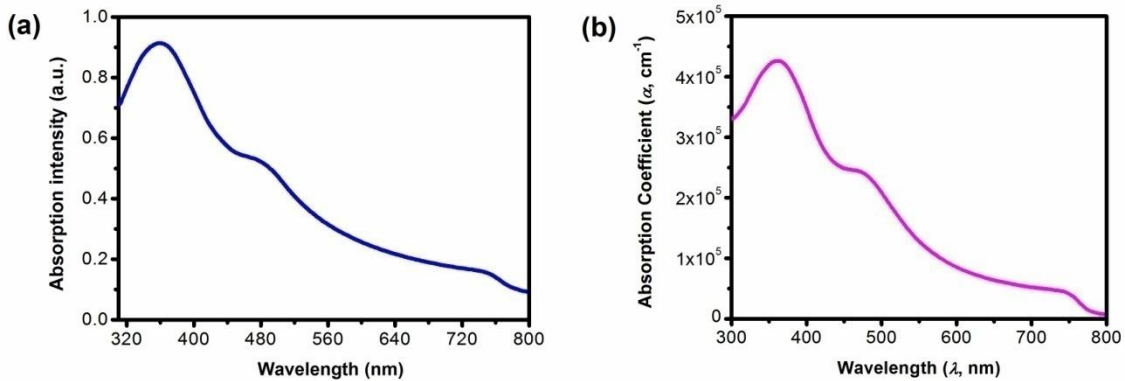


**Figure 4-3:** (a) UV-Vis absorption spectra and (b) absorption coefficient spectra of CH<sub>3</sub>NH<sub>3</sub>PbI<sub>3</sub> thin film prepared on quartz substrates.

The calculated  $\alpha$  curve for the CH<sub>3</sub>NH<sub>3</sub>PbI<sub>3</sub> thin film is plotted and shown in Figure 4-3b. It is found that the CH<sub>3</sub>NH<sub>3</sub>PbI<sub>3</sub> film can have a maximum  $\alpha$  value of  $4.3 \times 10^5 \text{ cm}^{-1}$  at 360 nm. Im *et al.* have reported the absorption coefficient of CH<sub>3</sub>NH<sub>3</sub>PbI<sub>3</sub> is  $1.5 \times 10^4 \text{ cm}^{-1}$  at 550 nm earlier;<sup>16</sup> while at the same wavelength, our calculated  $\alpha$  value is  $1.3 \times 10^5 \text{ cm}^{-1}$ . The difference is approximately in an order of magnitude. This discrepancy may be due to the fact that the optical contribution of TiO<sub>2</sub> was also included in their calculation as Im *et al.* performed their test on the CH<sub>3</sub>NH<sub>3</sub>PbI<sub>3</sub>-coated TiO<sub>2</sub> samples. Compared to those commonly used conjugated molecules in the highly efficient organic solar cells, the absorption coefficient of CH<sub>3</sub>NH<sub>3</sub>PbI<sub>3</sub> is comparable to or even higher than most of them.<sup>20-22</sup> The value is also in the same range to some of inorganic semiconductors, e.g. Cu<sub>2</sub>ZnSnS<sub>4</sub> ( $\alpha \approx 6.1 \times 10^4 \text{ cm}^{-1}$  at 650 nm)<sup>23</sup> or CuInSe<sub>2</sub> ( $\alpha \approx 6 \times 10^5 \text{ cm}^{-1}$  at 690 nm)<sup>24</sup>.

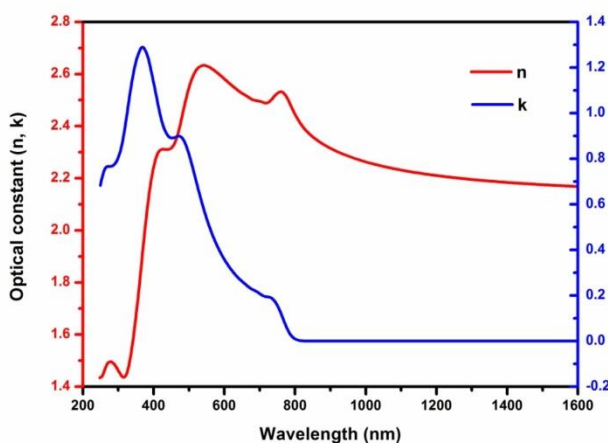


**Figure 4-4:** Refractive index  $n$  and extinction coefficient  $k$  determined for CH<sub>3</sub>NH<sub>3</sub>PbI<sub>3</sub>

The refractive indices and extinction coefficient ( $n$ ,  $k$ ) of CH<sub>3</sub>NH<sub>3</sub>PbI<sub>3</sub> in the wavelength range of 300 nm to 1600 nm were determined using an ellipsometer. The measured spectrum of CH<sub>3</sub>NH<sub>3</sub>PbI<sub>3</sub> as a function of wavelength was fitted using the B-spline

model. Figure 4-4 showed the optical constants variation as a function of wavelength. The mean square error (MSE) value for the B-spline fit is only 2.295 indicating that the fit is very good. The characteristic absorption peaks of  $\text{CH}_3\text{NH}_3\text{PbI}_3$  film at 360 nm and 480 nm can be easily observed in the extinction coefficient ( $k$ ) plot. In addition, the thickness of the thin  $\text{CH}_3\text{NH}_3\text{PbI}_3$  film is also determined using the Cauchy model and found to be 59.58 nm. In summary, the broad absorption window and large optical absorption coefficient (i.e. large absorption depth) ensure that the photons can be efficiently harvested by the thin  $\text{CH}_3\text{NH}_3\text{PbI}_3$  film, which is essential for an efficient solar cell.

#### **4.2.3 Photophysical properties of $\text{CH}_3\text{NH}_3\text{PbI}_3$**

One fundamental property of the photoactive materials that governed their effectiveness for use in excitonic cells is the exciton (bound electron-hole pair) diffusion length. This parameter will eventually determine the number of excitons reaching the donor-acceptor (D-A) interface and hence the output photocurrent. Therefore, transient optical spectroscopy with femtosecond resolution was employed to study this key property in  $\text{CH}_3\text{NH}_3\text{PbI}_3$ . This measurement was done by using the surface quenching technique, where by the loss in the luminescence in the thin film of the material to be tested was induced by an additional quenching layer. This loss in luminescence is monitored and compared to that in an identical film without the quenching layer. The quencher should be able to dissociate the excitons that made it to the interface readily and charge transfer can take place from the  $\text{CH}_3\text{NH}_3\text{PbI}_3$  layer to the quencher instead of fluorescence resonance energy transfer (FRET). In this study, organic semiconductor [6,6]-phenyl- $\text{C}_{61}$ -butyric acid methyl ester ( $\text{PC}_{61}\text{BM}$ ) with the lowest conduction band (CB) level lying

below that of  $\text{CH}_3\text{NH}_3\text{PbI}_3$  is used as the electron extraction layer for a heterojunction film; while in the other bilayer, small molecule 2,2',7,7'-tetrakis(*N,N'*-di-*p*-methoxyphenylamine)-9,9'-spirobifluorene (spiro-OMeTAD) with the highest valence band (VB) level above that in  $\text{CH}_3\text{NH}_3\text{PbI}_3$  is selected as the hole extraction material. As the luminescence loss of the quenched film (i.e.  $\text{CH}_3\text{NH}_3\text{PbI}$ ) depend both on the diffusion coefficient and the film thickness of the testing material, the thickness of  $\text{CH}_3\text{NH}_3\text{PbI}_3$  thin film needs to be measured first so as to determine the diffusion coefficient eventually. Figure 4-5 shows the depth profiles of the pure  $\text{CH}_3\text{NH}_3\text{PbI}_3$  film,  $\text{CH}_3\text{NH}_3\text{PbI}_3/\text{PC}_{61}\text{BM}$  bilayer film and  $\text{CH}_3\text{NH}_3\text{PbI}_3/\text{spiro-OMeTAD}$  bilayer film spin cast onto the quartz substrates measured using a profilometer. The thicknesses of the films are identical to those samples prepared for the following transient spectroscopy studies. The height lines shown are quite representative, which were all drawn arbitrarily across the center region of the samples. The tiny variation of height in the step line profiles indicates these films are very smooth, which is also supported by the AFM images. The abrupt spike signal in the step profile of pure  $\text{CH}_3\text{NH}_3\text{PbI}_3$  film is attributed to the soft material accumulation from the mechanical scratch-drawing at the testing spot. The final thicknesses of the thin films are measured to be about 65 nm, 109 nm and 155 nm respectively. The thickness of  $\text{CH}_3\text{NH}_3\text{PbI}_3$  thin films determined here is close to the one measured using the ellipsometry. The low ratio of the film roughness to the film thickness implies the heterojunction have smooth contacting interface since the bilayer samples were not subjected to any heat treatment after the quenching material was cast on the  $\text{CH}_3\text{NH}_3\text{PbI}_3$  layer.

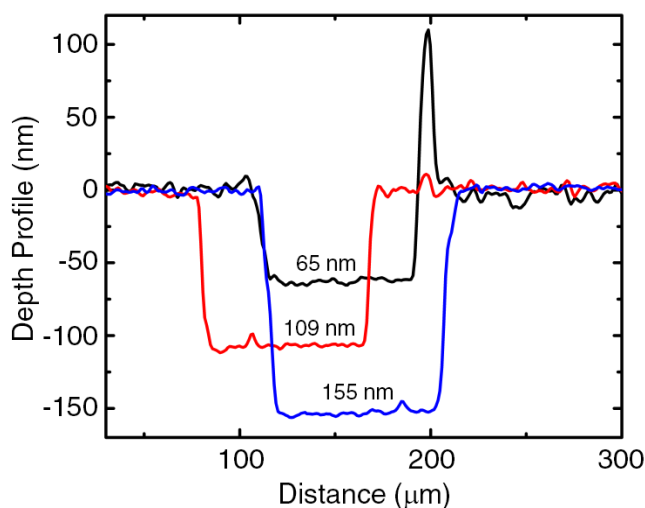


**Figure 4-5:** Step profiles of the thickness of the  $\text{CH}_3\text{NH}_3\text{PbI}_3$  (black) film,  $\text{CH}_3\text{NH}_3\text{PbI}_3/\text{PC}_{61}\text{BM}$  (red) and  $\text{CH}_3\text{NH}_3\text{PbI}_3/\text{spiro-OMeTAD}$  (blue) bilayer films.

**Photoluminescence (PL) spectroscopy** Figure 4-6a shows steady-state PL spectra of the pure  $\text{CH}_3\text{NH}_3\text{PbI}_3$  thin film,  $\text{CH}_3\text{NH}_3\text{PbI}_3/\text{PC}_{61}\text{BM}$  bilayer film and  $\text{CH}_3\text{NH}_3\text{PbI}_3/\text{spiro-OMeTAD}$  bilayer film. All the samples exhibit a characteristic PL peak at *ca.* 775 nm, which is close to the absorption band edge (*ca.* 760 nm) of  $\text{CH}_3\text{NH}_3\text{PbI}_3$  shown earlier. This small Stokes shift (*ca.* 15 nm) indicates that the vibronic relaxation in the perovskite crystals is quite weak. Compared to the pure  $\text{CH}_3\text{NH}_3\text{PbI}_3$  film, the PL intensities of both bilayer films are greatly reduced since the photogenerated excitons were able to diffuse to the interface where they are quenched. The PL intensity of  $\text{CH}_3\text{NH}_3\text{PbI}_3/\text{PCBM}$  bilayer is only about 2% of that of the pure  $\text{CH}_3\text{NH}_3\text{PbI}_3$  (i.e. signal reduced by a factor of 50); while the PL intensity is quenched by a factor of 12.5 when  $\text{CH}_3\text{NH}_3\text{PbI}_3$  forms a heterojunction with spiro-OMeTAD. The charge carrier transfer efficiencies ( $\eta_{\text{CT}}$ ) for  $\text{CH}_3\text{NH}_3\text{PbI}_3/\text{PC}_{61}\text{BM}$  and  $\text{CH}_3\text{NH}_3\text{PbI}_3/\text{spiro-OMeTAD}$  heterojunctions are 98% and

92% individually. Such high degree of quenching is comparable to those reported for the closely mixed donor-acceptor systems,<sup>25-27</sup> which is rather amazing considering that these samples are constructed in a bilayer configuration. The highly effective PL quenching suggests that the diffusion length of excitons (or electron-hole pairs) inside the CH<sub>3</sub>NH<sub>3</sub>PbI<sub>3</sub> layer is equivalent or larger than the film thickness. What's more, at 600 nm photoexcitation, CH<sub>3</sub>NH<sub>3</sub>PbI<sub>3</sub> has a linear absorption coefficient of  $8.55 \times 10^4 \text{ cm}^{-1}$  and a corresponding penetration depth of *ca.* 100 nm, which is larger than the film thickness of the CH<sub>3</sub>NH<sub>3</sub>PbI<sub>3</sub> layer in the testing samples. These two studies suggest that the charge carriers are almost homogenously generated in the CH<sub>3</sub>NH<sub>3</sub>PbI<sub>3</sub> film during the time-resolved spectroscopy studies.<sup>16</sup>

Figure 4-6b exhibits the time-resolved PL spectra of the samples, quartz/CH<sub>3</sub>NH<sub>3</sub>PbI<sub>3</sub>, quartz/CH<sub>3</sub>NH<sub>3</sub>PbI<sub>3</sub>/PC<sub>61</sub>BM and quartz/CH<sub>3</sub>NH<sub>3</sub>PbI<sub>3</sub>/spiro-OMeTAD measured at 760 nm by the time-resolved PL spectroscopy. As the equipment setup has a time resolution of 150 fs, it is sufficient to resolve the fast quenching that occurs in the initial decay stage. These transient plots all display a single exponential PL decay, suggesting these samples have good crystalline quality. Using an exponential function fitting for these plots, pure CH<sub>3</sub>NH<sub>3</sub>PbI<sub>3</sub> has a time constant ( $\tau_0$ ) of  $4.5 \pm 0.3 \text{ ns}$ . When CH<sub>3</sub>NH<sub>3</sub>PbI<sub>3</sub> is coupled with PC<sub>61</sub>BM or spiro-OMeTAD, the PL lifetimes of the heterojunctions ( $\tau_{PL}$ ) were shortened to be  $0.37 \pm 0.02 \text{ ns}$  and  $0.64 \pm 0.03 \text{ ns}$  respectively. As the charge-carrier transfer time ( $\tau_{CT}$ ) between the two materials can be determined by equation  $1/\tau_{PL} = 1/\tau_0 + 1/\tau_{CT}$ , heterojunctions of CH<sub>3</sub>NH<sub>3</sub>PbI<sub>3</sub>/PC<sub>61</sub>BM and CH<sub>3</sub>NH<sub>3</sub>PbI<sub>3</sub>/spiro-OMeTAD have a  $\tau_{CT}$  of 0.40 ns and 0.75 ns separately. The charge transfer efficiencies ( $\eta_{CT}$ ) of the heterojunction can be described as  $\eta_{CT} = (1/\tau_{CT})/(1/\tau_{PL})$  and the charge

transfer efficiencies in CH<sub>3</sub>NH<sub>3</sub>Pb<sub>3</sub>/PC<sub>61</sub>BM and CH<sub>3</sub>NH<sub>3</sub>PbI<sub>3</sub>/spiro-OMeTAD are calculated to be 92% and 86% accordingly. These values are slightly lower than those previously measured in the steady-state PL measurement. This discrepancy can arise from two possible aspects. Firstly, the light absorption in the steady-state PL study is slightly altered at the heterojunction due to reflection, scattering and refraction of light at the interface, which will affect the measurement at long time scale.<sup>28</sup> Secondly, the charge carrier transfer at the interface may be too fast to be monitored due to the current temporal resolution of the transient PL setup.

The PL decay dynamics in CH<sub>3</sub>NH<sub>3</sub>Pb<sub>3</sub> can be modeled by one dimensional diffusion equation.<sup>29</sup> The spatial distribution of excitons  $n(z, t)$  generated throughout the thin film as a function of time (t) can be described as (a):  $\frac{\partial n(z,t)}{\partial t} = D \frac{\partial^2 n(z,t)}{\partial z^2} - k(t)n(z, t)$ , where  $z$  represents the vertical distance of a point in the CH<sub>3</sub>NH<sub>3</sub>Pb<sub>3</sub> film from the quartz/active layer interface,  $D$  is the exciton diffusion coefficient, and  $k(t)$  is the PL decay rate of CH<sub>3</sub>NH<sub>3</sub>Pb<sub>3</sub> without any quencher layer. Right after the excitation by a 600-nm laser pulse, the initial exciton distribution throughout the film can be expressed as equation:  $n(z, 0) = n(0)e^{-\alpha z}$ , where  $\alpha$  is the linear absorption coefficient of CH<sub>3</sub>NH<sub>3</sub>Pb<sub>3</sub> at the excitation wavelength. When the quencher is absent, the decay rate of excited species in CH<sub>3</sub>NH<sub>3</sub>Pb<sub>3</sub> is independent of their initial distribution and is uniform across the film. When a quencher is coupled, the PL decay rate in CH<sub>3</sub>NH<sub>3</sub>Pb<sub>3</sub> will be influenced both by the spatial distribution and the film thickness. As charge transfer between CH<sub>3</sub>NH<sub>3</sub>Pb<sub>3</sub> and PC<sub>61</sub>BM (or spiro-OMeTAD) is ultrafast, the quenching rate at the donor/acceptor interface can be assumed to be infinite (i.e. no excitons exist at the interface), creating a boundary condition. The equation (a) was then numerically solved with the initial charge

carrier distribution and the boundary condition. The total charge number  $N(t)$  within the film is yielded, which can be expressed as:

$$N(t) = \frac{2n_0L}{\pi} \exp(-kt) \sum_{m=0}^{\infty} \left\{ \exp\left[-\frac{\pi^2 D}{L^2} \left(m + \frac{1}{2}\right)^2 t\right] \frac{\exp(-\alpha L)\pi\left(m + \frac{1}{2}\right) + (-1)^m \alpha L}{\left[(\alpha L)^2 + \pi^2 \left(m + \frac{1}{2}\right)^2\right]^{(m + \frac{1}{2})}} \right\},$$

where  $L$  is the thickness of the film. Then the calculated PL intensities as a function of time was plotted to match the experimental decay data to extract the only unknown parameter  $D$ . Thus, the diffusion coefficients of electron and hole in CH<sub>3</sub>NH<sub>3</sub>PbI<sub>3</sub> were estimated to be 0.037 cm<sup>2</sup>/s and 0.018 cm<sup>2</sup>/s respectively. It should be noted that the obtained diffusion coefficients are quite conservative, as a larger value is required to achieve the same amount of quenching for a finite quenching rate. As the diffusion length  $L_D$  is governed by  $L_D = \sqrt{D\tau}$ , where  $\tau$  is the lifetime, the electron and hole diffusion length ( $L_D$ ) are calculated to be 130 nm and 90 nm respectively with a minimal value.

In comparison, solution-processed organic molecules generally have very small diffusion lengths, typically around 10 nm.<sup>30-32</sup> While colloidal quantum dots (CQDs) films prepared by the layer-by-layer deposition commonly show diffusion lengths of *ca.* 30 nm (cross-linked by small organic molecule), and CQDs film well passivated by inorganic anions can only exhibit a diffusion length of up to *ca.* 80 nm.<sup>33</sup> This shows CH<sub>3</sub>NH<sub>3</sub>PbI<sub>3</sub> film has supreme charge transport properties compared to the other solution-processed semiconductors. On top of this, the electron mobility and hole mobility in CH<sub>3</sub>NH<sub>3</sub>PbI<sub>3</sub> are quite similar, which is very rare. In comparison, in typical BHJ solar cells, they can differ by orders of magnitude which often results in the space charge limited photocurrent.<sup>34</sup> The space charge limited photocurrent will be weak in CH<sub>3</sub>NH<sub>3</sub>PbI<sub>3</sub> thin film, which is beneficial for charge transport and collection. It is believed that such long transport lengths associated with CH<sub>3</sub>NH<sub>3</sub>PbI<sub>3</sub> are attributed to its unique crystal



structure, in which the corner-connected  $\text{PbI}_6$  octahedra forms a three-dimensional framework.<sup>35</sup> Considering the fact that such material also has good optical absorption characteristic,  $\text{CH}_3\text{NH}_3\text{PbI}_3$  is considered as one of the most promising photovoltaic materials.

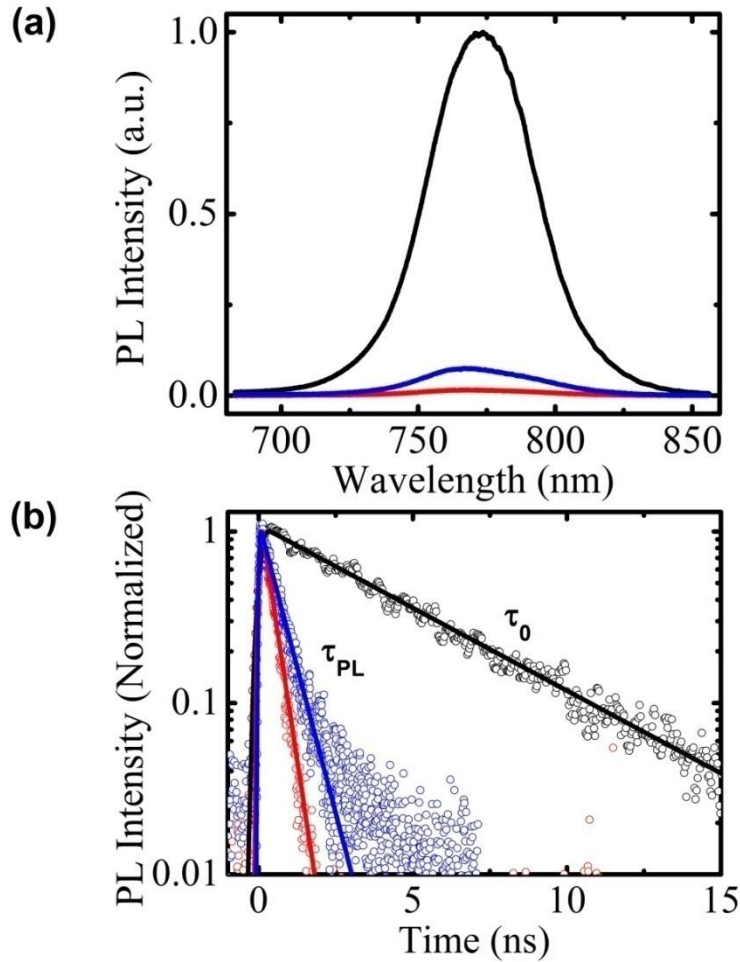


**Figure 4-6:** (a) Steady-state PL spectra and (b) Time-resolved PL decay transients measured at  $760 \pm 10$  nm for  $\text{CH}_3\text{NH}_3\text{PbI}_3$  (black),  $\text{CH}_3\text{NH}_3\text{PbI}_3/\text{PC}_{61}\text{BM}$  (red), and  $\text{CH}_3\text{NH}_3\text{PbI}_3/\text{spiro-OMeTAD}$  (blue) after excitation at 600 nm (1 KHz, 150 fs). The solid lines in B are the single-exponential fit for the PL decay transients.

**Transient absorption spectroscopy (TAS)** TAS measurements were also carried out to reveal more detailed information about the charge carrier dynamics in  $\text{CH}_3\text{NH}_3\text{PbI}_3$  and to validate the accuracy of the results obtained from the direct PL approach as well. To avoid the second order effects (e.g. Auger recombination), low pump fluence is adopted to excite all the samples. The representative transient absorption (TA) spectra of  $\text{CH}_3\text{NH}_3\text{PbI}_3$  film,  $\text{CH}_3\text{NH}_3\text{PbI}_3/\text{PC}_{61}\text{BM}$  film and  $\text{CH}_3\text{NH}_3\text{PbI}_3/\text{spiro-OMeTAD}$  film spanning from the ultraviolet (UV) to near infrared (IR) are shown in Figure 4-7 from a to c. All these films have similar spectra characteristics. When  $\text{CH}_3\text{NH}_3\text{PbI}_3$  is coupled with an electron or hole extraction layer, no additional photobleaching (PB) peaks or photoinduced absorption (PIA) bands are observed in their profiles. Two pronounced long-lived PB bands can be observed at wavelength of 480 nm and 760 nm in all the samples, which are labeled as PB1 and PB2 respectively. These two bleach peaks are located at almost the same spectral positions of the two absorption peaks shown earlier, the intensity of which decrease concurrently over the same time frame. The PB2 peak located at 760 nm can be attributed to the state-filling effect, which includes the hole population of the first valence band maximum (VB1), the electron population of the conduction band minimum (CB1), and the interband stimulated emission. However, it is challenging to assign the band transitions associated with the 480 nm PB1 peak in the first place. There are four possibilities, which are illustrated in Figure 4-8. For scenario A, it can be excluded at first. It is because as the bleaching peak has long life time; lowest energy level (CB1 or VB1) must be involved. In the case for scenario D, it is expected that charge transfer will get involved for such energy level layout (type-II heterojunction) as time progresses, and when that happens, there should be a decrease of PB2 peak (760

nm) accompanied with an increase of PB1 peak (480 nm) over the same time frame after the 600-nm pump excitation. The observation does not show this and hence, this configuration can be excluded too. Therefore the origin of PB1 peak can be either from the VB1-CB2 transition in scenario B or VB2-CB1 transition in scenario C, where CB2 and VB2 are the second lowest energy levels in the conduction band and the valence band respectively. As the 600 nm pump energy (2.07 eV) for the photoexcitation is smaller than the energy of PB1 peak (2.59 eV), only one of the two energy levels in the possible PB transition can be populated. For instance, in the case for VB1-CB2 transition, either VB1 level or CB2 level alone can be involved with the PB1 peak signal. Combining with the evidence that the PB1 peak possesses long-lived nature, the populated energy level should be either VB1 or CB1, which will be discussed in the subsequent section.

Figure 4-7d and Figure 4-7e show the normalized bleaching kinetics of  $\text{CH}_3\text{NH}_3\text{PbI}_3$  film,  $\text{CH}_3\text{NH}_3\text{PbI}_3/\text{PC}_{61}\text{BM}$  bilayer film and  $\text{CH}_3\text{NH}_3\text{PbI}_3/\text{spiro-OMeTAD}$  bilayer film probed at wavelength of 480 nm and 760 nm after photoexcitation at 600 nm. It should be noted that the recombination dynamics at the different probe wavelength are independent of the pump fluence when the Auger recombination are insignificant in the system. For pure  $\text{CH}_3\text{NH}_3\text{PbI}_3$  thin film, its decay transient has a single exponential time constant ( $\tau_{\text{TA}}$ ) of  $5.6 \pm 0.1$  ns after fitting with the data, which is longer than the measured PL lifetime ( $\tau_{\text{PL}}$ ) ( $4.5 \pm 0.3$  ns). The small discrepancy may result from the measurements.

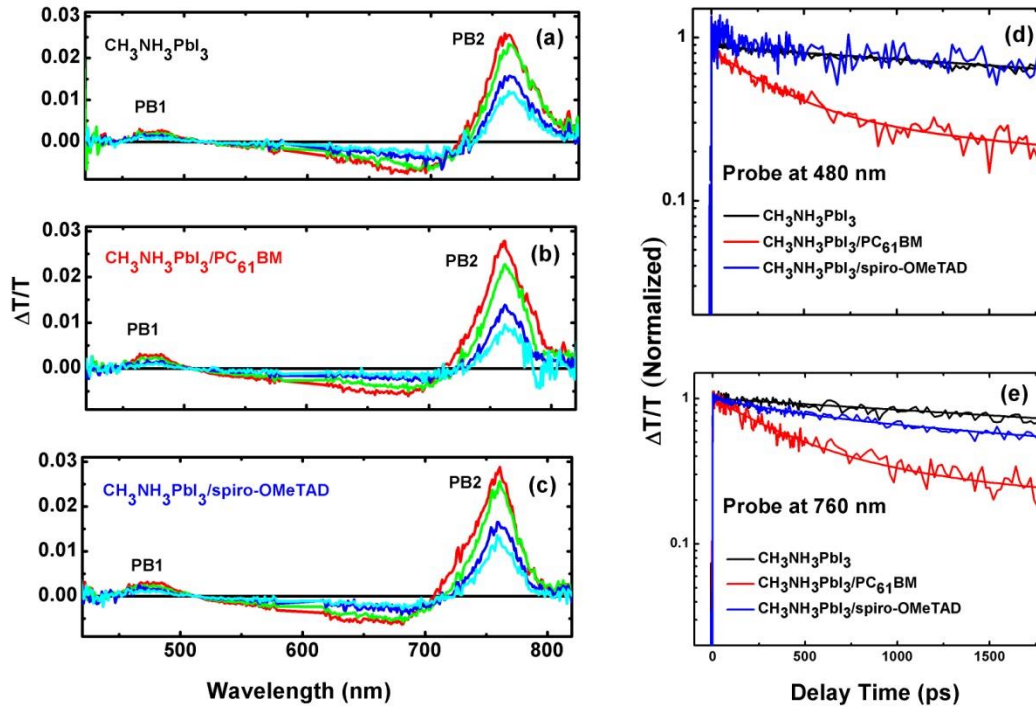


**Figure 4-7:** Differential transmission ( $\Delta T/T$ ) spectra for (a)  $\text{CH}_3\text{NH}_3\text{PbI}_3$ , (b)  $\text{CH}_3\text{NH}_3\text{PbI}_3/\text{PC}_{61}\text{BM}$ , and (c)  $\text{CH}_3\text{NH}_3\text{PbI}_3/\text{spiro-OMeTAD}$  films in vacuum after excitation at 600 nm (1 KHz, 150 fs,  $13 \mu\text{J}/\text{cm}^2$ ) : red (1 ps), green (100 ps), blue (500 ps), and cyan (1 ns). Normalized bleaching kinetics at (d) 480 nm and (e) 760 nm for the films in vacuum after excitation at 600 nm (1 KHz, 150 fs,  $1.3 \mu\text{J}/\text{cm}^2$ ).

For  $\text{CH}_3\text{NH}_3\text{PbI}_3/\text{spiro-OMeTAD}$  bilayer under the 480-nm probe, it exhibits a similar slow decay behavior as the pure  $\text{CH}_3\text{NH}_3\text{PbI}_3$  film, which means the population of the photoexcited carriers in  $\text{CH}_3\text{NH}_3\text{PbI}_3$  is not affected by the presence of spiro-OMeTAD. Considering the hole-extraction nature of spiro-OMeTAD, the photoexcited species can only be electrons so that its population is not affected under such circumstance. As discussed above, the PB1 signal can only come from the population either in VB1 level or CB1 level. Thus, PB1 peak must correspond to the electron population in CB1 (i.e the transition between VB2 and CB1 is involved). This means scenario C in figure 8 should be the right solution for the origin of two PB peaks. And  $\text{CH}_3\text{NH}_3\text{PbI}_3/\text{spiro-OMeTAD}$

bilayer under the 760-nm probe exhibits an additional decay lifetime of  $0.59 \pm 0.03$  ns by a biexponential fitting of its scatterplot, which implies that the hole population of VB1 level can be reflected in the PB2 peak. The TA lifetime obtained here is very similar to the PL lifetime of  $0.64 \pm 0.03$  ns. While when the electron acceptor layer of PC<sub>61</sub>BM is present, both PB1 (under 480-nm probe) and PB2 (under 760-nm probe) bleaching peaks exhibits an additional time constant of  $0.37 \pm 0.02$  ns in the bilayer, which matches well with the measured PL lifetime. As PB1 and PB2 dynamics are simultaneously affected by the electron extraction layer, they are both related with electron population in the CB1. In other words, the electron population in the CB1 level can be reflected in PB2 peak as well as in PB1 peak. In summary, for CH<sub>3</sub>NH<sub>3</sub>PbI<sub>3</sub> under 600-nm pump by the transient absorption study, the PB1 peak can only reflect the electron population in CB1; while the PB2 peak reflects the electron population in CB1 and hole population in VB1.

Similarly, by comparing the decay of the PB2 peak between pure CH<sub>3</sub>NH<sub>3</sub>PbI<sub>3</sub> and CH<sub>3</sub>NH<sub>3</sub>PbI<sub>3</sub>/spiro-OMeTAD, the hole extraction time in the bilayer is calculated to be  $0.66 \pm 0.05$  ns. However, as the PB2 peak is a combination of the signals from both electrons and holes, it is difficult to estimate the detailed hole-extraction efficiency. By comparing the PB1 decays between the pure CH<sub>3</sub>NH<sub>3</sub>PbI<sub>3</sub> and CH<sub>3</sub>NH<sub>3</sub>PbI<sub>3</sub>/PC<sub>61</sub>BM, the electron extraction time and efficiency are determined to  $0.40 \pm 0.05$  ns and 68% respectively. It is also found that about 27% of the photogenerated electrons are possibly trapped and therefore contribute neither to the electron extraction from CH<sub>3</sub>NH<sub>3</sub>PbI<sub>3</sub> to PC<sub>61</sub>BM nor to the radiative recombination by comparing the amplitudes associated with the time constants of the fitting function.

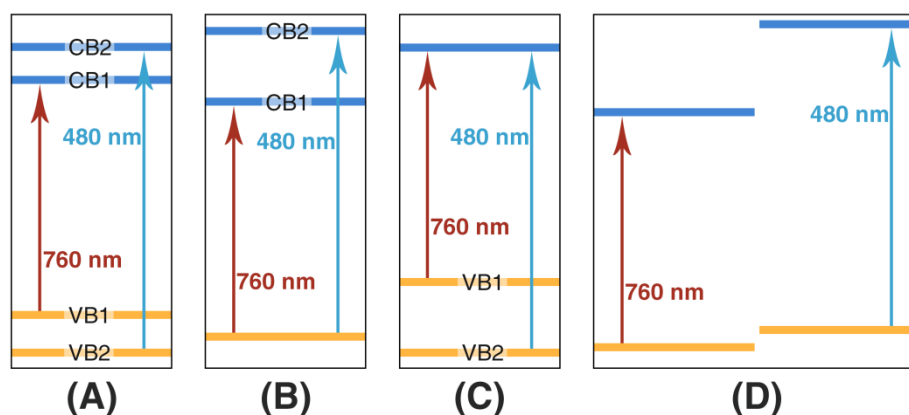


**Figure 4-8:** Schematics of the possible energy levels associated with the two peaks (480 nm and 760 nm) observed in the TA spectra.

The origins of the PB peaks suggest that hot holes generated in  $\text{CH}_3\text{NH}_3\text{PbI}_3$  may undergo fast cooling from the VB2 level to the VB1 level at very short time scale if the sample is excited with higher energy ( $\geq 480$  nm). To validate the proposition, pumps with varied wavelength are used to excite the pure  $\text{CH}_3\text{NH}_3\text{PbI}_3$  sample (400 nm vs 600 nm). Pump with 400-nm wavelength is selected to promote the VB2-CB1 transition. In such circumstance, PB1 can reflect the hole population in VB2 level, which is quite different from that under 600 nm pump excitation. Figure 4-9a shows the early bleaching kinetics in  $\text{CH}_3\text{NH}_3\text{PbI}_3$  film probed both at 480 nm and 760 nm in a time range of less than 3 ps. As observed, after excitation at 400nm, PB1 peak quickly builds up in a time scale close to the 150-fs laser pulse duration, and then decrease in the first  $0.4 \pm 0.1$  ps. The bleach signal at PB2 has a concomitant rise well matched with the decay of PB1 peak. As the decay of the PB1 peak is an indication of the depopulation of hole in VB2 level and the rise of the PB2 peak is an indication of the hole being populated in VB1 level, their synchronization proves that the relaxation of hole from VB2 level to VB1 level indeed

occurs in  $\text{CH}_3\text{NH}_3\text{PbI}_3$  at very early stage. In contrast, the energy of 600-nm pump is only enough to excite carriers in VB2 level; and such hot-hole cooling dynamics are absent. Hot-hole cooling within  $\text{CH}_3\text{NH}_3\text{PbI}_3$  and charge extraction at the  $\text{CH}_3\text{NH}_3\text{PbI}_3/\text{PC}_{61}\text{BM}$  and  $\text{CH}_3\text{NH}_3\text{PbI}_3/\text{spiro-OMeTAD}$  interface are illustrated in Figure 4-9b. This 0.4-ps hot-hole cooling is much slower than that in most organic semiconductors ( $\sim 100$  fs).<sup>29,36</sup> Thus these hot-hole energies could be possibly utilized through optimizing the device configuration before they are wasted.

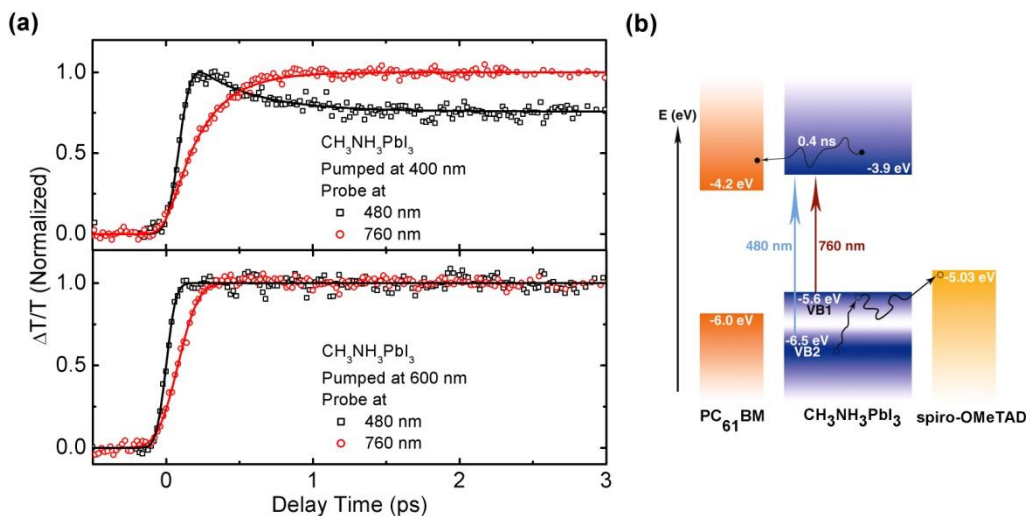


**Figure 4-9:** Normalized bleaching kinetics at 480 and 760 nm in a short time range show the intervalence band hot-hole cooling for  $\text{CH}_3\text{NH}_3\text{PbI}_3$  film after excitation at (a) 400 nm and (B) 600 nm. (b) A schematic illustration the hot-hole cooling and charge recombination within  $\text{CH}_3\text{NH}_3\text{PbI}_3$  and charge separation at the  $\text{CH}_3\text{NH}_3\text{PbI}_3/\text{PC}_{61}\text{BM}$  and  $\text{CH}_3\text{NH}_3\text{PbI}_3/\text{spiro-OMeTAD}$  interfaces. The approximated positions of VB1 and VB2 were obtained from the TA measurement.

Similarly, by fitting the TA decay dynamics with the one dimensional diffusion model, the electron and hole diffusion coefficients in  $\text{CH}_3\text{NH}_3\text{PbI}_3$  are estimated to be 0.036 and 0.022  $\text{cm}^2/\text{s}$ ; and the calculated electron and hole diffusion lengths are 130 nm and 110 nm.

#### 4.2.4 $\text{CH}_3\text{NH}_3\text{PbI}_3$ characteristic in device

**Device structure** As  $\text{CH}_3\text{NH}_3\text{PbI}_3$  exhibits very good optical and electrical properties,  $\text{CH}_3\text{NH}_3\text{PbI}_3$  based solar cells can be expected to perform very well and it would be interesting to elucidate how the device function. To fabricate an efficient solar cell, firstly a suitable electron donor or acceptor must be selected to couple to  $\text{CH}_3\text{NH}_3\text{PbI}_3$ . In this thesis, the main focus is the coupling of  $\text{CH}_3\text{NH}_3\text{PbI}_3$  to an electron accepting material for photovoltaic application. From the section above, we have learned that  $\text{PC}_{61}\text{BM}$  can readily accept electron from  $\text{CH}_3\text{NH}_3\text{PbI}_3$ , and it is also well known that CdSe NCs have a higher electron affinity than  $\text{PC}_{61}\text{BM}$ ; therefore charge transfer in  $\text{CH}_3\text{NH}_3\text{PbI}_3/\text{CdSe}$  NCs may be better, and hence this is would be an interesting material systems to look into for device studies.

Transient absorption (TA) spectroscopic study of the bilayer film was carried out. Figure 4-10a displayed the differential transmission spectra ( $\Delta T/T$ ) of pure  $\text{CH}_3\text{NH}_3\text{PbI}_3$  film,  $\text{CH}_3\text{NH}_3\text{PbI}_3/\text{PC}_{61}\text{BM}$  film, and  $\text{CH}_3\text{NH}_3\text{PbI}_3/\text{CdSe}$  film. It can be observed that the photoexcited species in  $\text{CH}_3\text{NH}_3\text{PbI}_3/\text{CdSe}$  bilayer decay much faster than those in  $\text{CH}_3\text{NH}_3\text{PbI}_3/\text{PC}_{61}\text{BM}$  bilayer and pure  $\text{CH}_3\text{NH}_3\text{PbI}_3$  thin film. The shorter lifetime indicates CdSe can accept electron faster than  $\text{PC}_{61}\text{BM}$ , which means CdSe is a better electron acceptor than  $\text{PC}_{61}\text{BM}$  when coupled to  $\text{CH}_3\text{NH}_3\text{PbI}_3$ .

Solar cells are constructed with device structure:  $\text{ITO}/\text{CdSe}/\text{CH}_3\text{NH}_3\text{PbI}_3/\text{P3HT}/\text{Ag}$ . The energy level diagram for the materials employed in this solar cell is shown in Figure 4-10b. It can be seen that the LUMO and HOMO levels of CdSe are both lying below the conduction and valence bands of  $\text{CH}_3\text{NH}_3\text{PbI}_3$ , forming a type-II heterojunction. To fabricate the device, CdSe NCs were first spincoated onto ITO substrates from the chlorobenzene (CB) and butylamine (BA, 5% v/v) mixture solution. Then, the substrate



was subject to thermal treatment at  $140^\circ\text{C}$  for 20 min to improve the film conductivity by removing capping ligand butylamine between CdSe NCs and the processing solvent (chlorobenzene). Subsequently,  $\text{CH}_3\text{NH}_3\text{PbI}_3$  was deposited on the CdSe film via the spincoating of an equimolar mixture of  $\text{CH}_3\text{NH}_3\text{I}$  and  $\text{PbI}_2$  precursors in dimethylformamide (DMF). To prevent any short-circuit in the device due to direct contact between  $\text{CH}_3\text{NH}_3\text{PbI}_3$  and metal electrode, a very thin layer of P3HT was solution-deposited on top of  $\text{CH}_3\text{NH}_3\text{PbI}_3$  layer. To complete the device, silver was thermally deposited on the active layer to form the cathode. It is expected that the material combination of  $\text{CH}_3\text{NH}_3\text{PbI}_3$  and CdSe NCs can achieve a solution-processed hybrid solar cell with high performance.

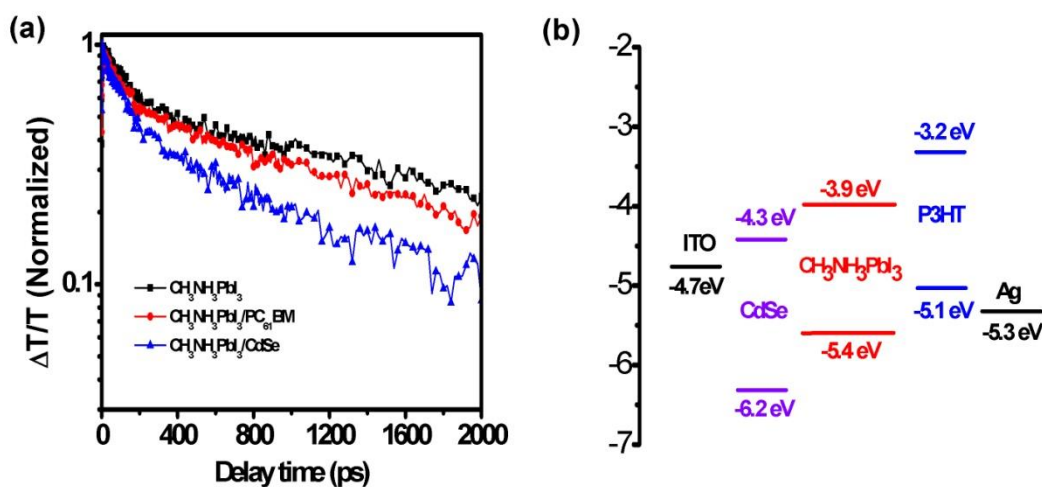


**Figure 4-10:** (a) Differential transmission ( $\Delta T/T$ ) spectra of  $\text{CH}_3\text{NH}_3\text{PbI}_3$  film,  $\text{CH}_3\text{NH}_3\text{PbI}_3/\text{PC}_{61}\text{BM}$  film, and  $\text{CH}_3\text{NH}_3\text{PbI}_3/\text{CdSe}$  film after excitation at 600 nm and probed at 760 nm and (b) Energy level diagram of the CdSe/ $\text{CH}_3\text{NH}_3\text{PbI}_3$  bilayer solar cell.

**Device performance** Figure 4-11 exhibits the  $J$ - $V$  characteristics of solar cells based on CdSe QDs and  $\text{CH}_3\text{NH}_3\text{PbI}_3$  in dark and under the AM1.5G illumination ( $100 \text{ mW}/\text{cm}^2$ ) and their corresponding EQE profiles under low light intensity. The hybrid solar cell

containing CH<sub>3</sub>NH<sub>3</sub>PbI<sub>3</sub> has a good PCE of 2.60%, with  $J_{sc}$  of 8.72 mA/cm<sup>2</sup>,  $V_{oc}$  of 0.88 V and FF of 0.34. In comparison, the bilayer devices based on CdSe (or CdS) and conjugated polymers typically show a PCE of less than 0.5%.<sup>37,38</sup> In general, the  $V_{oc}$  of bilayer solar cells based on conjugated polymers and inorganic NCs or solution-processed all-inorganic NCs solar cells are less than 0.5 V.<sup>39-43</sup> Both  $J_{sc}$  and  $V_{oc}$  in the CdSe/CH<sub>3</sub>NH<sub>3</sub>PbI<sub>3</sub> bilayer devices are considerably higher compare to the conventional polymer/CdSe bilayer cells. These conventional solution-processed hybrid solar cells also have very low  $J_{sc}$ . For instance, Kwon *et al.* have demonstrated hybrid solar cells based on ultrahigh density CdSe nanorod array and P3HT and they displayed a  $J_{sc}$  as low as 3.20 mA/cm<sup>2</sup> even though well aligned arrays were adopted to facilitate the charge transport and charge collection.<sup>37</sup> The ultrahigh  $J_{sc}$  and  $V_{oc}$  observed in CH<sub>3</sub>NH<sub>3</sub>PbI<sub>3</sub>/CdSe solar cells are the result of using CH<sub>3</sub>NH<sub>3</sub>PbI<sub>3</sub> as the main light absorber as it has very good light absorption properties and at the same time, excellent charge transport properties. The deep HOMO level of CH<sub>3</sub>NH<sub>3</sub>PbI<sub>3</sub> results in a high  $V_{oc}$ . Nevertheless, FF of the hybrid solar cells is a bit low, limiting the final device performance. It is well known that series resistance ( $R_s$ ) and the recombination processes in the devices can have a very strong impact on the FF. In this case, the residual insulating ligands (e.g. TOPO) on CdSe NCs reduce the electron mobility in the film and increase  $R_s$  of the devices, contributing to the poor FF. If FF can be improved to about 0.50 by replacing the CdSe layer with a more efficient electron-transporting layer, which is the typical value in BHJ hybrid solar cells, a PCE of more than 4% can be achieved.

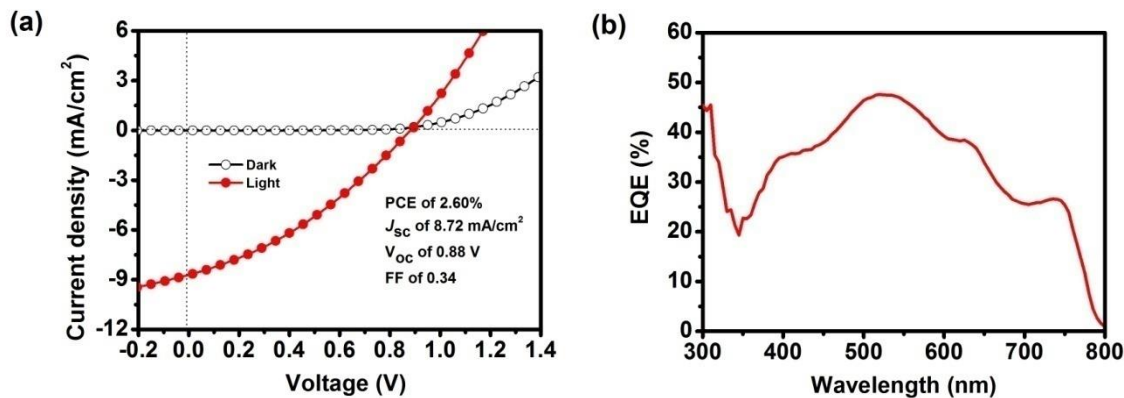
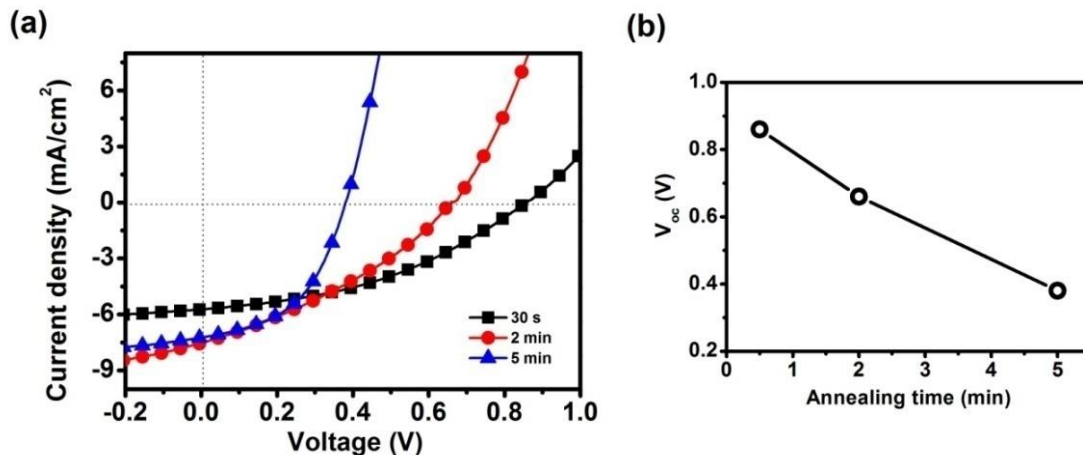


Figure 4-11: (a)  $J$ - $V$  characteristic and (b) EQE profile of CdSe/ $\text{CH}_3\text{NH}_3\text{PbI}_3$  bilayer devices.

**Effect of thermal treatment** Thermal treatment of  $\text{CH}_3\text{NH}_3\text{PbI}_3$  film has been shown as an important step to improve the performance of solid DSSCs where  $\text{CH}_3\text{NH}_3\text{PbI}_3$  is used as the light absorber<sup>44-46</sup> Figure 4-12 showed the  $J$ - $V$  characteristic of CdSe/ $\text{CH}_3\text{NH}_3\text{PbI}_3$  solar cell with  $\text{CH}_3\text{NH}_3\text{PbI}_3$  layer incorporated as the absorber and annealed at  $100^\circ\text{C}$  for 30 s, 2 min and 5 min. It can be observed that the  $V_{\text{oc}}$  of the device decrease as the annealing time increase, and this reduction can be down to half of its original value (from  $0.86 \text{ V}$  to  $0.38 \text{ V}$ ). It can be noted that at short annealing time (i.e. 30 s), the device has the lowest  $J_{\text{sc}}$  of only  $5.7 \text{ mA}/\text{cm}^2$ . At longer annealing times (2 min and 5 min),  $J_{\text{sc}}$  of the devices can be enhanced to more than  $7 \text{ mA}/\text{cm}^2$ . However, the enhancement in  $J_{\text{sc}}$  is offset by the reduction in  $V_{\text{oc}}$ , therefore, the best performance for the device is obtained with the  $\text{CH}_3\text{NH}_3\text{PbI}_3$  layer annealed for 30 s. Excessive annealing time may cause the rearrangement of  $\text{CH}_3\text{NH}_3\text{PbI}_3$  in the solution-cast metastable thin films (i.e. 65 nm) and induce the formation of pinholes which is harmful for  $V_{\text{oc}}$  of the device. The morphology change in  $\text{CH}_3\text{NH}_3\text{PbI}_3$  thin film induced by heat treatment has also been observed by Eperon *et al.*, who found that as-fabricated thin films tend to dewet and agglomerate upon

annealing, and this cause the surface coverage change.<sup>47</sup> Such phenomenon is believed to be driven by surface energy minimization.<sup>18</sup>



**Figure 4-12:** (a)  $J$ - $V$  characteristic and (b) the  $V_{oc}$  trend of  $\text{CH}_3\text{NH}_3\text{PbI}_3/\text{CdSe}$  hybrid solar cells with the  $\text{CH}_3\text{NH}_3\text{PbI}_3$  layer annealed at 30s, 2 min and 5 min.

**Effect of film thickness** The performance of the hybrid solar cell is also strongly influenced by the thickness of the CdSe and P3HT layers adjacent to the  $\text{CH}_3\text{NH}_3\text{PbI}_3$  layer. Figure 4-13a exhibits the  $J$ - $V$  characteristic of  $\text{CH}_3\text{NH}_3\text{PbI}_3$  thin film solar cells with various thickness of CdSe layer. As shown, the  $J_{sc}$  of the device is inversely proportional to the thickness of CdSe film. It is because when the thickness of the film increased, the series resistance ( $R_s$ ) of the whole device increased from  $82 \Omega \text{ cm}^2$  to  $180 \Omega \text{ cm}^2$ . The thickness variation of CdSe layer has less impact on  $V_{oc}$  of the bilayer solar cell instead it is influenced more by the packing of the photoactive materials at the heterojunction. As a result, the device with thinner CdSe layer showed better performance. Figure 4-13b shows the dependence of the device efficiency on the thickness of P3HT layer. It is found that the thinner P3HT layer resulted in a better

performance device due to lower series resistance. However when the thickness of P3HT layer is reduced to below a certain range, the increase in  $J_{sc}$  becomes more insignificant. These two studies demonstrate that the charge transport and recombination in the layers adjacent  $\text{CH}_3\text{NH}_3\text{PbI}_3$  can be quite crucial, which can be the limiting factor for the final device performance.

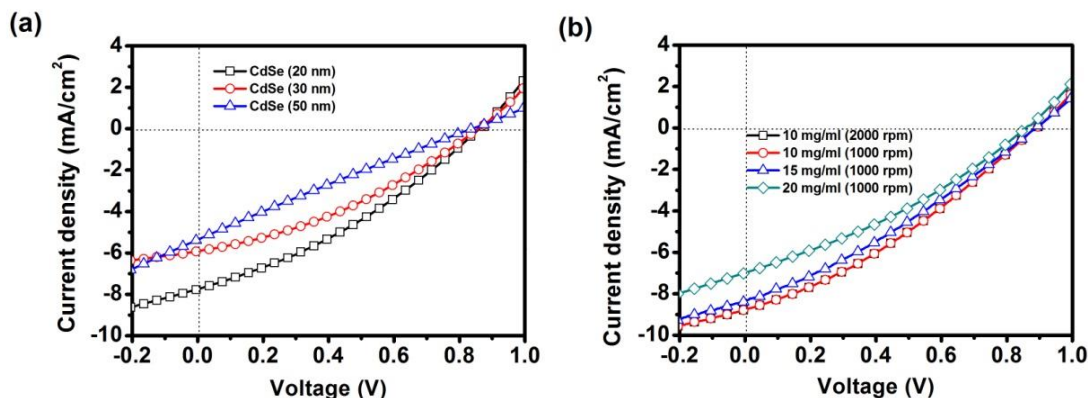


**Figure 4-13:**  $J$ - $V$  characteristic of  $\text{CH}_3\text{NH}_3\text{PbI}_3$  based solar cells with (a) various thickness of CdSe layer or (b) various thickness of P3HT layer.

In summary, to achieve an efficient  $\text{CH}_3\text{NH}_3\text{PbI}_3$  thin film solar cell, the choice of electron acceptor is critical as it determines the efficiency of charge generation and charge extraction. These characteristics can be the bottleneck to a good device performance and negates the superior optoelectronic property of  $\text{CH}_3\text{NH}_3\text{PbI}_3$  when used in a solar cell device. On top of these considerations, the thickness of the neighbouring films in contact with  $\text{CH}_3\text{NH}_3\text{PbI}_3$  layer needs to be optimized to minimize the series resistance of the cells and at the same time to prevent device short-circuiting.

### 4.3 Conclusions

In this chapter, methylammonium lead iodide ( $\text{CH}_3\text{NH}_3\text{PbI}_3$ ) has been synthesized and fully characterized for photovoltaic application. It has been found that  $\text{CH}_3\text{NH}_3\text{PbI}_3$  can be easily deposited to form a smooth thin film with high crystallinity via the spincoating of its precursor solution. We have shown that  $\text{CH}_3\text{NH}_3\text{PbI}_3$  has very good optical properties - a very high optical absorption coefficient and a wide absorption spectrum. In addition, the transient photoluminescence and absorption studies have proven that electron and hole transport lengths in  $\text{CH}_3\text{NH}_3\text{PbI}_3$  are both long range ( $\geq 100$  nm) and quite balanced. The optical absorption length and charge-carrier diffusion length are comparable, which makes  $\text{CH}_3\text{NH}_3\text{PbI}_3$  surpasses the traditional constraints of the other solution-processed semiconductors and becomes a very promising photovoltaic material.  $\text{CH}_3\text{NH}_3\text{PbI}_3$  was also coupled with electron acceptor CdSe NCs to evaluate its performance in a working solar cell. It has been found that solution-processed  $\text{CH}_3\text{NH}_3\text{PbI}_3/\text{CdSe}$  hybrid bilayer solar cell gives decent performance; with considerably high short-circuit current ( $J_{\text{sc}}$ ) and open-circuit current ( $V_{\text{oc}}$ ) concurrently, which is closely linked with the supreme intrinsic properties of  $\text{CH}_3\text{NH}_3\text{PbI}_3$ . The low fill factor (FF), which limits the device performance, is attributed to the high series resistance resulting from the CdSe layer. Nevertheless, the study provides an insight into the behavior of  $\text{CH}_3\text{NH}_3\text{PbI}_3$  in the photovoltaic device and it suggests that through a cautious material selection and combination, a highly efficient solar cell based on  $\text{CH}_3\text{NH}_3\text{PbI}_3$  may be achieved.

## 4.4 Experimental Section

**Materials** The organic salt methylammonium iodide ( $\text{CH}_3\text{NH}_3\text{I}$ ) was synthesized by following the method introduced by Im *et.al.*<sup>16</sup> In the beginning, methylamine (40% in methanol, Sigma) was reacted with hydroiodic acid (57 wt% in water, Sigma) at 0 °C for 2 h with a constant stirring. Secondly,  $\text{CH}_3\text{NH}_3\text{I}$  was crystallized by the slow evaporation of the solvent at 50 °C in the flask. In the end, the white precipitant was washed three times with ethyl ether ( $(\text{C}_2\text{H}_5)_2\text{O}$ , Sigma) and dried in the vacuum oven at 60°C for 24 h. To prepare the thin film of methylammonium lead iodide ( $\text{CH}_3\text{NH}_3\text{PbI}_3$ ),  $\text{CH}_3\text{NH}_3\text{I}$  powder and lead (II) iodide powder ( $\text{PbI}_2$ , Aldrich) were first mixed in the anhydrous solvent of dimethylformamide (DMF, Aldrich) at 1:1 mol ratio and stirred on the hotplate overnight at 60 °C. Before the film casting, the precursor solution (10 wt %) was filtered with a 0.45  $\mu\text{m}$  PVDF filter. [6,6]-Phenyl- $\text{C}_{61}$ -butyric acid methyl ester ( $\text{PC}_{61}\text{BM}$ ) was obtained from Nano-C<sup>®</sup>. The  $\text{PC}_{61}\text{BM}$  films were prepared via the spincoating of a solvent mixture (10 mg  $\text{mL}^{-1}$ ) of anhydrous chlorobenzene (CB, Aldrich) and anhydrous chloroform (CF, Aldrich) (1:1 v/v). (2,2',7,7'-tetrakis(N,-di-p-methoxyphenylamine)-9,9'-spirobifluorene) (spiro-OMeTAD) films were solution casted from a 20 mg/ml solution in chlorobenzene (CB, Aldrich). CdSe nanocrystal (NCs) of *ca.* 4.5 nm was synthesized in the lab. The detail information for the synthesis was reported in the chapter 3. In general, CdSe NCs (25 mg/ml) were dispersed in a solvent mixture of chlorobenzene and butylamine (5% v/v) and spincoated to form the thin film of CdSe. All the materials were used directly without any purification. For all the photophysical studies, the samples were stored in vacuum for more than three days to get rid of any residual solvent (i.e. DMF).

**Material characterization** The absorption spectrum of perovskite film on quartz was measured by a UV-vis-NIR spectrophotometer (Shimadzu UV-3600) with an integrating sphere (ISR-3100). X-ray diffractometer (XRD, Bruker D8 Advance) equipped with a Cu-K $\alpha$  X-ray tube was used to investigate the crystal structure of the CH<sub>3</sub>NH<sub>3</sub>PbI<sub>3</sub> perovskite film. The morphology of the thin film of perovskite was probed by atomic force microscopy (AFM, Asylum MFP-3D-BIO) in tapping-mode, which was equipped with an Al reflex coated AFM probe (Olympus AC240TS) with a spring constant of 2 N m<sup>-1</sup> and tip radius of 9 nm. The spectroscopic data of CH<sub>3</sub>NH<sub>3</sub>PbI<sub>3</sub> thin film was captured by the ellipsometer and processed with the built-in models by CompleteEASE to obtain the refractive indices ( $n$ ,  $k$ ). The thickness of the films was also determined by the Alpha-Step profiler (KLA-Tencor).

During the photophysical measurements, all the samples were kept in an optical cryostat under vacuum. For femtosecond optical spectroscopy, laser source was seeded by a Coherent Vitesse<sup>TM</sup> oscillator (100 fs, 80 MHz) and amplified by a Coherent Legend<sup>TM</sup> regenerative amplifier (150 fs, 1 KHz, 800 nm). Thus, the default laser pulses from the regenerative amplifier's output were 800 nm wavelengths. To obtain 400 nm wavelength laser pulse output, a barium borate (BBO) crystal was used to double the fundamental 800 nm pulses. A Light Conversion TOPAS-C optical parametric amplifier was used to generate 600-nm laser pulses. The emission signal of the samples at a 150° backscattering angle passed a pair of optical lenses and through an optical fiber to reach the spectrometer (Acton, Spectra Pro 2500i) at the terminal, which was detected by a charge coupled device (CCD) camera (Princeton Instruments, Pixis 400B). An Optronis Optoscope<sup>TM</sup> streak camera system with an ultimate temporal resolution of ~10 ps was



used to collect time-resolved PL. For femtosecond transient absorption (TA) experiments, the samples were pumped at 2.07 eV (or 3.1 eV) and probed with a white-light continuum. To generate the probe pulses (420-820 nm), a small portion (~5  $\mu$ J) of the fundamental 800 nm laser pulses was focused into a 2 mm-thick sapphire plate. The linear polarization of the pump pulse was adjusted to be perpendicular to that of the probe pulse with a polarizer and a half waveplate. Any contribution from coherent artifacts at early times will be eliminated by the cross-polarization. A monochromator/PMT configuration with lock-in detection was used to monitor the pump-induced changes of the transmission ( $\Delta T/T$ ) of the probe beam, which was chopped at 83 Hz. Such frequency was adopted as the reference frequency for the lock-in amplifier.

**Device fabrication and characterization** The hybrid solar cells were fabricated with the device configuration of ITO/CdSe/CH<sub>3</sub>NH<sub>3</sub>PbI<sub>3</sub>/P3HT/Ag. At first, the ITO-coated glass substrates (Xinyan Technology Ltd., 7  $\Omega$  sq<sup>-1</sup>) were sequentially cleaned by detergent, deionized (DI) water, acetone and isopropanol (IPA) for 15 min each in the ultrasonic water bath. The ITO substrates were then cleaned by air plasma for 2 min. Following that, PEDOT:PSS (Clevios™ Al 4083) was spin-coated on the ITO substrates to generate a 30-nm-thick thin film. The substrates were then baked at 140 °C for 10 min in a N<sub>2</sub> filled glove box. Subsequently, CdSe thin films were prepared on the ITO substrates via solution casting and baked at 140 °C for 20 min. Afterwards, the perovskite precursor solution was spin-coated onto the CdSe layer. The films were then subjected to a brief heat treatment at 100 °C for 30 s. P3HT solution was then spin-coated on the thin film of CH<sub>3</sub>NH<sub>3</sub>PbI<sub>3</sub>. Finally, silver cathode (~ 60 nm) was formed on the active layer by thermal evaporation under vacuum (10<sup>-6</sup> torr). The active area for each device was 0.07 cm<sup>2</sup>. In

general, more than 20 devices were fabricated for each experimental variable approximately.

The current density-voltage (*J*-*V*) characteristics of the devices were measured by a Keithley SMU 2400 source meter. Solar simulator (SAN-EI Electric) was used to generate the AM 1.5G illumination (100 mW cm<sup>-2</sup>). Before device testing, a digital Solar Meter (Daystar, DS-05A) was used to calibrate the light intensity. Merlin radiometer (Newport) with a monochromator-calibrated wavelength control was used to perform the external quantum efficiency (EQE) measurement and a calibrated silicon photodiode (Hamamatsu) was used to count the incident photons. All the device performance was measured in a N<sub>2</sub> filled glovebox.

## 4.5 References

- (1) Yu, G.; Gao, J.; Hummelen, J. C.; Wudl, F.; Heeger, A. J. *Science* **1995**, 270, 1789.
- (2) Peet, J.; Kim, J. Y.; Coates, N. E.; Ma, W. L.; Moses, D.; Heeger, A. J.; Bazan, G. C. *Nat Mater* **2007**, 6, 497.
- (3) Oosterhout, S. D.; Wienk, M. M.; van Bavel, S. S.; Thiedmann, R.; Jan Anton Koster, L.; Gilot, J.; Loos, J.; Schmidt, V.; Janssen, R. A. J. *Nat Mater* **2009**, 8, 818.
- (4) Campoy-Quiles, M.; Ferenczi, T.; Agostinelli, T.; Etchegoin, P. G.; Kim, Y.; Anthopoulos, T. D.; Stavrinou, P. N.; Bradley, D. D. C.; Nelson, J. *Nat Mater* **2008**, 7, 158.
- (5) Halls, J. J. M.; Pichler, K.; Friend, R. H.; Moratti, S. C.; Holmes, A. B. *Applied Physics Letters* **1996**, 68, 3120.
- (6) Kroeze, J. E.; Savenije, T. J.; Vermeulen, M. J. W.; Warman, J. M. *The Journal of Physical Chemistry B* **2003**, 107, 7696.
- (7) Shaw, P. E.; Ruseckas, A.; Samuel, I. D. W. *Advanced Materials* **2008**, 20, 3516.
- (8) Wei, G.; Lunt, R. R.; Sun, K.; Wang, S.; Thompson, M. E.; Forrest, S. R. *Nano Letters* **2010**, 10, 3555.
- (9) Shin, H. Y.; Woo, J. H.; Gwon, M. J.; Barthelemy, M.; Vomir, M.; Muto, T.; Takaishi, K.; Uchiyama, M.; Hashizume, D.; Aoyama, T.; Kim, D. W.; Yoon, S.; Bigot, J. Y.; Wu, J. W.; Ribierre, J. *C. Physical Chemistry Chemical Physics* **2013**, 15, 2867.
- (10) Mikhnenko, O. V.; Lin, J.; Shu, Y.; Anthony, J. E.; Blom, P. W. M.; Nguyen, T.-Q.; Loi, M. A. *Physical Chemistry Chemical Physics* **2012**, 14, 14196.
- (11) Drain, C. M.; Varotto, A.; Radivojevic, I. *Chemical Reviews* **2009**, 109, 1630.
- (12) Noh, J. H.; Im, S. H.; Heo, J. H.; Mandal, T. N.; Seok, S. I. *Nano Letters* **2013**, 13, 1764.
- (13) Lee, M. M.; Teuscher, J.; Miyasaka, T.; Murakami, T. N.; Snaith, H. J. *Science* **2012**, 338, 643.
- (14) Burschka, J.; Pellet, N.; Moon, S.-J.; Humphry-Baker, R.; Gao, P.; Nazeeruddin, M. K.; Gratzel, M. *Nature* **2013**, 499, 316.
- (15) Kojima, A.; Teshima, K.; Shirai, Y.; Miyasaka, T. *Journal of the American Chemical Society* **2009**, 131, 6050.
- (16) Im, J.-H.; Lee, C.-R.; Lee, J.-W.; Park, S.-W.; Park, N.-G. *Nanoscale* **2011**, 3, 4088.
- (17) Cheng, Z.; Lin, J. *CrystEngComm* **2010**, 12, 2646.
- (18) Thompson, C. V. *Annual Review of Materials Research* **2012**, 42, 399.
- (19) Cesaria, M.; Caricato, A. P.; Martino, M. *J. Opt.* **2012**, 14, 105701.

- (20) Walker, B.; Kim, C.; Nguyen, T.-Q. *Chem. Mat.* **2010**, *23*, 470.
- (21) Park, S. H.; Roy, A.; Beaupre, S.; Cho, S.; Coates, N.; Moon, J. S.; Moses, D.; Leclerc, M.; Lee, K.; Heeger, A. J. *Nat. Photonics* **2009**, *3*, 297.
- (22) Kim, Y.; Cook, S.; Tuladhar, S. M.; Choulis, S. A.; Nelson, J.; Durrant, J. R.; Bradley, D. D. C.; Giles, M.; McCulloch, I.; Ha, C.-S.; Ree, M. *Nat. Mater.* **2006**, *5*, 197.
- (23) Ito, K.; Nakazawa, T. *Jpn. J. Appl. Phys.* **1988**, *27*, 2094.
- (24) Kazmerski, L. L.; Hallerdt, M.; Ireland, P. J.; Mickelsen, R. A.; Chen, W. S. *JVST A: Vacuum, Surfaces, and Films* **1983**, *1*, 395.
- (25) van Duren, J. K. J.; Yang, X.; Loos, J.; Bulle-Lieuwma, C. W. T.; Sieval, A. B.; Hummelen, J. C.; Janssen, R. A. J. *Advanced Functional Materials* **2004**, *14*, 425.
- (26) Beek, W. J. E.; Wienk, M. M.; Janssen, R. A. J. *Advanced Functional Materials* **2006**, *16*, 1112.
- (27) Piris, J.; Dykstra, T. E.; Bakulin, A. A.; Loosdrecht, P. H. M. v.; Knulst, W.; Trinh, M. T.; Schins, J. M.; Siebbeles, L. D. A. *The Journal of Physical Chemistry C* **2009**, *113*, 14500.
- (28) Scully, S. R.; McGehee, M. D. *Journal of Applied Physics* **2006**, *100*, 034907.
- (29) Grancini, G.; Maiuri, M.; Fazzi, D.; Petrozza, A.; Egelhaaf, H. J.; Brida, D.; Cerullo, G.; Lanzani, G. *Nat Mater* **2013**, *12*, 29.
- (30) Lunt, R. R.; Benziger, J. B.; Forrest, S. R. *Advanced Materials* **2010**, *22*, 1233.
- (31) Bruno, A.; Reynolds, L. X.; Dyer-Smith, C.; Nelson, J.; Haque, S. A. *The Journal of Physical Chemistry C* **2013**, *117*, 19832.
- (32) Sim, M.; Shin, J.; Shim, C.; Kim, M.; Jo, S. B.; Kim, J.-H.; Cho, K. *The Journal of Physical Chemistry C* **2013**, *118*, 760.
- (33) Zhitomirsky, D.; Voznyy, O.; Hoogland, S.; Sargent, E. H. *ACS Nano* **2013**, *7*, 5282.
- (34) Blom, P. W. M.; Mihailetschi, V. D.; Koster, L. J. A.; Markov, D. E. *Advanced Materials* **2007**, *19*, 1551.
- (35) Baikie, T.; Fang, Y.; Kadro, J. M.; Schreyer, M.; Wei, F.; Mhaisalkar, S. G.; Graetzel, M.; White, T. J. *Journal of Materials Chemistry A* **2013**, *1*, 5628.
- (36) Jailaubekov, A. E.; Willard, A. P.; Tritsch, J. R.; Chan, W.-L.; Sai, N.; Gearba, R.; Kaake, L. G.; Williams, K. J.; Leung, K.; Rossky, P. J.; Zhu, X. Y. *Nat Mater* **2013**, *12*, 66.
- (37) Kwon, S.; Shim, M.; Lee, J. I.; Lee, T.-W.; Cho, K.; Kim, J. K. *Journal of Materials Chemistry* **2011**, *21*, 12449.
- (38) Aydin Yuksel, S.; Gunes, S.; Guney, H. Y. *Thin Solid Films* **2013**, *540*, 242.

- (39) Yu, D.; Yang, Y.; Durstock, M.; Baek, J.-B.; Dai, L. *ACS Nano* **2010**, *4*, 5633.
- (40) Wood, S.; Franklin, J. B.; Stavrinou, P. N.; McLachlan, M. A.; Kim, J.-S. *Applied Physics Letters* **2013**, *103*, 153304.
- (41) Gur, I.; Fromer, N. A.; Geier, M. L.; Alivisatos, A. P. *Science* **2005**, *310*, 462.
- (42) Rath, A. K.; Bernechea, M.; Martinez, L.; de Arquer, F. P. G.; Osmond, J.; Konstantatos, G. *Nat Photon* **2012**, *6*, 529.
- (43) Loiudice, A.; Rizzo, A.; Grancini, G.; Biasiucci, M.; Belviso, M. R.; Corricelli, M.; Curri, M. L.; Striccoli, M.; Agostiano, A.; Cozzoli, P. D.; Petrozza, A.; Lanzani, G.; Gigli, G. *Energy & Environmental Science* **2013**, *6*, 1565.
- (44) Cai, B.; Xing, Y.; Yang, Z.; Zhang, W.-H.; Qiu, J. *Energy & Environmental Science* **2013**, *6*, 1480.
- (45) Edri, E.; Kirmayer, S.; Cahen, D.; Hodes, G. *The Journal of Physical Chemistry Letters* **2013**, *4*, 897.
- (46) Bi, D.; Yang, L.; Boschloo, G.; Hagfeldt, A.; Johansson, E. M. J. *The Journal of Physical Chemistry Letters* **2013**, *4*, 1532.
- (47) Eperon, G. E.; Burlakov, V. M.; Docampo, P.; Goriely, A.; Snaith, H. J. *Advanced Functional Materials* **2014**, *24*, 151.

# Chapter 5

---

**CH<sub>3</sub>NH<sub>3</sub>PbI<sub>3</sub>:PC<sub>61</sub>BM bilayer solar cells**

## 5.1 Introduction

As discussed in the previous chapter, for a breakthrough in the performance of the state-of-the-art hybrid solar cells (HSCs), a bilayer device structure can be a better choice instead of commonly adopted bulk heterojunction (BHJ) structure. The morphology and interface control of the photoactive layer in BHJ hybrid solar cells have been proven to be critical in determining their device performance but these properties are extremely challenging to optimize since there is a complex interplay between conjugated molecules, capping ligands and inorganic nanocrystals (NCs). Thus, the increase in light absorption and charge generation arising from having a thick absorbing film is largely negated by poor charge transport in the film and collection at the interface. In contrast, due to the simplicity in the bilayer architecture and hence its processing requirements, the photoactive layers in bilayer HSCs can be processed to give good film quality for better charge transport. The bilayer structure has its own drawbacks. Since charge generation occurs only at the donor-acceptor (D-A) interface, those photogenerated excitons created in the region with a distance longer than its exciton diffusion length ( $L_D$ ) will lose their energy and contribute no external power. As a result, the best performance of solution processed hybrid bilayer solar cell so far is only 1.76% based on PbS NCs and a low bandgap conjugated polymer.<sup>1</sup> Apparently, the short diffusion length is the bottleneck parameter of the device performance for bilayer solar cell. The employment of a photovoltaic material of large diffusion length can be an effective approach to boost the charge generation in a solar cell device.

As mentioned earlier, on top of the inherent simplicity of the device layout, such device structure is also beneficial for charge transport and transport collection if the charge

diffusion length is larger than the thickness of the film. Hence to achieve highly efficient bilayer solar cells with high efficiency in exciton dissociation and charge generation, new active materials with good light-absorbing quality (large absorption coefficient) that matches the solar spectrum together with large characteristic exciton diffusion length that is comparable to its absorption depth need be explored.

In recent years, many literatures have shown that hybrid organic-inorganic lead halide perovskite (e.g.  $\text{CH}_3\text{NH}_3\text{PbX}_3$ ,  $\text{X}$  = halogen) can fulfill the requirements of having both good absorption properties and large diffusion lengths and hence giving rise to dye-sensitized solar cells (DSSCs) with high efficiency more than 10%.<sup>2-5</sup> In addition, several studies also suggested that these hybrid perovskite compounds can serve as both light absorber and conductor for charge carriers which is a prerequisite for bilayer solar cells.<sup>6,7</sup> For instance, Etgar *et al.* have demonstrated that heterojunction solar cells with  $\text{CH}_3\text{NH}_3\text{PbI}_3$  coated on mesoporous  $\text{TiO}_2$  can show PCE of 5.5%. However, these cells are constructed using a mesoporous architecture, with an interdigitated donor-acceptor interface rather than using planar surface. Their fabrication process is complex and high temperature of over 300°C is usually involved. Very recently, Liu *et al.* have shown pure bilayer solar cell based on  $\text{CH}_3\text{NH}_3\text{PbI}_3$  which was prepared by thermal evaporation could achieve PCE of 15%.<sup>8</sup> Such finding is very encouraging and it implies  $\text{CH}_3\text{NH}_3\text{PbI}_3$  can function efficiently in the simplest device structure. It is more interesting to know the performance of genuine bilayer solar cell based on solution prepared  $\text{CH}_3\text{NH}_3\text{PbI}_3$ , which will be helpful both for the fundamental research and large scale manufacturing in the future. From the discussion in the previous chapter, it can be seen that electron and hole diffusion lengths in the solution-prepared  $\text{CH}_3\text{NH}_3\text{PbI}_3$  thin



film both are larger than *ca.* 100 nm, which are longer than other solution-processed light harvesting materials used so far. In addition, absorber and donor - CH<sub>3</sub>NH<sub>3</sub>PbI<sub>3</sub> coupled with electron acceptor CdSe QDs was used to study how these solution-processed bilayer hybrid solar cells perform. It has been shown that CH<sub>3</sub>NH<sub>3</sub>PbI<sub>3</sub>/CdSe QDs bilayer solar cells can have reasonable performance with high  $J_{sc}$  and  $V_{oc}$ . Nevertheless, these devices suffer from low FF which is attributed to the inefficient charge transport in the CdSe layer. Both our earlier photoluminescence (PL) quenching study and the report by Abrusci *et al.* suggest that n-type organic semiconductor fullerene and their derivative can act as efficient electron acceptor for hybrid lead halide perovskite, which makes this material combination interesting for the exploration of highly efficient solution-processed bilayer hybrid solar cells.<sup>9</sup>

In this chapter, CH<sub>3</sub>NH<sub>3</sub>PbI<sub>3</sub> is coupled with fullerene derivative [6,6]-phenyl-C<sub>61</sub>-butyric acid methyl ester (PC<sub>61</sub>BM) to demonstrate efficient bilayer hybrid solar cell. TEM, FESEM, and EDX mapping were used to confirm the planar heterojunctions in the devices. To understand the working mechanism of the new bilayer device, the function of the layers between the electrodes is studied and the origin of the high performance in the device is also evaluated by looking at the internal quantum efficiency (IQE). The effect of heat treatment on the properties of CH<sub>3</sub>NH<sub>3</sub>PbI<sub>3</sub> film and the device performance is also presented.

## 5.2 Results and discussions

### 5.2.1 Device structure and materials characterization

**Structure layout and energy level diagram** Figure 5-1 shows the device architecture of the hybrid solar cells made of CH<sub>3</sub>NH<sub>3</sub>PbI<sub>3</sub> and PC<sub>61</sub>BM, and the energy level diagram of all the material components used. As shown in the energy level diagram, photoactive material CH<sub>3</sub>NH<sub>3</sub>PbI<sub>3</sub> and PC<sub>61</sub>BM of the device form type-II heterojunction at the interface, which comply with the basic requirement for a working device. To fabricate the bilayer solar cell, the absorber material - CH<sub>3</sub>NH<sub>3</sub>PbI<sub>3</sub> precursor in polar solvent (dimethylformamide) was first deposited on PEDOT:PSS-coated ITO substrates to form a thin bottom film. Subsequently, the substrates were heat treated at 100°C for 30s to encourage the material conversion from the precursor to the final perovskite material, this transformation will be discussed in more detail later. Next, PC<sub>61</sub>BM was spincoated onto the heat-treated CH<sub>3</sub>NH<sub>3</sub>PbI<sub>3</sub> layer from non-polar solvent (the mixture of chlorobenzene and chloroform) to form a top layer film. As CH<sub>3</sub>NH<sub>3</sub>PbI<sub>3</sub> is soluble only in the polar solvent and non-polar solvent is used to dissolve and cast PC<sub>61</sub>BM, solvent orthogonality ensures that PC<sub>61</sub>BM solution will not remove the bottom CH<sub>3</sub>NH<sub>3</sub>PbI<sub>3</sub> thin film and this film remains intact. After the deposition of PC<sub>61</sub>BM on CH<sub>3</sub>NH<sub>3</sub>PbI<sub>3</sub> layer, no further heat treatment was applied. Thus, interdiffusion between the two adjacent layers at the heterojunction is expected to be minimum. Eventually, aluminum was deposited on the active layer to form the cathode through a shadow mask. The final device has a device structure of ITO/PEDOT:PSS/CH<sub>3</sub>NH<sub>3</sub>PbI<sub>3</sub>/PC<sub>61</sub>BM/Al. The whole device fabrication process is solution-processed except the top metal electrode. The whole cell making process is also carried out at low-temperature, making this cell highly compatible with flexible substrates (e.g. ITO/PET).

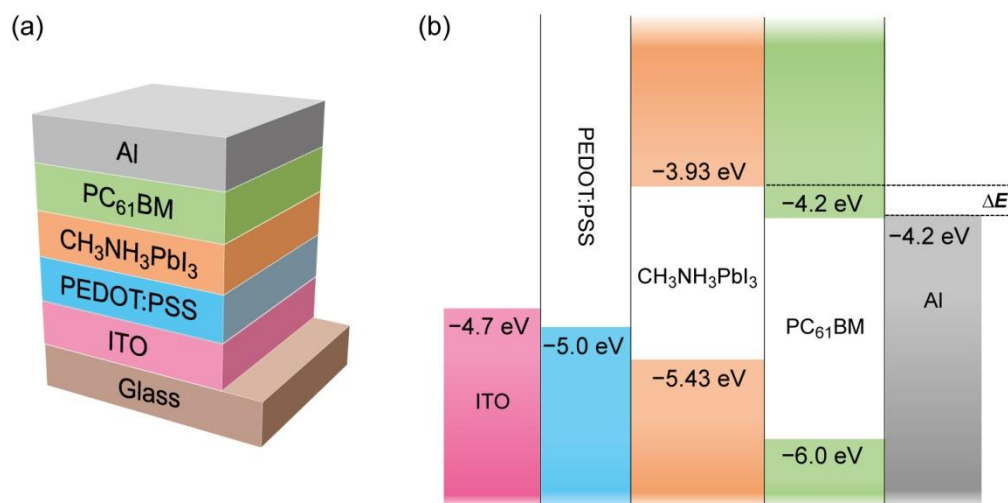


**Figure 5-1:** The schematic drawings of (a) the device layout and (b) the energy level diagram of CH<sub>3</sub>NH<sub>3</sub>PbI<sub>3</sub>/PC<sub>61</sub>BM bilayer solar cell. The energy offset of the LUMO levels of CH<sub>3</sub>NH<sub>3</sub>PbI<sub>3</sub> and PC<sub>61</sub>BM is noted as  $\Delta E$ .

**Characterization of device cross-section** The cross-section of the optimized bilayer solar cell describes previously can be seen in Figure 5-2. The high resolution TEM (HRTEM) image of the active layer showed that the CH<sub>3</sub>NH<sub>3</sub>PbI<sub>3</sub> layer is highly crystalline. Looking at the TEM image, five distinct layers that made up the stack can be clearly identified. This suggests that the all-solution-processed bilayer device indeed shows planar junction architecture with small donor/acceptor (D/A) interface area. Dark spots can be observed in the CH<sub>3</sub>NH<sub>3</sub>PbI<sub>3</sub> layer and these correspond to most probably crystalline material with high atomic number. PEDOT:PSS and PC<sub>61</sub>BM layers are adjacent to CH<sub>3</sub>NH<sub>3</sub>PbI<sub>3</sub> layer. As observed, PC<sub>61</sub>BM forms a continuous layer on top of the CH<sub>3</sub>NH<sub>3</sub>PbI<sub>3</sub> layer and their interface is distinct without the formation of a diffusion region. The bottom layer with huge crystals is the ITO layer while the top bright layer with is Al. The layers can also be distinguished easily in the annular dark-field scanning transmission electron microscopy (ADF-STEM) image with the reversed contrast (shown

in Appendix). The thickness of  $\text{CH}_3\text{NH}_3\text{PbI}_3$  and  $\text{PC}_{61}\text{BM}$  layers are both found to be  $50 \pm 5$  nm. These values agreed well with the data obtained using a surface profilometer. In the HRTEM image of the  $\text{CH}_3\text{NH}_3\text{PbI}_3$  layer (Figure 5-2b), the lattice fringes indicating crystalline regions can be observed surrounded by some amorphous material. These lattice fringes correlate well to the planes of the hybrid material formed by intercalating  $\text{PbI}_2$  and  $\text{CH}_3\text{NH}_3\text{I}$  layers. In addition, the darker contrast observed in the film may correspond either a few overlapping crystallite planes or the existence of planes with different orientations.

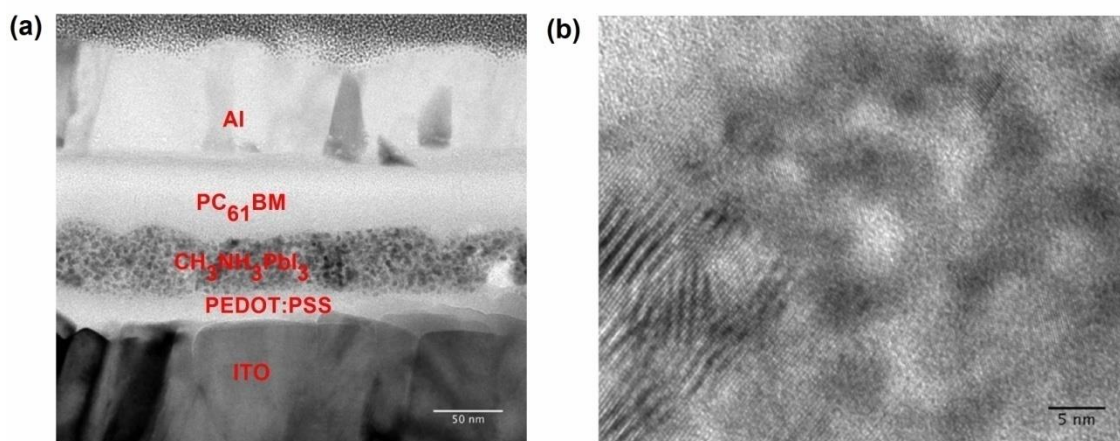


**Figure 5-2:** (a) Cross-sectional TEM image of  $\text{CH}_3\text{NH}_3\text{PbI}_3/\text{PC}_{61}\text{BM}$  bilayer solar cell in the bright-field mode (b) HRTEM image of the  $\text{CH}_3\text{NH}_3\text{PbI}_3$  layer.

**Elemental analysis** Energy-dispersive X-ray spectroscopy (EDX) was used to probe the material composition of the each layer in the device, and the collected EDS spectra are shown in Figure 5-3. As shown, exclusive Pb and I element signals are detected in the middle layer of the device (i.e. the  $\text{CH}_3\text{NH}_3\text{PbI}_3$  layer) and they were not found in the two adjacent layers. This verifies no material interdiffusion occurs between the photoactive

regions in the finished bilayer device. The EDX mapping shown here proves the above assignments of each layer in the device are correct.

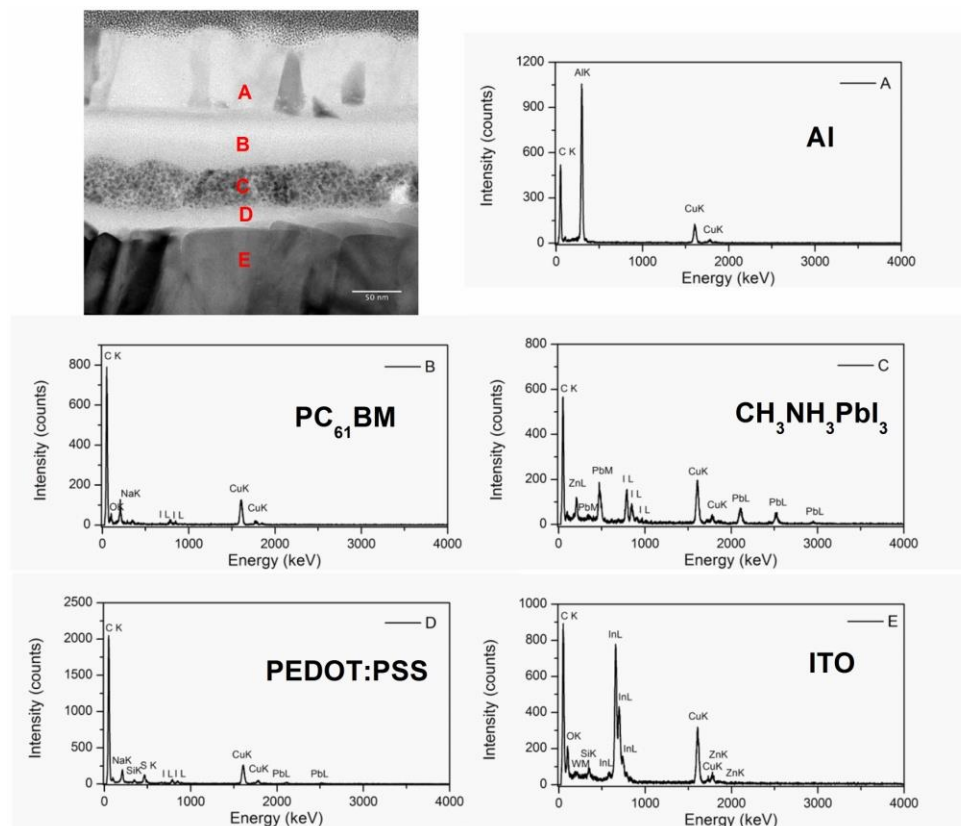


**Figure 5-3:** EDX spectra from the  $\text{CH}_3\text{NH}_3\text{PbI}_3/\text{PC}_{61}\text{BM}$  bilayer solar cell. Areas A-E correspond to regions in the Al,  $\text{PC}_{61}\text{BM}$ ,  $\text{CH}_3\text{NH}_3\text{PbI}_3$ , PEDOT:PSS and ITO layers, respectively.

### 5.2.2 Optical characteristics

Since these perovskite films are used as the active material in a solar cell device, it is critical to understand its absorption characteristics. Figure 5-4 shows the absorption profiles of the standalone  $\text{CH}_3\text{NH}_3\text{PbI}_3$  film, pure  $\text{PC}_{61}\text{BM}$  film, and  $\text{CH}_3\text{NH}_3\text{PbI}_3/\text{PC}_{61}\text{BM}$  bilayer film. The AM 1.5G spectral of solar irradiation is also included as a background reference. It can be seen that  $\text{CH}_3\text{NH}_3\text{PbI}_3$  film can absorb over the whole UV-Vis range with an absorption onset at *ca.* 790 nm. And it has an absorption

peak at *ca.* 360 nm and a shoulder peak at *ca.* 480 nm. In comparison, PC<sub>61</sub>BM film has a much weaker absorption with an absorption peak at *ca.* 330 nm. The bilayer consisting of CH<sub>3</sub>NH<sub>3</sub>PbI<sub>3</sub> and PC<sub>61</sub>BM layers with similar thickness exhibits superposed absorption characteristic of both components, which has a broad absorption window overlapping with the maximum irradiance of the solar spectrum. From this absorption figure and the device layout for the incoming light, it can be concluded that light absorption of the device mainly come from the CH<sub>3</sub>NH<sub>3</sub>PbI<sub>3</sub> layer. In addition, as discussed in the previous chapter, the calculated absorption coefficient ( $\alpha$ ) of the main absorber CH<sub>3</sub>NH<sub>3</sub>PbI<sub>3</sub> film is found to be extremely high, comparable to those of the commonly used conjugated molecules in the highly efficient organic solar cells (e.g. PCDTBT)<sup>10-12</sup> and some inorganic semiconductors (e.g. Cu<sub>2</sub>ZnSnS<sub>4</sub><sup>13</sup> and CuInSe<sub>2</sub><sup>14</sup>). The wide absorption window and large optical absorption coefficient evident from the optical studies mean that photons can be efficiently harvested by the thin CH<sub>3</sub>NH<sub>3</sub>PbI<sub>3</sub> film in the bilayer solar cell, which may eventually lead to a high photocurrent.

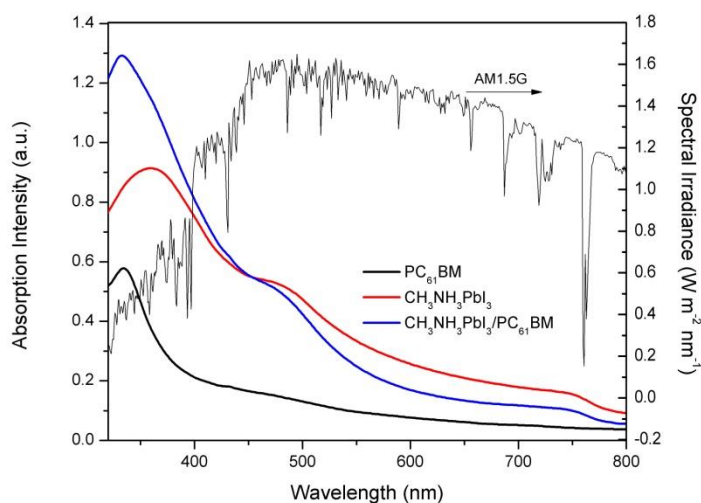


**Figure 5-4:** UV-Vis absorption spectra of standalone CH<sub>3</sub>NH<sub>3</sub>PbI<sub>3</sub> film, pure PC<sub>61</sub>BM film and the CH<sub>3</sub>NH<sub>3</sub>PbI<sub>3</sub>/PC<sub>61</sub>BM bilayer film.

### 5.2.3 Electrical characteristics

Figure 5-5a exhibits the  $J$ - $V$  characteristics of our best CH<sub>3</sub>NH<sub>3</sub>PbI<sub>3</sub>/PC<sub>61</sub>BM bilayer solar cell in the dark and under light illumination (100 mW/cm<sup>2</sup>). The optimal device shows a PCE of 5.23% with a  $J_{sc}$  of 8.20 mA/cm<sup>2</sup>,  $V_{oc}$  of 0.82 V, and FF of 0.77. This efficiency is much higher than that reported by Jeng *et al.*, who shows a similar system with a PCE of 3.9%.<sup>15</sup> Compared to normal bilayer organic/hybrid solar cells with genuine flat heterojunction, the  $J_{sc}$  of our bilayer solar cell is extremely high. The atypical high  $J_{sc}$  may result from the amalgam of a few factors: (1) a wide absorption window, (2) a large optical absorption coefficient, (3) a moderate exciton diffusion length (i.e. thickness comparable to the film thickness, so that almost all the excitons generated can reach the interface) and (4) excellent charge-carrier mobility. The first two factors are strongly related to the optical properties of the main absorber in the device, i.e. the CH<sub>3</sub>NH<sub>3</sub>PbI<sub>3</sub> layer, which is shown to be effective in capturing the incoming photons. The last two factors are greatly determined by the electrical property of the bilayer device as a whole unit, which will be discussed in detail in a later section.

Besides obtaining a remarkable  $J_{sc}$ , the highly efficient bilayer device based on CH<sub>3</sub>NH<sub>3</sub>PbI<sub>3</sub> and PC<sub>61</sub>BM also has high  $V_{oc}$  and FF. The  $V_{oc}$  can be as high as 0.82 V that is close to those reported values for “champion” organic solar cells based on low bandgap materials. For example, the  $V_{oc}$  of those devices based on PTB7:PCBM, PBDTTT-CF:PCBM and PCDTBT:PCBM are 0.74 V,<sup>16</sup> 0.76 V<sup>17</sup> and 0.88 V<sup>18</sup> respectively. In comparison, standard organic solar cells based on wide bandgap polymer P3HT and PCBM only have a  $V_{oc}$  of *ca.* 0.6 V. This is largely due to the high highest-occupied molecular orbital (HOMO) levels of CH<sub>3</sub>NH<sub>3</sub>PbI<sub>3</sub> which is comparable to some known

organic donor materials (i.e. P3HT of -5 eV, PTBT of -5.15 eV, PBDTTT-CF of -5.22 eV, CH<sub>3</sub>NH<sub>3</sub>PbI<sub>3</sub> of -5.43 eV, and PCDTBT of -5.50 eV). It is well known that the  $V_{oc}$  of BHJ organics solar cells can be empirically estimated from the equation:  $V_{oc} \approx (1/e)(|E_{HOMO}^{donor}| - |E_{LUMO}^{acceptor}|)$ . Since CH<sub>3</sub>NH<sub>3</sub>PbI<sub>3</sub> has a high HOMO energy level, the device should give a high photovoltage. Our result suggests that the theoretical  $V_{oc}$  of the devices based on metal halide perovskite and fullerene either in bilayer or BHJ architecture may be calculated from such equation, which is estimated to be 1.23 eV. Since the  $V_{oc}$  in practical is often affected by the charge-carrier recombination rates and the amount of energetic disorder at the interface, it is reasonable to observe that our CH<sub>3</sub>NH<sub>3</sub>PbI<sub>3</sub>/PC<sub>61</sub>BM bilayer devices possess a smaller  $V_{oc}$  than the calculated one.<sup>19</sup>

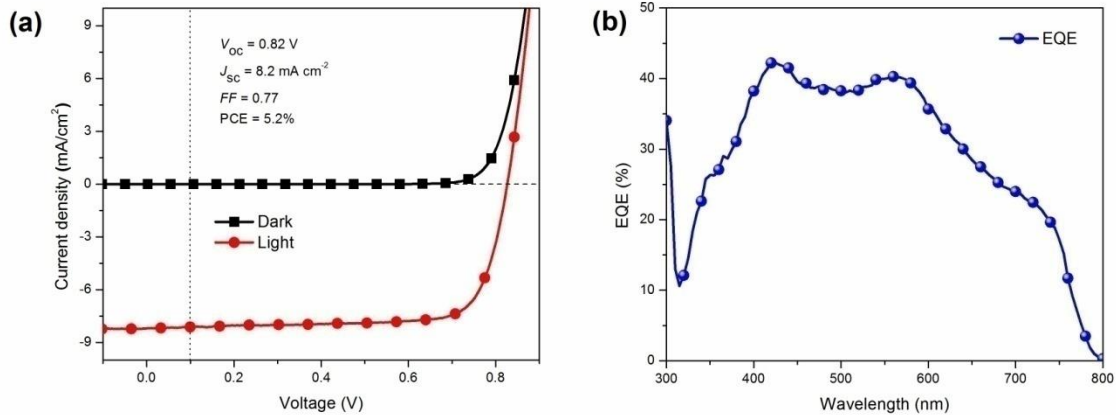


**Figure 5-5:** (a)  $J$ - $V$  characteristic and (b) EQE spectra of ITO/PEDOT:PSS/CH<sub>3</sub>NH<sub>3</sub>PbI<sub>3</sub>/PC<sub>61</sub>BM/Al bilayer solar cell in dark and under AM 1.5G illumination.

In addition, these CH<sub>3</sub>NH<sub>3</sub>PbI<sub>3</sub>/PC<sub>61</sub>BM bilayer solar cells also give rise to high FF of 0.77 that is amongst the highest reported for solution-deposited solar cells. This FF is considered very high as compared to other highly efficient solution-processed solar cells with well-engineered electrode buffer layers which have shown FF of between 0.60 and



0.72 so far.<sup>17,20,21</sup> In contrast, no electron transport layer (ETL) was used in our bilayer solar cells to assist with the charge collection and still such high FF can be achieved. The high FF indicates that the charge transport and charge collection in such bilayer solar cells are very efficient. It has been shown by many research groups that device parameter FF strongly depends on both the series resistance ( $R_s$ ) and shunt resistance ( $R_{sh}$ ) of the solar cell. By extracting the slope of the  $J$ - $V$  curve at around the open-circuit and short-circuit regions,  $R_s$  and  $R_{sh}$  of such bilayer solar cell can be calculated and they are found to be  $6.4 \, \Omega \, \text{cm}^2$  and  $1.6 \, \text{k}\Omega \, \text{cm}^2$  respectively. The low  $R_s$  implied that the charge accumulation and recombination in the device system is negligible during charge transport.

The external quantum efficiency (EQE) profile of this CH<sub>3</sub>NH<sub>3</sub>PbI<sub>3</sub>/PC<sub>61</sub>BM bilayer solar cell is also shown in Figure 5-5b. It can be seen that the EQE signal in such bilayer device is high - 41% at *ca.* 570 nm. The integrated  $J_{sc}$  from the EQE spectra is  $8.04 \, \text{mA}/\text{cm}^2$ , which agrees well with the measured high  $J_{sc}$  under the illumination condition of AM 1.5G.

#### **5.2.4 Role of PC<sub>61</sub>BM and PEDOT:PSS in the device**

From the previous discussion, we know that the photoabsorption event mainly happens in the CH<sub>3</sub>NH<sub>3</sub>PbI<sub>3</sub> layer for the designed bilayer solar cell. The next question will then be if the exciton formed will be able to dissociate into free charges in this planar architecture. As CH<sub>3</sub>NH<sub>3</sub>PbI<sub>3</sub> film form heterojunctions with both PEDOT:PSS and PC<sub>61</sub>BM, it is imperative to understand the role of PEDOT:PSS layer and PC<sub>61</sub>BM layer in the hybrid solar cell. Steady state photoluminescence (PL) measurement was first used

to explore the interactions of CH<sub>3</sub>NH<sub>3</sub>PbI<sub>3</sub> with PEDOT:PSS and PC<sub>61</sub>BM. The photoluminescence spectra of CH<sub>3</sub>NH<sub>3</sub>PbI<sub>3</sub> film, CH<sub>3</sub>NH<sub>3</sub>PbI<sub>3</sub>/PC<sub>61</sub>BM bilayer and CH<sub>3</sub>NH<sub>3</sub>PbI<sub>3</sub>/PEDOT:PSS bilayer is shown in Figure 5-6. The PL intensity of CH<sub>3</sub>NH<sub>3</sub>PbI<sub>3</sub>/PEDOT:PSS bilayer is only about one-fourth of that of CH<sub>3</sub>NH<sub>3</sub>PbI<sub>3</sub> film. When CH<sub>3</sub>NH<sub>3</sub>PbI<sub>3</sub> is coupled with PC<sub>61</sub>BM, the resulting PL intensity is quenched to only only one-seventh of the original signal of its standalone film. This indicates that excitons generated from CH<sub>3</sub>NH<sub>3</sub>PbI<sub>3</sub> can be dissociated at both junctions and the exciton dissociation is much more efficient at the interface between CH<sub>3</sub>NH<sub>3</sub>PbI<sub>3</sub> and PC<sub>61</sub>BM. This finding is in agreement with the conclusion drawn by Abrusci *et al.*, where efficient transfer happens between perovskite and fullerene molecules.<sup>9</sup>

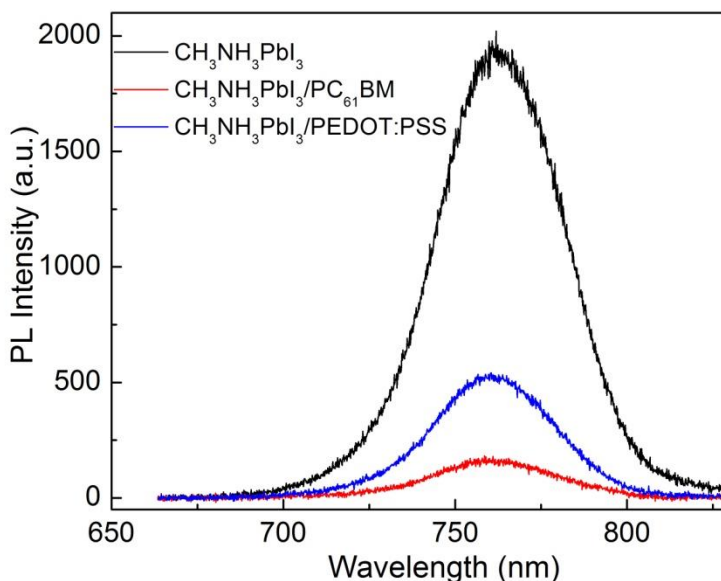


**Figure 5-6:** Steady-state photoluminescence spectra of pure CH<sub>3</sub>NH<sub>3</sub>PbI<sub>3</sub> film, CH<sub>3</sub>NH<sub>3</sub>PbI<sub>3</sub>/PC<sub>61</sub>BM bilayer and CH<sub>3</sub>NH<sub>3</sub>PbI<sub>3</sub>/PEDOT:PSS bilayer ( $\lambda_{\text{ex}} = 600$  nm).

From the PL study, it seems that free charges can be created at the two planar interfaces of CH<sub>3</sub>NH<sub>3</sub>PbI<sub>3</sub> layer. This raises another question as to whether both heterojunctions can contribute to the output photocurrent in the real device. To answer this question, a device without PC<sub>61</sub>BM top layer was fabricated and compared with those devices with PC<sub>61</sub>BM layer. The *J-V* characteristics of CH<sub>3</sub>NH<sub>3</sub>PbI<sub>3</sub> perovskite devices with and without PCBM are shown in Figure 5-7. It can be seen that the ITO/PEDOT:PSS/CH<sub>3</sub>NH<sub>3</sub>PbI<sub>3</sub>/Al device in the absence of PC<sub>61</sub>BM layer behaves only as a diode and shows no significant photovoltaic characteristic. No meaningful power can be extracted from the fourth quadrant of its light *J-V* curve. Nonetheless, several papers have shown that organolead halide has ambipolar characteristics and can work as electron acceptor in the solar cells.<sup>6,22,23</sup> This suggests either the exciton dissociation and charge transfer at PEDOT:PSS/CH<sub>3</sub>NH<sub>3</sub>PbI<sub>3</sub> interface is too weak, or both charge transport and collection is unfavorable due to the energy levels of the two materials. On the other hand, CH<sub>3</sub>NH<sub>3</sub>PbI<sub>3</sub> device with PC<sub>61</sub>BM layer shows typical photovoltaic behavior. It has a PCE of 3.33%, with  $J_{sc}$  of 5.96 mA/cm<sup>2</sup>,  $V_{oc}$  of 0.83 V and FF of 0.67. The remarkable difference in the device performance for the two types of devices is attributed to the lack of efficient exciton dissociating interface in the absence of n-type PC<sub>61</sub>BM. The devices without PEDOT:PSS layer have also been fabricated and tested. It is found that such devices with ITO/CH<sub>3</sub>NH<sub>3</sub>PbI<sub>3</sub>/PC<sub>61</sub>BM/Al structure can perform similarly to those devices with PEDOT:PSS layer, showing slightly higher  $J_{sc}$ . However, shorting of such devices tends to happen easily and the reproducibility of the solar cells is greatly reduced. This is an indication that in the standard ITO/PEDOT:PSS/CH<sub>3</sub>NH<sub>3</sub>PbI<sub>3</sub>/PC<sub>61</sub>BM/Al device, the incorporation of PEDOT:PSS layer can increase the shunt resistance of the

device by preventing direct contact between ITO and perovskite and at the same time, this will also increase their series resistance, considering the high conductivity of perovskite film ( $10^{-3} \text{ S cm}^{-3}$ ).<sup>6</sup>

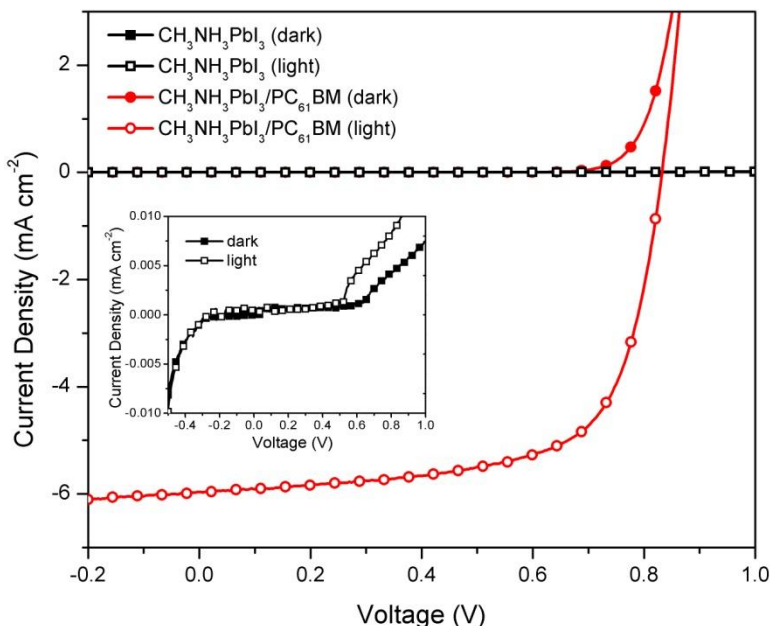


**Figure 5-7:** *J-V* characteristic of CH<sub>3</sub>NH<sub>3</sub>PbI<sub>3</sub> based devices with and without top PC<sub>61</sub>BM layer both in dark and under light. The light and dark electrical characteristics of ITO/PEDOT:PSS/CH<sub>3</sub>NH<sub>3</sub>PbI<sub>3</sub>/Al device are also shown as inset image.

### 5.2.5 Elucidating the reasons for the high device performance

Both PEDOT:PSS and PC<sub>61</sub>BM are essential in the bilayer solar cell of ITO/PEDOT:PSS/CH<sub>3</sub>NH<sub>3</sub>PbI<sub>3</sub>/PC<sub>61</sub>BM/Al for different reasons. The combination of materials and cell architecture gives rise to very high performance in such device. It would be important to find out why this is the case. To do so, it is imperative to look at the internal quantum efficiency (IQE) of this device. IQE can account for the number of charge carrier extracted per photon absorbed by the solar cell. By decoupling the

electronic properties from optical properties, the output photocurrent of the solar cells becomes independent on its light absorption efficiency; as a result, it can provide an insight into the electrical properties of the solar cell. Thus the effectiveness of the bilayer structure to generate photocurrent in our solar cells can be assessed.

The IQE of the bilayer device was calculated using the method discussed by Burkhard *et al.*<sup>24</sup> In this method, the total absorption of the device, which mainly consists of the absorption of the active layer, is measured first. The parasitic absorption of non-active layers (e.g electrode) in the solar cells can be calculated using a model based on the transfer-matrix formalism. With this information, the contribution of the parasitic absorption can be then subtracted from the total absorption to obtain the active absorption of the device. Active absorption is the absorption that is responsible for the charge generation in the device. As this method takes into account factors such as optical interference and light scattering at interface in an actual device, a more precise description of the light absorption in the photoactive layer can be achieved. Besides, this method gives good estimation of active absorption because the main component is the experimentally measured total absorption and this can be measured with high accuracy.

To get the total absorption ( $t_a$ ) of the real device, the total reflectance ( $t_r$ ) of the devices was measured first by using a spectrophotometer with the integrating sphere setup. As  $t_a + t_r + t_t = 1$ , where  $t_t$  is total transmission of the real device, which is taken as 0% as light cannot pass through the thick Al electrode; the total absorption profile can be calculated from the measured reflectance spectrum easily. The measured  $t_r$  and calculated  $t_a$  of our bilayer solar cells are shown in Figure 5-8a. The parasitic absorption of non-active layers, i.e. ITO, PEDOT:PSS, Al, were obtained using the transfer matrix

formalism and their resulting spectrums are shown in Figure 5-8b. For the modeling, all the optical constants (refractive indices  $n$  and  $k$ ) of the materials were obtained from the literature except that CH<sub>3</sub>NH<sub>3</sub>PbI<sub>3</sub> was measured by using an ellipsometer, the detailed discussion of which is presented in the previous chapter.

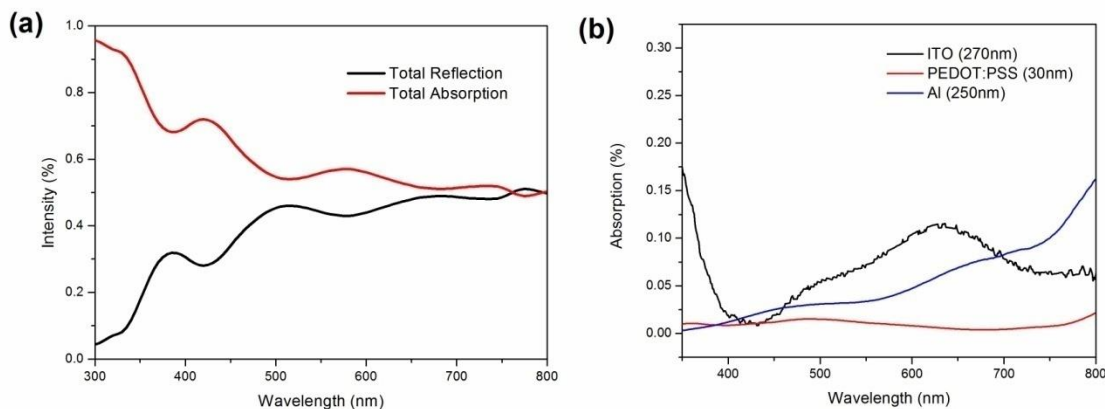


**Figure 5-8:** (a) Total reflection and total absorption spectra of the bilayer solar cell, (b) calculated parasitic absorptions of individual non-active layer ITO, PEDOT:PSS and Al using the transfer-matrix formalism based on device constructure: ITO (270 nm)/PEDOT:PSS (30 nm)/CH<sub>3</sub>NH<sub>3</sub>PbI<sub>3</sub> (45 nm)/PC<sub>61</sub>BM (45 nm)/Al (100 nm).

The active absorption of the photoactive layer is shown in Figure 5-9a, and as described earlier, this was obtained by subtracting the modeled parasitic absorptions from the total absorption. It can be seen that the total absorption at higher wavelength is more influenced by the parasitic absorption. Once the active absorption is found, the IQE can be calculated based on the measured EQE and the active absorption. And this is shown in Figure 5-9b. It can be seen that the IQE of our bilayer solar cell has a maximum peak of 95% at *ca.*580 nm and it is above 90% throughout the whole absorption range between 550 nm and 650 nm.

Considering the photocurrent generation process in the solar cell, IQE can be expressed as:  $IQE = \eta_{ED} * \eta_{CT} * \eta_{CC}$ ; where  $\eta_{ED}$  is the exciton diffusion efficiency,  $\eta_{CT}$  is the charge transfer efficiency, and  $\eta_{CC}$  is charge collection efficiency. The surprisingly high IQE in our bilayer device can be attributed to these three factors. Firstly, the exciton diffusion length ( $L_D$ ) of the main light absorber CH<sub>3</sub>NH<sub>3</sub>PbI<sub>3</sub> is in the same order range of the thickness of its thin film. Besides, the exciton lifetime ( $\tau$ ) in pure CH<sub>3</sub>NH<sub>3</sub>PbI<sub>3</sub> is 5.6 ns.<sup>25</sup> The combination of these two facts increased the probability that the excitons will reach the heterojunction to dissociate into free electron-hole pairs since they can travel a long distance in CH<sub>3</sub>NH<sub>3</sub>PbI<sub>3</sub> before recombination takes place. In comparison, many reports have shown that  $L_D$  in conjugated polymers are only in the range of 2-10 nm<sup>26-28</sup> and  $\tau$  for singlet excitons in organic semiconductors are less than 5 ns.<sup>29</sup>

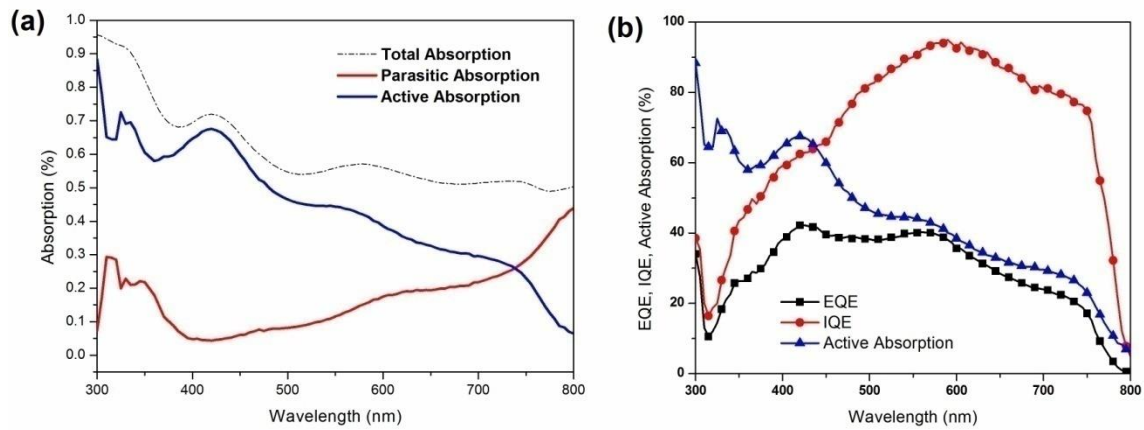


**Figure 5-9:** (a) Parasitic absorption spectra of non-active layers and the active absorption spectra of the bilayer solar cell. The total absorption is also included in comparison. (b) The active absorption, EQE and the resulting IQE profiles of the bilayer solar cell.

Secondly, the charge transfer from CH<sub>3</sub>NH<sub>3</sub>PbI<sub>3</sub> layer to PC<sub>61</sub>BM layer at the heterojunction must be very efficient. This is supported by the photoluminescence (PL)

study shown in the previous section, in which more than 90% of CH<sub>3</sub>NH<sub>3</sub>PbI<sub>3</sub> luminescence signal is quenched in the presence of PC<sub>61</sub>BM. The degree of PL quenching at the planar interface between CH<sub>3</sub>NH<sub>3</sub>PbI<sub>3</sub> and PC<sub>61</sub>BM layers is comparable to those observed in nanoscale phase-separated polymer-fullerene blends,<sup>30,31</sup> which is always an indication of efficient exciton dissociation and charge transfer. It is well known that the exciton binding energy ( $E_b$ ) can have a strong impact on the efficiency of exciton dissociation and charge transfer. Therefore, temperature-dependent photoluminescence measurement was used to probe the  $E_b$  of CH<sub>3</sub>NH<sub>3</sub>PbI<sub>3</sub>. The integrated PL intensity is plotted as a function of the temperature, which is shown in Figure 5-10. The exciton binding energy is estimated to be  $19 \pm 3$  meV, which is extracted by a least square fit of the data curve using the Arrhenius equation:  $I(T) = I_o/[1 + Ae^{(-E_b/K_bT)}]$ . This value is much smaller than those in typical organic semiconductors ( $> 100$  meV),<sup>32</sup> thus a much weaker electric field is required to dissociate the excitons into free charge carriers. In our system, the energy offset between the HOMO level of CH<sub>3</sub>NH<sub>3</sub>PbI<sub>3</sub> and the LUMO level of PC<sub>61</sub>BM provides the driving force to promote the exciton dissociation and electron transfer from the donor CH<sub>3</sub>NH<sub>3</sub>PbI<sub>3</sub> to the acceptor PC<sub>61</sub>BM. The energy level diagram in Figure 5-1 indicates that this energy offset is 0.27 eV, which is more than 10-fold higher than the  $E_b$  of CH<sub>3</sub>NH<sub>3</sub>PbI<sub>3</sub> measured. This means the internal field in the bilayer solar cell is sufficient for exciton dissociation. Furthermore, many literatures have shown that C<sub>60</sub> derivatives tend to have high electron affinity towards electron donating materials due to its deep LUMO level, which is favorable for charge transfer.<sup>33</sup> This suggests excitons in CH<sub>3</sub>NH<sub>3</sub>PbI<sub>3</sub> can split instantaneously at the CH<sub>3</sub>NH<sub>3</sub>PbI<sub>3</sub>/PC<sub>61</sub>BM interface and followed by the electron transfer to the fullerene phase.



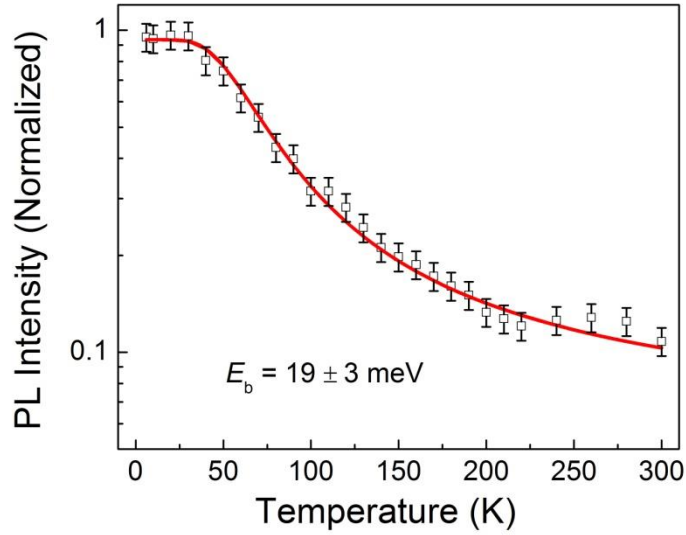


**Figure 5-10:** Temperature-dependent integrated PL intensity of the CH<sub>3</sub>NH<sub>3</sub>PbI<sub>3</sub> film under the excitation of a 532 nm continuous-wave laser beam. The solid line is the best fit based on the Arrhenius equation.

Thirdly, charge transport and charge collection in such system are believed to be efficient. Due to the benefits of its device structure, long-rang charge transport and charge collection in CH<sub>3</sub>NH<sub>3</sub>PbI<sub>3</sub>/PC<sub>61</sub>BM heterojunction solar cells is not an issue as the pathways of holes to the anode and electrons to the cathode are well defined and continuous. Besides, based on the field-effect transistor (FET) measurement reported, the hole mobility of metal halide perovskite and electron mobility of PC<sub>61</sub>BM are very high, which are 0.6 cm<sup>2</sup> v<sup>-1</sup>s<sup>-1</sup> and 1 cm<sup>2</sup> v<sup>-1</sup> s<sup>-1</sup> respectively.<sup>34,35</sup> Therefore, the charge recombination in the bilayer device is expected to be very low.

### 5.2.6 Effect of heat treatment

During the optimization of our bilayer solar cells, it has been noticed that heat treatment has a strong impact on the film property of  $\text{CH}_3\text{NH}_3\text{PbI}_3$ , which is vital for the device performance. This effect will be discussed in this section.

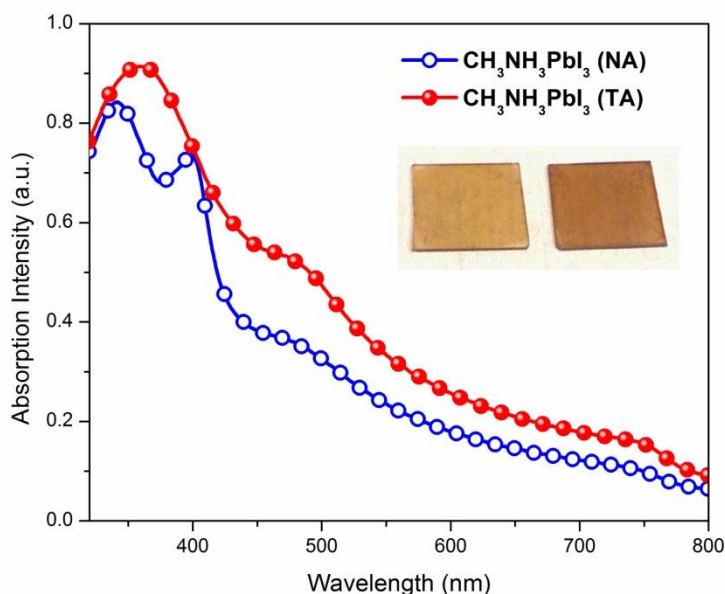


**Figure 5-11:** UV-vis absorption spectra of as-cast (NA) and heat-treated (TA)  $\text{CH}_3\text{NH}_3\text{PbI}_3$  films. The heat treatment was done at 100 °C for 30 s. The inset shows an image of the as-cast (left) and heat-treated (right)  $\text{CH}_3\text{NH}_3\text{PbI}_3$  films.

**Absorption spectroscopy** Figure 5-11 shows the UV-Vis absorption spectra of  $\text{CH}_3\text{NH}_3\text{PbI}_3$  film on quartz substrates before and after heat treatment. The optical images of the corresponding films can be seen in the inset. It is found that the color of  $\text{CH}_3\text{NH}_3\text{PbI}_3$  film becomes darker after a brief heat treatment (within the first 10-20 s), which is reflected in the change of the absorption profiles. As shown in the figure, the as-

cast CH<sub>3</sub>NH<sub>3</sub>PbI<sub>3</sub> film (NA) shows two distinct peaks at *ca.* 340 nm and 400 nm, and a broad shoulder at *ca.* 485 nm in its absorption spectrum. After heat treatment, CH<sub>3</sub>NH<sub>3</sub>PbI<sub>3</sub> film absorbs stronger throughout the UV-Vis range and its absorption onset shifts slightly to the longer wavelength. The heat-treated CH<sub>3</sub>NH<sub>3</sub>PbI<sub>3</sub> film (TA) only exhibits one absorption peak at *ca.* 360 nm. The absorption peak at *ca.* 400 nm can be attributed to the lead iodide (PbI<sub>2</sub>) nanocrystals because of the incomplete conversion of the precursors to the perovskite structure. The disappearance of this peak in the thermally treated CH<sub>3</sub>NH<sub>3</sub>PbI<sub>3</sub> film shows that heat treatment is very effective in the complete transformation of PbI<sub>2</sub> to CH<sub>3</sub>NH<sub>3</sub>PbI<sub>3</sub>. Since the heat-treated sample has stronger and more red-shifted absorption than the as-cast sample, it is expected that its resulting device might generate larger photocurrent.

**Film structure** To probe the crystallinity of the film after heat treatment, TEM was used to investigate the cross-section film morphology of as-cast and heat-treated CH<sub>3</sub>NH<sub>3</sub>PbI<sub>3</sub> films. From the bright-field TEM images of the focused ion beam prepared samples shown in Figure 5-12, dark contrast can be observed for both films, suggesting there are some degree of crystallinity in both the as-cast and the heat-treated CH<sub>3</sub>NH<sub>3</sub>PbI<sub>3</sub> films. This implied that the formation of CH<sub>3</sub>NH<sub>3</sub>PbI<sub>3</sub> perovskite crystals happened immediately upon spincoating of its precursor solution during the film drying. However, the conversion is not fully complete and additional heat treatment is necessary to improve the crystallization in the film. It should be noted that in the bilayer system, the CH<sub>3</sub>NH<sub>3</sub>PbI<sub>3</sub> films were typically heat treated at 100 °C for only 30s before PC<sub>61</sub>BM deposition. Such short heat treatment was sufficient to achieve a complete conversion from the precursor material to the perovskite structure. In comparison, hybrid lead

perovskite coated on mesoporous films of either  $\text{TiO}_2$  or  $\text{Al}_2\text{O}_3$  need to be sintered at high temperature ( $\geq 300^\circ\text{C}$ ) and often for a longer period of more than ten minutes to ensure the complete removal of the solvent.<sup>2,6,36</sup> Our device fabrication methodology is a low-temperature process and can be highly compatible with flexible substrates.

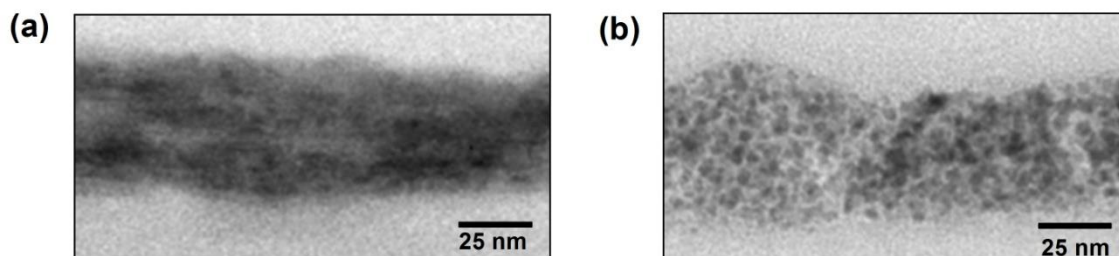


**Figure 5-12:** Cross-sectional TEM images of the as-cast and heat-treated  $\text{CH}_3\text{NH}_3\text{PbI}_3$  films from the corresponding bilayer devices. For comparison, only the perovskite layers are shown.

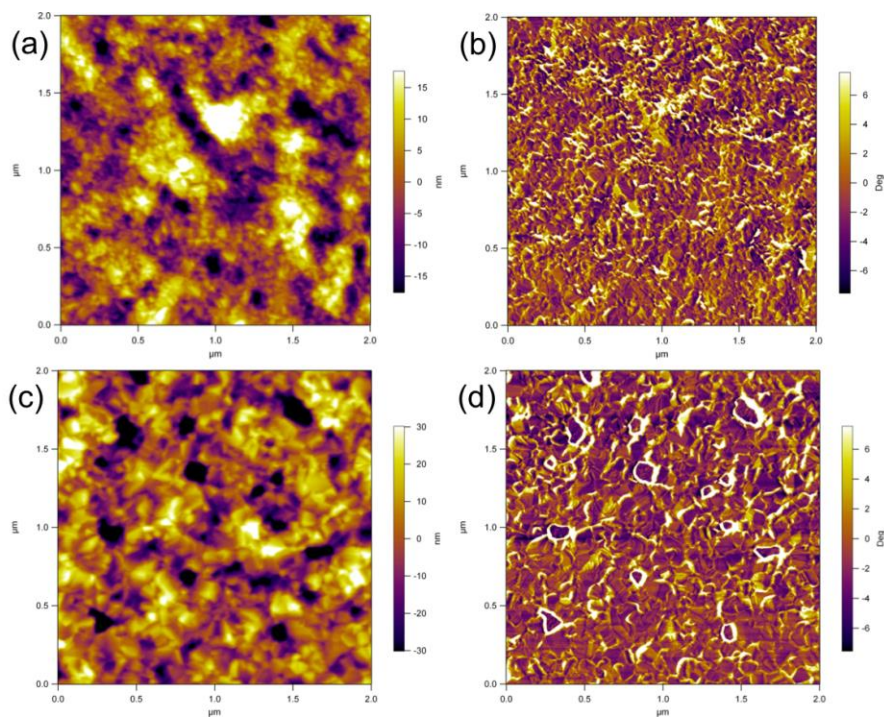


**Figure 5-13:** AFM images of as-cast (a,b) and heat-treated (c,d)  $\text{CH}_3\text{NH}_3\text{PbI}_3$  prepared on ITO/PEDOT:PSS substrates. The images on the left (a,c) are height images, while the images on the right (b,d) are phase images.

**Morphology study** Atomic force microscopy (AFM) was used to study the morphology changes induced by the heat treatment on the CH<sub>3</sub>NH<sub>3</sub>PbI<sub>3</sub> film. From the phase images shown in Figure 5-13, it is found that the grain size increased after the heat treatment. The root-mean-square roughness ( $\sigma_{\text{RMS}}$ ) of CH<sub>3</sub>NH<sub>3</sub>PbI<sub>3</sub> film before and after heat treatment obtained from the height images is 8.5 nm and 14.9 nm, respectively. The increased roughness indicates crystal growth and restructuring may occur during the heat treatment, which manifest as the enhanced crystallinity of the film.

**Device performance** Figure 5-14a exhibits the light  $J$ - $V$  characteristics of the bilayer solar cells based on the as-cast CH<sub>3</sub>NH<sub>3</sub>PbI<sub>3</sub> film and the heat-treated CH<sub>3</sub>NH<sub>3</sub>PbI<sub>3</sub> film, in which the other device processing parameters were the same. As shown, the as-cast device has a PCE of 3.48%, with a  $J_{\text{sc}}$  of 4.65 mA/cm<sup>2</sup>,  $V_{\text{oc}}$  of 1.01 and FF of 0.75. In contrast, after heat treatment, the  $J_{\text{sc}}$  of the device is almost doubled with slight increase in FF while there is a small drop in  $V_{\text{oc}}$  for the device. Eventually, the heat-treated device shows a PCE of 5.23% with a  $J_{\text{sc}}$  of 8.20 mA/cm<sup>2</sup>,  $V_{\text{oc}}$  of 0.82 V, and FF of 0.77. Two possible reasons may account for the big improvement in the  $J_{\text{sc}}$ . Firstly, after the heat treatment, CH<sub>3</sub>NH<sub>3</sub>PbI<sub>3</sub> film has higher crystallinity than before and hence the film has enhanced light absorption and can transport charges better. Secondly, the CH<sub>3</sub>NH<sub>3</sub>PbI<sub>3</sub> film becomes rougher after heat treatment and can have an increased interfacial area with the PC<sub>61</sub>BM layer, which is beneficial for exciton dissociation and charge generation.

The external quantum efficiency (EQE) profiles of both devices are also shown in Figure 5-14b. It can be seen that the heat-treated device has higher EQE response than that of the as-cast bilayer device, which is consistent with the trend of  $J_{\text{sc}}$ . For instance, the highest EQE signal for as-cast device is 30% at *ca.* 440 nm; while the peak EQE signal of the

heat-treated device is 41% at same wavelength. Similar to that of the absorption spectra, the EQE onset of as-cast device is in the lower wavelength region. This suggests as-cast CH<sub>3</sub>NH<sub>3</sub>PbI<sub>3</sub> film may have a wider bandgap. The integrated  $J_{sc}$  of the EQE spectra for as-cast device and heat-treated device is also calculated. They are 4.47 mA/cm<sup>2</sup> and 8.04 mA/cm<sup>2</sup> respectively, which are comparable to the measured values under AM 1.5G light illumination.

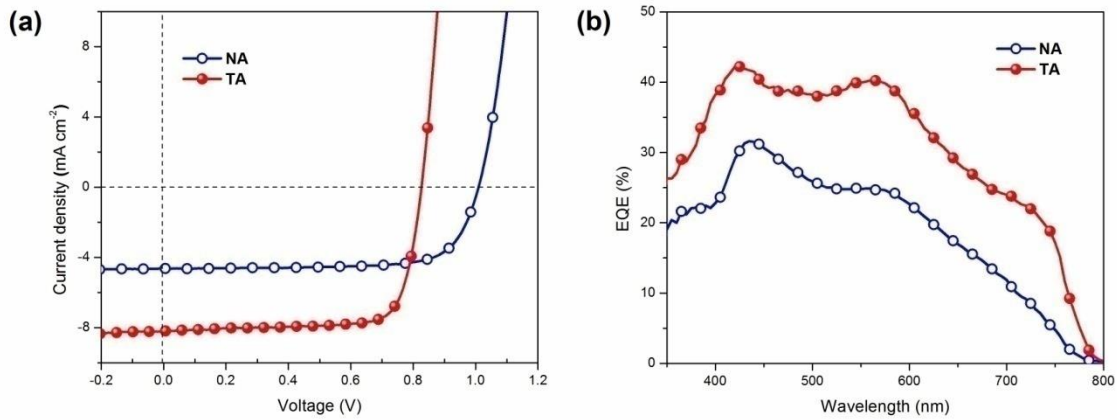


**Figure 5-14:** (a)  $J$ - $V$  characteristic and (b) EQE spectra of the as-cast (NA) and heat-treated (TA) CH<sub>3</sub>NH<sub>3</sub>PbI<sub>3</sub>/PC<sub>61</sub>BM bilayer solar cells under AM 1.5G illumination.

The origin of the higher  $V_{oc}$  in the as-cast device is believed to be related to the precursor component PbI<sub>2</sub> in the preparation of CH<sub>3</sub>NH<sub>3</sub>PbI<sub>3</sub> film. As previously hypothesized, in the as-cast film, some PbI<sub>2</sub> may be present along with the final desired material CH<sub>3</sub>NH<sub>3</sub>PbI<sub>3</sub> as “impurities”. As PbI<sub>2</sub> is a p-type semiconductor with a wide intrinsic bandgap ( $E_g = 2.4$ - $2.5$  eV),<sup>37,38</sup> its presence can increase the bandgap and lower the valence-band maximum of the CH<sub>3</sub>NH<sub>3</sub>PbI<sub>3</sub> film effectively. As a result, the as-cast device has a large  $V_{oc}$ . In comparison, after heat treatment, the remaining PbI<sub>2</sub> can be effectively converted to CH<sub>3</sub>NH<sub>3</sub>PbI<sub>3</sub> in the film and the  $V_{oc}$  of the device is restored to

the “real” value. The slight increase in FF after heat treatment could be correlated with the decreased series resistance ( $R_s$ ) of the bilayer devices. It is found that the  $R_s$  of as-cast device is  $14.9 \Omega \text{ cm}^2$  while the  $R_s$  of heat-treated device is  $6.4 \Omega \text{ cm}^2$ . The change of the series resistance in the device can be attributed to more efficient exciton dissociation, which results from the increased D/A interface and a better charge transport in the CH<sub>3</sub>NH<sub>3</sub>PbI<sub>3</sub> layer owing to its enhanced crystallinity.

### 5.3 Conclusions

In this chapter, a highly efficient bilayer hybrid solar cell has been demonstrated. The device consists of an ultrathin photoactive layer ( $< 100 \text{ nm}$ ). The bilayer structure has been confirmed by examining the cross-section of the devices using both FESEM and TEM. The planar heterojunction device is all solution-processed except the top metal electrode. The device is also fabricated at a low temperature of less than  $150^\circ\text{C}$  which makes it highly compatible with flexible substrates for consumer electronic applications. This bilayer solar cell is achieved by using organolead compound CH<sub>3</sub>NH<sub>3</sub>PbI<sub>3</sub> and n-type organic molecule PC<sub>61</sub>BM as the photoactive materials, and the latter acts as the electron acceptor. The reason behind the high device performance is that the IQE of the bilayer solar cell is close to 100%, which means the photocurrent generation processes including exciton diffusion, charge generation and charge collection are highly efficient. This implied that almost all the absorbed light contributed to the output current in such system.

Our study suggests that perovskite hybrid lead halide compound is a very promising material to achieve low-cost, high efficiency solar cells without the adoption of complex

device structure. In our system, the device performance is only limited by the light harvesting. Besides increasing the film thickness of the CH<sub>3</sub>NH<sub>3</sub>PbI<sub>3</sub> layer, it can be improved simply by the implementation of the antireflection or plasmonic technologies. Although the intrinsic property of CH<sub>3</sub>NH<sub>3</sub>PbI<sub>3</sub> is very good for photovoltaic application, it will be good to replace the toxic lead with other environmentally friendly element for large scale application of such perovskite materials.

## 5.4 Experimental Section

**Materials** Methylammonium iodide (CH<sub>3</sub>NH<sub>3</sub>I) was synthesized in the lab according to the reported literatures.<sup>2</sup> The precursor solution of organolead halide (CH<sub>3</sub>NH<sub>3</sub>PbI<sub>3</sub>) was prepared by mixing as-synthesized CH<sub>3</sub>NH<sub>3</sub>I powder and lead (II) iodide powder (PbI<sub>2</sub>, Aldrich) with a weight ratio of 1:3 in anhydrous dimethylformamide (DMF, Aldrich) solvent. Subsequently, the solution with 9 wt% dissolving materials was stirred on the hotplate overnight at 60 °C. Before device fabrication, the precursor solution was filtered with a 0.45 μm PVDF filter. [6,6]-Phenyl-C<sub>61</sub>-butyric acid methyl ester (PC<sub>61</sub>BM) was obtained from Nano-C<sup>®</sup>. The PC<sub>61</sub>BM (10 mg mL<sup>-1</sup>) solution was prepared in the solvent mixture of anhydrous chlorobenzene (CB, Aldrich) and anhydrous chloroform (CF, Aldrich) (CB:CF = 1:1 v/v). All the materials were used directly without any purification.

**Device fabrication and characterization** Bilayer solar cells were fabricated in the following device configuration: ITO/PEDOT:PSS/CH<sub>3</sub>NH<sub>3</sub>PbI<sub>3</sub>/PC<sub>61</sub>BM/Al. The ITO-coated glass substrates (Xinyan Technology Ltd., 7 Ω sq<sup>-1</sup>) were ultrasonic cleaned by



detergent, deionized water, acetone and isopropanol for 15 min each. Following that, the ITO substrates were exposed for 2 min to air plasma. A layer of 30-nm-thick PEDOT:PSS (Clevios™ Al 4083) layer was spin-coated on ITO and the substrates were then baked at 140 °C for 10 min in a N<sub>2</sub> filled glove box. Subsequently, the perovskite precursor solution was spin-coated onto the PEDOT:PSS layer to yield a film with the thickness *ca.* 45 nm. The films were then heated on the hotplate at 100 °C for 30 s. By default, the CH<sub>3</sub>NH<sub>3</sub>PbI<sub>3</sub> films were always subjected to a brief heat treatment, unless they are specified mentioned. The PC<sub>61</sub>BM solution was spin-coated onto the CH<sub>3</sub>NH<sub>3</sub>PbI<sub>3</sub> layer at 1200 r.p.m. for 60 s to generate the bilayer. No additional heat treatment was needed for the device after the PC<sub>61</sub>BM deposition. Finally, aluminum was deposited on the active layer under vacuum (10<sup>-6</sup> torr) to form the cathode (~ 100 nm). The active area for each device was 0.07 cm<sup>2</sup>. To confirm the results, 20 devices were fabricated for each experimental variable approximately.

The current density-voltage (*J-V*) characteristics of the devices were measured using a Keithley SMU 2400 source meter under AM 1.5G illumination (100 mW cm<sup>-2</sup>) provided by a solar simulator (SAN-EI Electric). Prior the test, the light intensity was calibrated with a digital Solar Meter (Daystar, DS-05A). The external quantum efficiency (EQE) measurement was performed using a Merlin radiometer (Newport) with a monochromator-calibrated wavelength control. The light was coupled into an optical cable (Ocean Optics). To count the incident photons, a calibrated silicon photodiode (Hamamatsu) was used as a reference. All device measurements were carried out in a N<sub>2</sub> filled glovebox.

**Material characterization** The total reflectance profile of the device was measured by a UV-vis-NIR spectrophotometer (Shimadzu UV-3600) with an integrating sphere (ISR-3100). Transfer matrix formalism was used to calculate the parasitic absorption of the non-active layers. For the modeling, the refractive indices ( $n$ ,  $k$ ) of CH<sub>3</sub>NH<sub>3</sub>PbI<sub>3</sub> were measured with an ellipsometer in the lab. For the other materials, they were obtained from the literature.<sup>24</sup>

The surface morphology of the perovskite film was probed by atomic force microscopy (AFM, Asylum MFP-3D-BIO) in tapping-mode with an Al reflex coated AFM probe (Olympus AC240TS), which has a spring constant of 2 N m<sup>-1</sup> and tip radius of 9 nm. The cross-sectional samples were prepared in a dual-beam FEI Helios focused ion beam (FIB) workstation using a standard lift-out procedure. To avoid degradation of the samples due to the Ga<sup>2+</sup> implantation during milling, two consecutive protective layers consisting of ~100 nm of electron-beam-deposited Pt and ~1  $\mu$ m of ion-beam-deposited Pt were applied. The coarse FIB milling was carried out using a 30 kV ion beam, while the final milling was performed at 5 kV ion energy. The angular dark-field scanning transmission electron microscope (ADF-STEM) imaging was performed in a FEI Helios electron microscope (15 kV FEG). The high-resolution transmission electron microscope (HR-TEM) images were obtained using a Philips CM20 TEM (200 kV, FEG) and a FEI Titan (300 kV, FEG). The EDX characterization was performed using a Philips CM20 TEM and an EDAX detector. To measure the thickness of the CH<sub>3</sub>NH<sub>3</sub>PbI<sub>3</sub> layer, both an Alpha-Step profiler (KLA-Tencor) and an AFM were used.

For the time-integrated photoluminescence (TRPL) measurement, a Coherent Legend<sup>TM</sup> regenerative amplifier (150 fs, 1 KHz, 800 nm) that was seeded by a Coherent Vitesse<sup>TM</sup>

oscillator (100 fs, 80 MHz) was used the light source. A Coherent TOPAS-C optical parametric amplifier was used to generate a 600-nm pulse with 150-fs duration. To avoid any second order effects in the dynamics, the fluence was kept to a minimum of  $\sim 1.3 \mu\text{J cm}^{-2}$  per pulse. During the whole measurement, the films were kept in vacuum. The emission from the samples was collected at a backscattering angle of  $150^\circ$  by a pair of lenses and into an optical fiber that was coupled to a spectrometer (Acton, Spectra Pro 2500i) to be detected by a charge-coupled device (Princeton Instruments, Pixis 400B). To determine the exciton binding energy, the temperature dependent photoluminescence (PL) was conducted with the same experimental geometry but with a continuous excitation light source (532 nm,  $\sim 1 \text{ mJ cm}^{-2}$ ).

## 5.5 References:

- (1) Nam, M.; Lee, T.; Kim, S.; Kim, S.; Kim, S.-W.; Lee, K.-K. *Organic Electronics* **2014**, *15*, 391.
- (2) Im, J.-H.; Lee, C.-R.; Lee, J.-W.; Park, S.-W.; Park, N.-G. *Nanoscale* **2011**, *3*, 4088.
- (3) Burschka, J.; Pellet, N.; Moon, S.-J.; Humphry-Baker, R.; Gao, P.; Nazeeruddin, M. K.; Grätzel, M. *Nature* **2013**, *499*, 316.
- (4) Kim, H.-S.; Lee, J.-W.; Yantara, N.; Boix, P. P.; Kulkarni, S. A.; Mhaisalkar, S.; Grätzel, M.; Park, N.-G. *Nano Letters* **2013**, *13*, 2412.
- (5) Kojima, A.; Teshima, K.; Shirai, Y.; Miyasaka, T. *J. Am. Chem. Soc.* **2009**, *131*, 6050.
- (6) Lee, M. M.; Teuscher, J.; Miyasaka, T.; Murakami, T. N.; Snaith, H. J. *Science* **2012**, *338*, 643.
- (7) Etgar, L.; Gao, P.; Xue, Z.; Peng, Q.; Chandiran, A. K.; Liu, B.; Nazeeruddin, M. K.; Grätzel, M. *J. Am. Chem. Soc.* **2012**, *134*, 17396.
- (8) Liu, M.; Johnston, M. B.; Snaith, H. J. *Nature* **2013**, *501*, 395.
- (9) Abrusci, A.; Stranks, S. D.; Docampo, P.; Yip, H.-L.; Jen, A. K. Y.; Snaith, H. J. *Nano Lett.* **2013**, *13*, 3124.
- (10) Walker, B.; Kim, C.; Nguyen, T.-Q. *Chem. Mat.* **2010**, *23*, 470.
- (11) Park, S. H.; Roy, A.; Beaupre, S.; Cho, S.; Coates, N.; Moon, J. S.; Moses, D.; Leclerc, M.; Lee, K.; Heeger, A. J. *Nat. Photonics* **2009**, *3*, 297.
- (12) Kim, Y.; Cook, S.; Tuladhar, S. M.; Choulis, S. A.; Nelson, J.; Durrant, J. R.; Bradley, D. D. C.; Giles, M.; McCulloch, I.; Ha, C.-S.; Ree, M. *Nat. Mater.* **2006**, *5*, 197.
- (13) Ito, K.; Nakazawa, T. *Jpn. J. Appl. Phys.* **1988**, *27*, 2094.
- (14) Kazmerski, L. L.; Hallerdt, M.; Ireland, P. J.; Mickelsen, R. A.; Chen, W. S. *JVST A: Vacuum, Surfaces, and Films* **1983**, *1*, 395.
- (15) Jeng, J.-Y.; Chiang, Y.-F.; Lee, M.-H.; Peng, S.-R.; Guo, T.-F.; Chen, P.; Wen, T.-C. *Advanced Materials* **2013**, *25*, 3727.
- (16) Liang, Y.; Xu, Z.; Xia, J.; Tsai, S.-T.; Wu, Y.; Li, G.; Ray, C.; Yu, L. *Advanced Materials* **2010**, *22*, E135.

- (17) Chen, H.-Y.; Hou, J.; Zhang, S.; Liang, Y.; Yang, G.; Yang, Y.; Yu, L.; Wu, Y.; Li, G. *Nat. Photonics* **2009**, *3*, 649.
- (18) Li, G.; Shrotriya, V.; Huang, J.; Yao, Y.; Moriarty, T.; Emery, K.; Yang, Y. *Nat. Mater.* **2005**, *4*, 864.
- (19) Blakesley, J. C.; Neher, D. *Physical Review B* **2011**, *84*, 075210.
- (20) He, Z.; Zhong, C.; Su, S.; Xu, M.; Wu, H.; Cao, Y. *Nat. Photonics* **2012**, *6*, 591.
- (21) Small, C. E.; Chen, S.; Subbiah, J.; Amb, C. M.; Tsang, S.-W.; Lai, T.-H.; Reynolds, J. R.; So, F. *Nat. Photonics* **2012**, *6*, 115.
- (22) Ball, J. M.; Lee, M. M.; Hey, A.; Snaith, H. J. *Energ. Environ. Sci.* **2013**, *6*, 1739.
- (23) Edri, E.; Kirmayer, S.; Cahen, D.; Hodes, G. *J. Phys. Chem. Lett.* **2013**, *4*, 897.
- (24) Burkhard, G. F.; Hoke, E. T.; McGehee, M. D. *Advanced Materials* **2010**, *22*, 3293.
- (25) Sun, S.; Salim, T.; Mathews, N.; Duchamp, M.; Boothroyd, C.; Xing, G.; Sum, T. C.; Lam, Y. M. *Energy & Environmental Science* **2014**, *7*, 399.
- (26) Markov, D. E.; Tanase, C.; Blom, P. W. M.; Wildeman, J. *Phys. Rev. B* **2005**, *72*, 045217.
- (27) Kroeze, J. E.; Savenije, T. J.; Vermeulen, M. J. W.; Warman, J. M. *J. Phys. Chem. B* **2003**, *107*, 7696.
- (28) Shaw, P. E.; Ruseckas, A.; Samuel, I. D. W. *Advanced Materials* **2008**, *20*, 3516.
- (29) Narayan, M. R.; Singh, J. *Phys. Status Solidi (c)* **2012**, *9*, 2386.
- (30) Hallermann, M.; Kriegel, I.; Da Como, E.; Berger, J. M.; von Hauff, E.; Feldmann, J. *Adv. Funct. Mater.* **2009**, *19*, 3662.
- (31) Wang, H.; Wang, H.-Y.; Gao, B.-R.; Wang, L.; Yang, Z.-Y.; Du, X.-B.; Chen, Q.-D.; Song, J.-F.; Sun, H.-B. *Nanoscale* **2011**, *3*, 2280.
- (32) Arkhipov, V. I.; Bäessler, H. *Phys. Status Solidi (a)* **2004**, *201*, 1152.
- (33) Allemand, P. M.; Koch, A.; Wudl, F.; Rubin, Y.; Diederich, F.; Alvarez, M. M.; Anz, S. J.; Whetten, R. L. *J. Am. Chem. Soc.* **1991**, *113*, 1050.
- (34) Kagan, C. R.; Mitzi, D. B.; Dimitrakopoulos, C. D. *Science* **1999**, *286*, 945.
- (35) Singh, T. B.; Marjanović, N.; Matt, G. J.; Günes, S.; Sariciftci, N. S.; Moutaigne Ramil, A.; Andreev, A.; Sitter, H.; Schwödiauer, R.; Bauer, S. *Org. Electron.* **2005**, *6*, 105.

- (36) Kim, H.-S.; Lee, C.-R.; Im, J.-H.; Lee, K.-B.; Moehl, T.; Marchioro, A.; Moon, S.-J.; Humphry-Baker, R.; Yum, J.-H.; Moser, J. E.; Gratzel, M.; Park, N.-G. *Sci. Rep.* **2012**, 2, 591.
- (37) Gopi, K. K.; Norman, R. D.; Temer, S. A. *J. Phys. D: Appl. Phys.* **2007**, 40, 1778.
- (38) da Silva, A. F.; Veissid, N.; An, C. Y.; Pepe, I.; de Oliveira, N. B.; da Silva, A. V. *B. Appl. Phys. Lett.* **1996**, 69, 1930.

# Chapter 6

---

Summary and Future Work

## 6.1 Summary

Hybrid solar cells (HSCs) combine the advantages of both organic and inorganic materials, and can therefore offer the potential to realize high performance with low cost. Currently, conjugated polymers and inorganic nanocrystals (NCs) are commonly blended together to fabricate solution-processed HSCs, which adopt a bulk heterojunction (BHJ) structure. Compared to organic solar cells (OSCs) based on polymer and fullerene derivative, the performance of state-of-the-art HSCs is low. The main challenge for HSCs is that percolated transport paths for electrons and holes are difficult to achieve simultaneously in the hybrid blend system due to the incompatibility between organic and inorganic materials. Besides, a lack of intimacy between polymer and NCs can impede charge transfer between them. To address these issues, two different approaches have been developed in the hope to improve the performance of solution-processed HSCs.

In the first approach, the use of preformed self-assembled donor nanostructures has been demonstrated. Conjugated polymer P3HT and butylamine capped CdSe NCs were selected for this study. The growth of P3HT nanofiber in solution as a function of time was monitored using optical spectroscopy and AFM. It was found that the absorption intensity of the solution increased with time and remained constant after 24 h. The initial change was associated with the increase in fiber length and density. The width of P3HT nanofiber was comparable to its exciton diffusion length, making it a suitable template to construct ordered hybrid nanostructure. Solution assembled P3HT nanofiber was then integrated into solar cells containing CdSe NCs. As a comparison, device based non-assembled P3HT and CdSe NCs were prepared as well. HSCs based on the fiber system showed better performance than those based on non-fiber system (1.33 % vs 1.07%). The



enhancement in PCE mainly resulted from the increase in  $J_{sc}$ , which was also reflected in their EQE profiles. This was because P3HT nanofibers enhanced light absorption and provided better connectivity within donor domains for charge transport. Although AFM could not reveal significant difference in the surface morphology of the blend films in the two devices since CdSe NCs preferred to be segregated to the top of the films, rougher film in P3HT nanofiber:CdSe devices implied that the interaction between the P3HT nanofiber and CdSe in the film was not perfect.

To improve the interaction between P3HT nanofiber and NCs, pyridine terminated low molecular weight P3HT (P3HT<sub>L</sub>-py) has been synthesized as a compatibilizer via Suzuki coupling. Pyridine moieties were successfully attached to P3HT<sub>L</sub> as confirmed by <sup>1</sup>H NMR, evident by the presence of two distinct proton peaks. It has been shown that the presence of P3HT<sub>L</sub>-py can significantly enhance the colloidal stability of CdSe NCs in solution, and the presence of favorable interaction between P3HT<sub>L</sub>-py and CdSe was also confirmed by XPS. An ordered hybrid nanostructure was prepared by co-assembly of P3HT and P3HT<sub>L</sub>-py in the solution, followed by the attachment of CdSe NCs around the preformed functionalized nanofiber. From the AFM and TEM images, it was revealed that some CdSe NCs were indeed tethered to P3HT nanofibers. When devices were fabricated based on functionalized P3HT nanofiber and CdSe NCs, the PCE increased by more than 20% compared to that of pure P3HT nanofiber:CdSe devices. It was believed that the enhanced performance is related to a more intimate donor-acceptor interface, due to the presence of the additional interaction force.

In another approach, methylammonium lead iodide (CH<sub>3</sub>NH<sub>3</sub>PbI<sub>3</sub>) has been synthesized and explored for photovoltaic application aiming to bypass challenges in the morphology

control in HSCs. Thin films of  $\text{CH}_3\text{NH}_3\text{PbI}_3$  were first characterized by XRD, AFM and optical spectroscopy. It was found that  $\text{CH}_3\text{NH}_3\text{PbI}_3$  thin film had a tetragonal perovskite crystal structure from the XRD studies. AFM images showed that solution-deposited  $\text{CH}_3\text{NH}_3\text{PbI}_3$  could form homogenous and smooth thin films. Optical spectroscopy studies showed that  $\text{CH}_3\text{NH}_3\text{PbI}_3$  thin film had broad absorption window covering almost the whole UV-Vis wavelength range, and a large optical absorption coefficient comparable to or even higher than most of conjugated molecules used in the highly efficient OSCs. In addition, photophysical properties of  $\text{CH}_3\text{NH}_3\text{PbI}_3$  were characterized by ultrafast laser spectroscopy using the surface quenching technique. By fitting the PL decay dynamics in  $\text{CH}_3\text{NH}_3\text{PbI}_3$  with 1-D diffusion equation, diffusion coefficient and length for electrons were calculated to be  $0.037 \text{ cm}^2/\text{s}$  and  $130 \text{ nm}$ ; while holes had a diffusion coefficient of  $0.018 \text{ cm}^2/\text{s}$  and a diffusion length of  $90 \text{ nm}$ . As  $\text{CH}_3\text{NH}_3\text{PbI}_3$  have very similar electron and hole mobilities, the space limited photocurrent will be weak in  $\text{CH}_3\text{NH}_3\text{PbI}_3$  thin film, which is beneficial for charge transport and collection. Transient absorption spectroscopy (TAS) was used to reveal more detailed information of charge carrier dynamics in  $\text{CH}_3\text{NH}_3\text{PbI}_3$ . It has been found that the charges in pure  $\text{CH}_3\text{NH}_3\text{PbI}_3$  thin film has longer lifetime than the one measured using the PL technique. It was because the time-resolved PL technique cannot monitor the recombination of all the photoexcited species in the samples. By comparing the lifetimes of  $\text{CH}_3\text{NH}_3\text{PbI}_3/\text{PC}_{61}\text{BM}$  and  $\text{CH}_3\text{NH}_3\text{PbI}_3/\text{spiro-OMeTAD}$  bilayer films measured by the two techniques, it is found that electrons are the minority charge carriers in  $\text{CH}_3\text{NH}_3\text{PbI}_3$ . In addition, it has been confirmed that hot holes generated in  $\text{CH}_3\text{NH}_3\text{PbI}_3$  can undergo

fast cooling at very short time scale if the sample is excited with higher energy ( $\geq 480$  nm).

A solution processed HSC based on  $\text{CH}_3\text{NH}_3\text{PbI}_3$  and CdSe NCs has been demonstrated since CdSe NCs has been proved to be an efficient electron acceptor for  $\text{CH}_3\text{NH}_3\text{PbI}_3$ . The solar cells could show decent performance of 2.6%; with considerably high  $J_{\text{sc}}$  ( $8.72 \text{ mA/cm}^2$ ) and  $V_{\text{oc}}$  (0.88 V) concurrently, which was attributed to the supreme intrinsic properties of  $\text{CH}_3\text{NH}_3\text{PbI}_3$ . Nevertheless, low FF limited the device performance of such device, which resulted from the high series resistance of the CdSe layer.

To avoid low FF issue in  $\text{CH}_3\text{NH}_3\text{PbI}_3/\text{CdSe}$  HSCs,  $\text{PC}_{61}\text{BM}$  was applied to replace CdSe NCs to fabricate solar cells. The final device has a device structure of ITO/PEDOT:PSS/ $\text{CH}_3\text{NH}_3\text{PbI}_3/\text{PC}_{61}\text{BM}/\text{Al}$ . It has been found that the optimal device based on  $\text{CH}_3\text{NH}_3\text{PbI}_3$  and  $\text{PC}_{61}\text{BM}$  showed a PCE of 5.23% with a  $J_{\text{sc}}$  of  $8.20 \text{ mA/cm}^2$ ,  $V_{\text{oc}}$  of 0.82 V, and FF of 0.77, which is quite amazing considering the adoption of a bilayer device structure. Various characterization techniques have been carried out to understand the working mechanism of the new bilayer device, the function of the active layers, and the origin of the high performance. TEM, FESEM and EDX mapping were used to examine the planarity of the heterojunctions in the device. In the TEM cross-sectional image, five distinct layers stacking on each other could be identified. Only Pb and I element signals could be detected in the perovskite layer of the device from the collected EDS spectra. All these results suggested no material interdiffusion occurred between the photoactive regions in the finished bilayer device. By combining the PL technique and  $J$ - $V$  device characterization, it has been found that excitons generated from  $\text{CH}_3\text{NH}_3\text{PbI}_3$  could be dissociated at both junctions and exciton dissociation was much

more efficient at the interface between  $\text{CH}_3\text{NH}_3\text{PbI}_3$  and  $\text{PC}_{61}\text{BM}$  than that between  $\text{CH}_3\text{NH}_3\text{PbI}_3$  and PEDOT:PSS. Subsequently, the high performance of  $\text{CH}_3\text{NH}_3\text{PbI}_3/\text{PC}_{61}\text{BM}$  bilayer device was investigated. Optical studies found that thin  $\text{CH}_3\text{NH}_3\text{PbI}_3$  film had wide absorption window and large optical absorption coefficient, which may eventually lead to a high photocurrent eventually when it was incorporated into solar cells. IQE of the device was determined to provide an insight into the electrical properties of the solar cell. It has been found that the bilayer device has a high IQE response close to 100%. This means the photocurrent generation processes in the bilayer devices including exciton diffusion, charge generation and charge collection are highly efficient. In addition, the effect of heat treatment on  $\text{CH}_3\text{NH}_3\text{PbI}_3$  on device performance was studied. The absorption and AFM studies showed that some  $\text{PbI}_2$  nanocrystals were present in the as-casted  $\text{CH}_3\text{NH}_3\text{PbI}_3$  film (NA) because of the incomplete conversion of the precursors to the perovskite structure, which could be effectively transformed into  $\text{CH}_3\text{NH}_3\text{PbI}_3$  by heat treatment. As  $\text{PbI}_2$  had a wider intrinsic bandgap and smaller charge mobility, the as-cast device had a large  $V_{oc}$  but lower  $J_{sc}$  compared to thermal-annealed device.

In summary, the application of novel material  $\text{CH}_3\text{NH}_3\text{PbI}_3$  greatly enhanced the performance of solution-processed hybrid solar cells due to its excellent optoelectronic properties, even though simple bilayer structure was adopted. While the performance of hybrid solar cells based on P3HT and CdSe was still limited even though bottom-up self-assembly approach was applied to enhance the morphology. Better understanding of the interaction between conjugated polymer and inorganic nanocrystals is needed to achieve a well-assembled morphology for high performance BHJ hybrid solar cells.

## 6.2 Future Work

This work has demonstrated two different approaches to improve the performance of solution-processed hybrid solar cells. The first one focuses on morphology and interface control in BHJ structure; while the latter one introduces a novel hybrid material with unique properties that is suitable to be used in a bilayer solar cell. Based on the present study, several future works are recommended:

(i) Improve hybrid nanostructure. The formation of P3HT/CdSe hybrid nanostructure is dependent on the interaction force between functionalized P3HT nanofiber and CdSe NCs. It is essential to control the type, density and distribution of the functional groups in the preassembled P3HT nanofibers to achieve a well-organized hybrid nanostructure. Low molecular weight P3HT (P3HT<sub>L</sub>) functionalized with other ligand moiety (e.g. thiol) can be investigated to improve the favorable interaction and charge transfer efficiency between polymer and NCs. The density of functional groups may be controlled by varying the ratio of functionalized P3HT<sub>L</sub> and P3HT, while the distribution of functional groups may be tuned by the sequence of the mixing of these materials during the co-assembly process. Besides, the size and shape of CdSe NCs can be varied so that hybrid nanostructure with different morphology can be achieved. It is interesting to compare the electronic and optoelectronic behaviors of these different hybrid nanostructures.

(ii) Investigate new electron and hole transporting materials for CH<sub>3</sub>NH<sub>3</sub>PbI<sub>3</sub>. Currently, the choice of good new electron and hole transporting materials for CH<sub>3</sub>NH<sub>3</sub>PbI<sub>3</sub> is very limited. PC<sub>61</sub>BM and hole transport material spiro-OMeTAD are two of the most studied materials to date. However, they are expensive and not stable. Cheaper and good materials need be explored for large-scale production. The search can begin with those

semiconducting materials developed for transistors and light emitting devices (LED). Nanocarbon (e.g. carbon nanotubes, graphene) and their composites can be another intriguing class of materials to explore. Besides, as  $\text{CH}_3\text{NH}_3\text{PbI}_3$  absorbs relative weak at high wavelength, materials with strong absorption in this region can be focused on, which may be beneficial for charge generation and device performance when they are coupled with  $\text{CH}_3\text{NH}_3\text{PbI}_3$ .

(iii) Investigate interfacial charge transfer between  $\text{CH}_3\text{NH}_3\text{PbI}_3$  and  $\text{PC}_{61}\text{BM}$ . As shown in chapter five, charge transfer between  $\text{CH}_3\text{NH}_3\text{PbI}_3$  and  $\text{PC}_{61}\text{BM}$  is very efficient. It is also known that exciton binding energy in  $\text{CH}_3\text{NH}_3\text{PbI}_3$  is weak, free charges and excitons will coexist in  $\text{CH}_3\text{NH}_3\text{PbI}_3$  thin film at room temperature. The effect of these species for charge separation, transport, and recombination during device operation is also unknown. More transient spectroscopy studies need be carried out to understand these fundamental events. It would be very interesting to look at the dependence of charge separation between  $\text{CH}_3\text{NH}_3\text{PbI}_3$  and fullerene molecules on the driving force provided by their LUMO difference, by coupling  $\text{CH}_3\text{NH}_3\text{PbI}_3$  with fullerene molecules bearing different LUMO levels considering excitons presence in these systems are weakly bound.

### List of Publications

1. **Sun, S.**; Salim, T.; Mathews, N.; Duchamp, M.; Boothroyd, C.; Xing, G.; Sum, T. C.; Lam, Y. M., The origin of high efficiency in low-temperature solution-processable bilayer organometal halide hybrid solar cells. *Energy & Environmental Science* **2014**, 7 (1), 399-407.
2. Xing, G.; Mathews, N.; **Sun, S.**; Lim, S. S.; Lam, Y. M.; Grätzel, M.; Mhaisalkar, S.; Sum, T. C., Long-Range Balanced Electron- and Hole-Transport Lengths in Organic-Inorganic CH<sub>3</sub>NH<sub>3</sub>PbI<sub>3</sub>. *Science* **2013**, 342 (6156), 344-347.
3. Sonar, P.; Tan, H.-S.; **Sun, S.**; Lam, Y. M.; Dodabalapur, A., Isoindigo dye incorporated copolymers with naphthalene and anthracene: promising materials for stable organic field effect transistors. *Polymer Chemistry* **2013**, 4 (6), 1983-1994.
4. **Sun, S.**; Li, H.; Salim, T.; Bomma, S.; Grimsdale, A. C.; Lam, Y. M., Conjugated polymers based on dicarboxylic imide-substituted isothianaphthene and their applications in solar cells. *Journal of Polymer Science Part A: Polymer Chemistry* **2012**, 50 (2), 250-260.
5. Lim, Z. B.; Li, H.; **Sun, S.**; Lek, J. Y.; Trewin, A.; Lam, Y. M.; Grimsdale, A. C., New 3D supramolecular Zn(ii)-coordinated self-assembled organic networks. *Journal of Materials Chemistry* **2012**, 22 (13), 6218-6231.
6. Kurniawan, M.; Salim, T.; Tai, K. F.; **Sun, S.**; Sie, E. J.; Wu, X.; Yeow, E. K. L.; Huan, C. H. A.; Lam, Y. M.; Sum, T. C., Carrier Dynamics in Polymer Nanofiber: Fullerene Solar Cells. *The Journal of Physical Chemistry C* **2012**, 116 (34), 18015-18022.
7. **Sun, S.**; Salim, T.; Wong, L. H.; Foo, Y. L.; Boey, F.; Lam, Y. M., A new insight into controlling poly(3-hexylthiophene) nanofiber growth through a mixed-solvent approach for organic photovoltaics applications. *Journal of Materials Chemistry* **2011**, 21 (2), 377-386.
8. Salim, T.; Yin, Z.; **Sun, S.**; Huang, X.; Zhang, H.; Lam, Y. M., Solution-Processed Nanocrystalline TiO<sub>2</sub> Buffer Layer Used for Improving the Performance of Organic Photovoltaics. *ACS Applied Materials & Interfaces* **2011**, 3 (4), 1063-1067.
9. Lim, Z. B.; Xue, B.; Bomma, S.; Li, H.; **Sun, S.**; Lam, Y. M.; Belcher, W. J.; Dastoor, P. C.; Grimsdale, A. C., New moderate bandgap polymers containing alkoxy-substituted-benzo[c][1,2,5]thiadiazole and thiophene-based units. *Journal of Polymer Science Part A: Polymer Chemistry* **2011**, 49 (20), 4387-4397.
10. Yin, Z.; **Sun, S.**; Salim, T.; Wu, S.; Huang, X.; He, Q.; Lam, Y. M.; Zhang, H., Organic Photovoltaic Devices Using Highly Flexible Reduced Graphene Oxide Films as Transparent Electrodes. *ACS Nano* **2010**, 4 (9), 5263-5268.
11. Salim, T.; **Sun, S.**; Wong, L. H.; Xi, L.; Foo, Y. L.; Lam, Y. M., The Role of Poly(3-hexylthiophene) Nanofibers in an All-Polymer Blend with a Polyfluorene Copolymer for Solar Cell Applications. *The Journal of Physical Chemistry C* **2010**, 114 (20), 9459-9468.
12. **Sun, S.**; Li, H.; Mhaisalkar, S.; Zin, M.; Lam, Y. M.; Grimsdale, A. C. A high voltage solar cell using a donor-acceptor conjugated polymer based on pyrrolo[3,4-f]-2,1,3-benzothiadiazole-5,7,-dione. *Journal of Materials Chemistry A* (Under review)

## Appendix

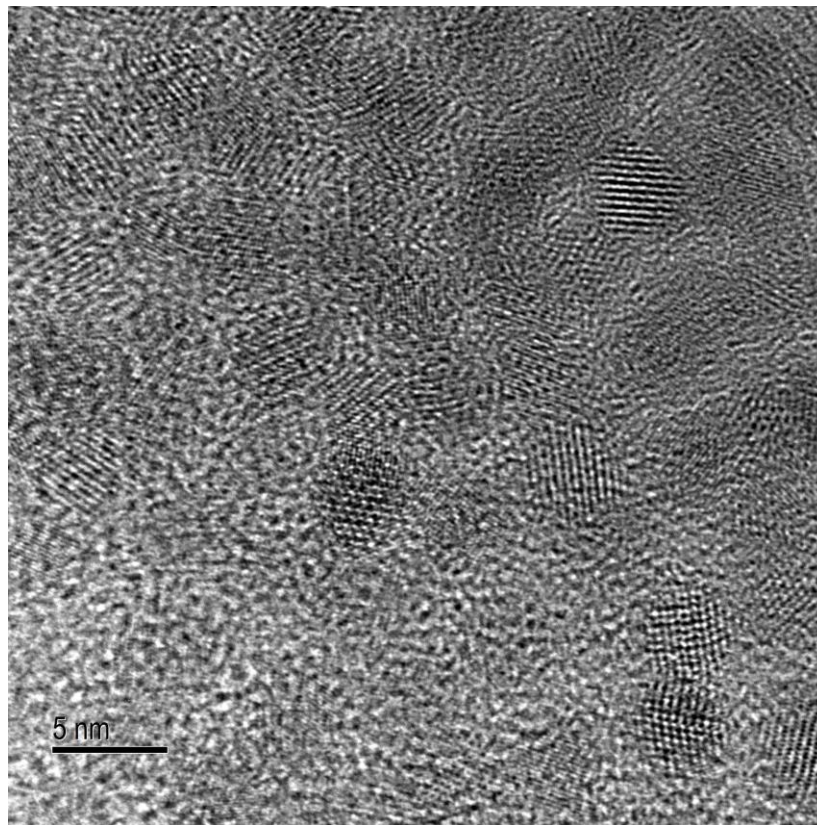


**Figure S1:** TEM image of CdSe nanocrystals (large)

The lattice spacing of the nanocrystals (NCs) was calculated to be 0.353 nm, which agree well with the spacing of the (101) planes of wurtzite CdSe reported.<sup>1</sup>

To obtain the lattice spacing, a ruler was first used to measure the distance of two lines far away in arbitrary five spots of the enlarged image, and the length of the scale bar ( $L_s$ ). Second, the spacing of two adjacent lines ( $d$ ) was calculated by dividing the total distance of the two outmost lines ( $D$ ) to the number of line spacing ( $N$ ) (i.e.  $d = D/N$ ). At last, the lattice spacing was calculated by multiplying the line spacing ( $d$ ) by a factor ( $10 \text{ nm}/L_s$ ).

<sup>1</sup> Li *et al.*, Journal of Nanomaterials, 2012, 2012, 6.



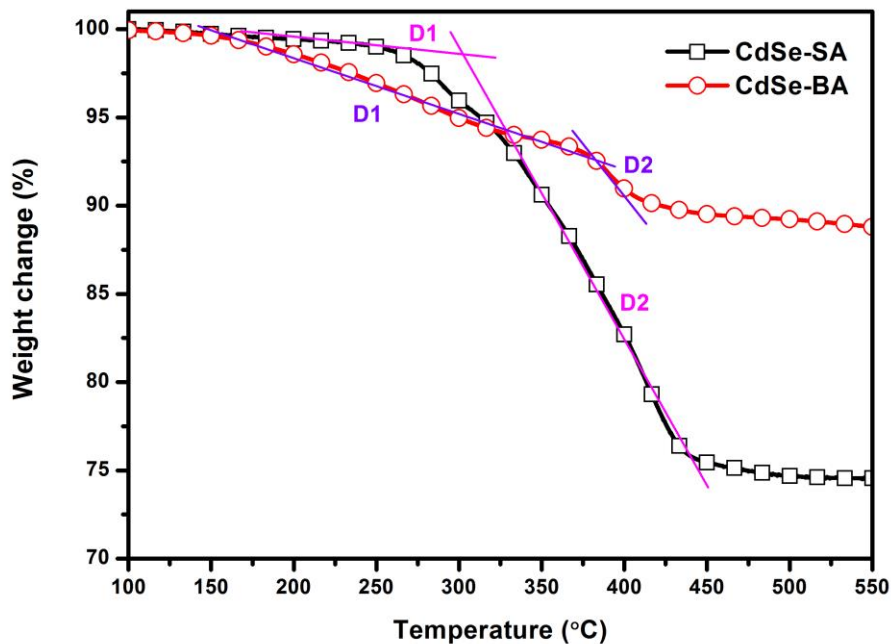


**Figure S2:** TGA plots of CdSe NCs before ligand exchange (CdSe-SA) and after ligand exchange (CdSe-BA) (marked)

The line gradients of the two regions in CdSe-SA and CdSe-BA TGA profiles are marked, indicating the presence of two-step weight loss.

**Table S1:** Summary of XRD parameters of P3HT (NA), P3HT (TA), P3HT nanofiber films

2 $\theta$ positions	$\theta$	Plane	d
	(°)		(nm)
5.4	2.7	(100)	1.636
11	5.5	(200)	0.804
16	8.0	(300)	0.554

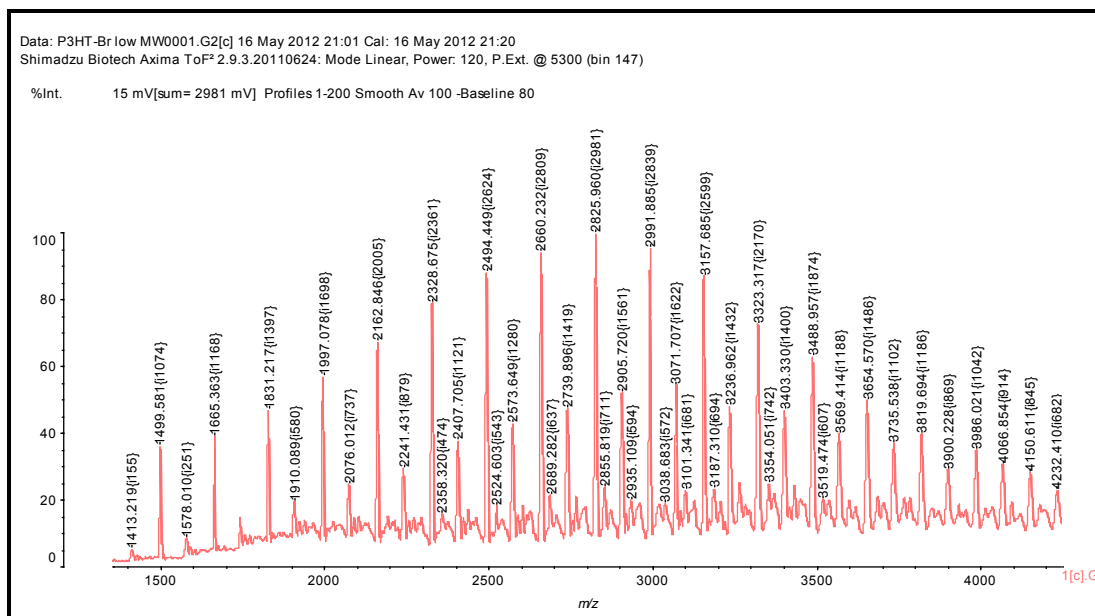
  

Samples	Peak Height	FWHM	Crystallinity
	(counts/s)	(°)	(a.u.)
P3HT (NA)	0.27	0.76	0.205
P3HT (TA)	0.63	0.59	0.372
P3HT nanofiber	1.02	0.83	0.847

**Table S2:** Summary of device performances based on P3HT: CdSe NCs device (non-fiber system) and P3HT nanofiber: CdSe NCs (fiber system), their  $J$ - $V$  characteristic shown in chapter 3.

Device	$J_{sc}$	$V_{oc}$	FF	PCE	$R_s$
	(mA/cm <sup>2</sup> )	(V)		(%)	( $\Omega$ cm <sup>2</sup> )
P3HT: CdSe	4.05 $\pm$ 0.08	0.71 $\pm$ 0.01	0.37 $\pm$ 0.00	1.07 $\pm$ 0.03	86
P3HT nanofiber: CdSe	4.88 $\pm$ 0.07	0.67 $\pm$ 0.00	0.40 $\pm$ 0.00	1.33 $\pm$ 0.04	52

Molecular weight of low molecular weight poly(3-hexylthiophene) (P3HT<sub>L</sub>) used in chapter 3 was characterized by matrix-assisted laser desorption/ionization time-of-the-flight (MALDI-TOF) mass spectroscopy before its end-group functionalization.



**Figure S3:** MALDI-TOF profile of low molecular weight P3HT (P3HT<sub>L</sub>) used for end functionalization.

Photoluminescence (PL) spectra of P3HT nanofiber: CdSe film (without P3HT<sub>L</sub>-py) and hybrid nanostructure film (with P3HT<sub>L</sub>-py) used in solar cells (Chapter 3).

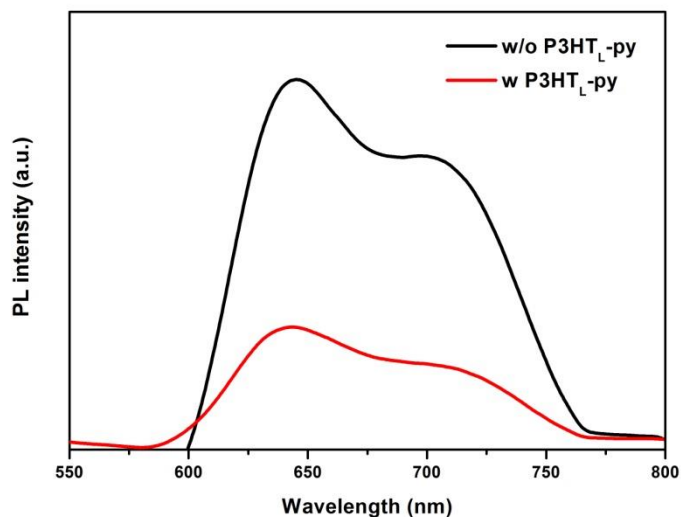
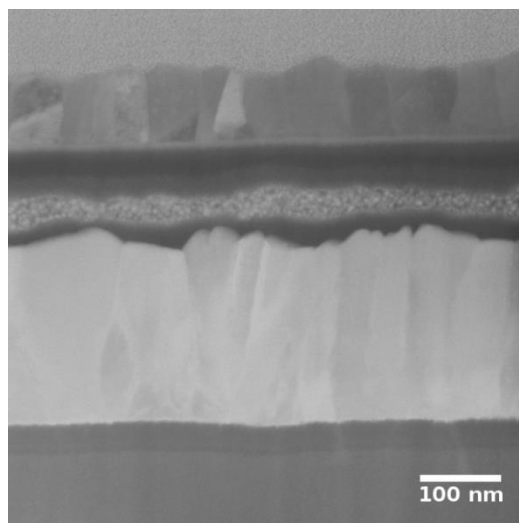


**Figure S4:** PL spectra of thin films of P3HT nanofiber: CdSe (w/o P3HT<sub>L</sub>-py) and hybrid nanostructure (w P3HT<sub>L</sub>-py).

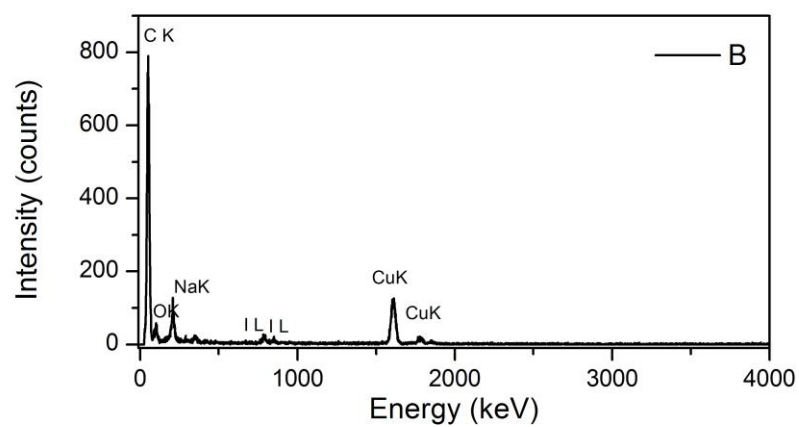
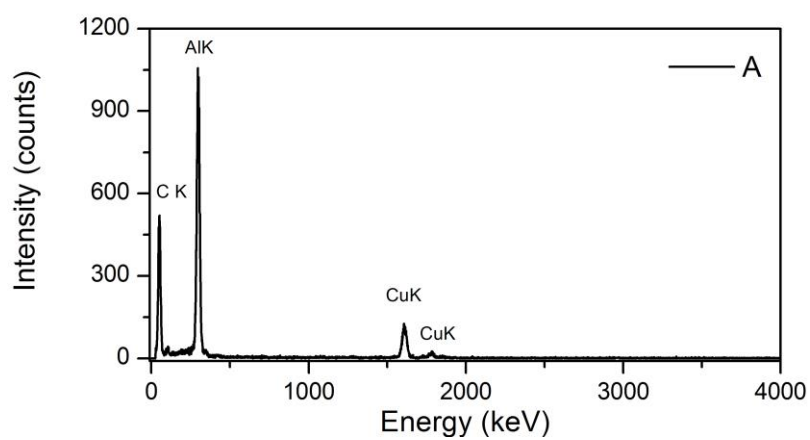
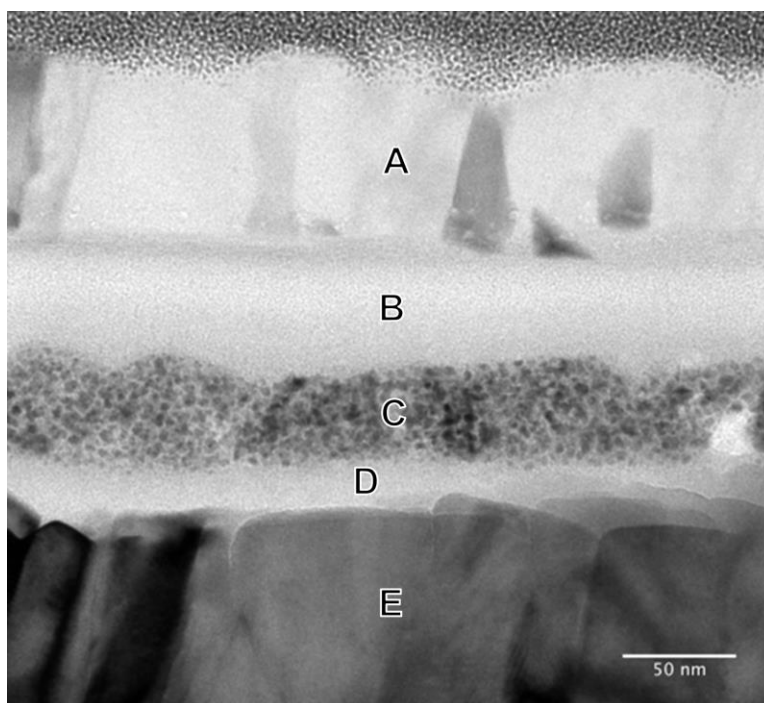
**Table S3:** Summary of device performances based on P3HT nanofiber: CdSe NCs (w/o P3HT<sub>L</sub>-py) and hybrid nanostructure (with P3HT<sub>L</sub>-py), their *J-V* characteristic shown in chapter 3.

Device	$J_{sc}$	$V_{oc}$	FF	PCE	$R_s$
	(mA/cm <sup>2</sup> )	(V)		(%)	(Ω cm <sup>2</sup> )
P3HT nanofiber: CdSe	4.62±0.05	0.65±0.01	0.40±0.01	1.23±0.06	70
P3HT: CdSe hybrid nanostructure	5.12±0.06	0.64±0.01	0.49±0.00	1.59±0.04	34

Cross-section of ITO/PEDOT:PSS/CH<sub>3</sub>NH<sub>3</sub>PbI<sub>3</sub>/PC<sub>61</sub>BM/Al device in chapter five was also examined by scanning transmission electron microscopy (STEM). Its annular dark-field imaging is shown below.



**Figure S5:** ADF-STEM image of FIB sample of ITO/PEDOT:PSS/CH<sub>3</sub>NH<sub>3</sub>PbI<sub>3</sub>/PC<sub>61</sub>BM/Al bilayer device. The bright spots observed in the CH<sub>3</sub>NH<sub>3</sub>PbI<sub>3</sub> layer correspond to the material with high atomic number (Z) elements.



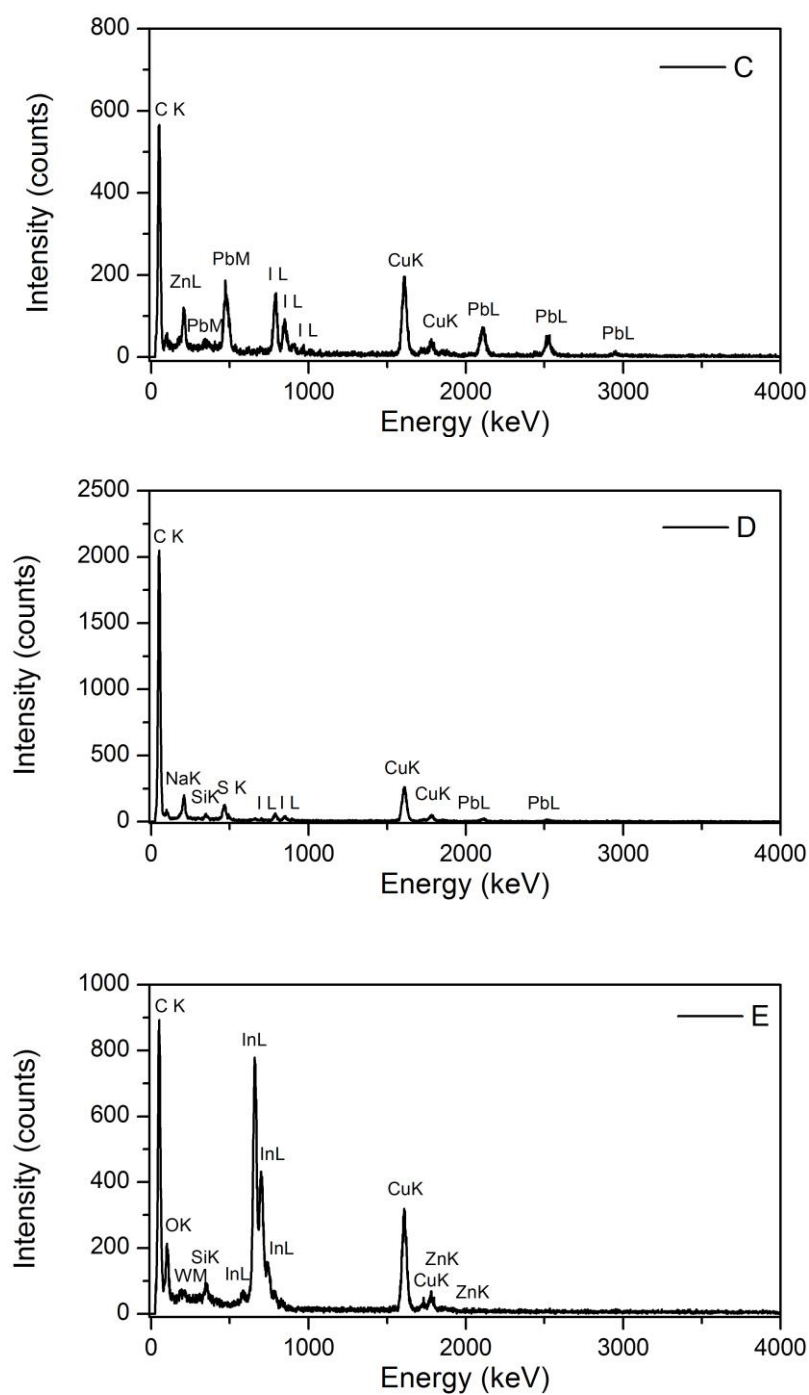


**Figure S6:** EDX spectra from the  $\text{CH}_3\text{NH}_3\text{PbI}_3/\text{PC}_{61}\text{BM}$  bilayer solar cell. Areas A-E correspond to regions in the Al,  $\text{PC}_{61}\text{BM}$ ,  $\text{CH}_3\text{NH}_3\text{PbI}_3$ , PEDOT:PSS and ITO layers respectively (Large).

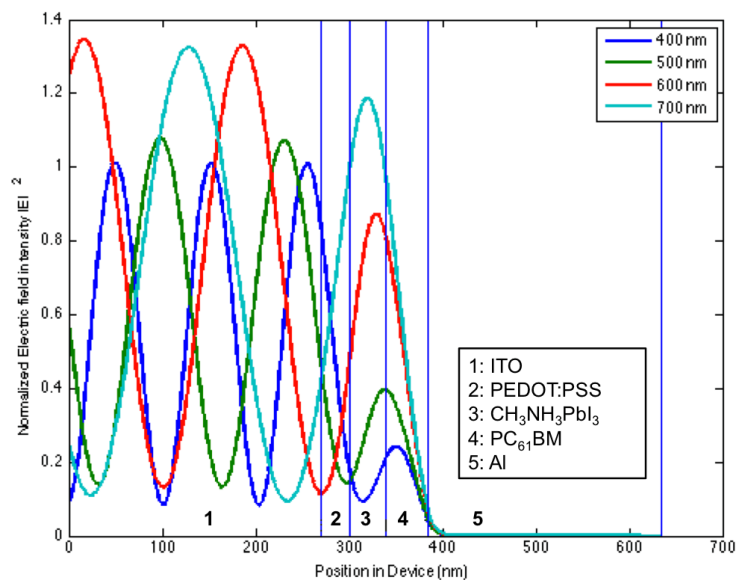


**Figure S7:** Electric field intensity distribution in the  $\text{CH}_3\text{NH}_3\text{PbI}_3/\text{PC}_{61}\text{BM}$  hybrid bilayer solar cell for monochromatic illumination simulated using the transfer matrix model. The position of the local maxima for each wavelength is different.

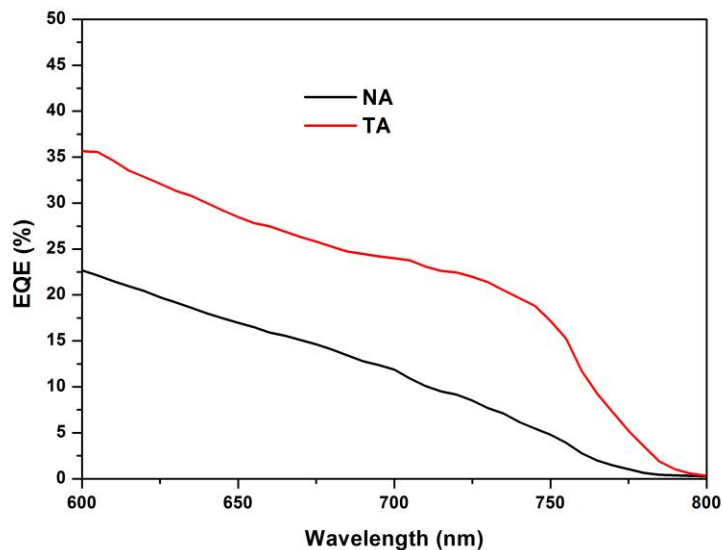


**Figure S8:** EQE spectra of the as-cast (NA) and heat-treated (TA)  $\text{CH}_3\text{NH}_3\text{PbI}_3/\text{PC}_{61}\text{BM}$  bilayer solar cells (600 nm -800 nm) under AM 1.5G illumination.

The EQE onset of the as-cast sample has a more flat region close to 800 nm compared to that of the annealed sample.

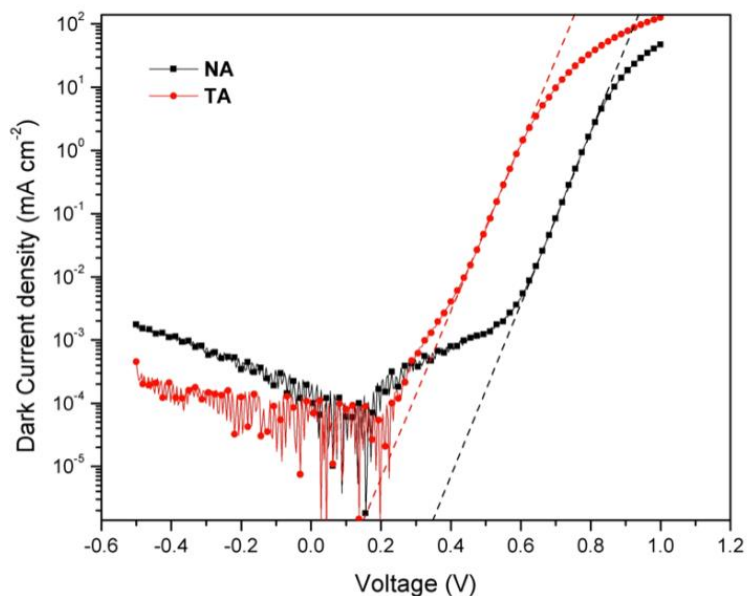


**Figure S9:** Dark semilog current density-voltage ( $J$ - $V$ ) characteristics of the as-cast (NA) and heat-treated (TA)  $\text{CH}_3\text{NH}_3\text{PbI}_3/\text{PC}_{61}\text{BM}$  hybrid bilayer solar cells. The dotted lines are fits to the  $J$ - $V$  characteristics with the ideal diode equation to extract the reverse-saturation current density ( $J_0$ ) and ideality factor ( $n$ ).

**Table S4:** Summary of performance parameters of both as-cast and heat-treated  $\text{CH}_3\text{NH}_3\text{PbI}_3/\text{PC}_{61}\text{BM}$  hybrid bilayer solar cells. The  $\text{CH}_3\text{NH}_3\text{PbI}_3$  thin film was prepared from a 9 wt% solution by spincoating. The heat treatment was performed at 100 °C for 30s

Device	$J_{\text{sc}}$ (mA/cm <sup>2</sup> )	$V_{\text{oc}}$ (V)	FF	PCE (%)	$R_{\text{s}}$ (Ω cm <sup>2</sup> )	$R_{\text{p}}$ (Ω cm <sup>2</sup> )	$J_0$ (mA/cm <sup>2</sup> )	$n$
As-cast	4.65±0.12	1.01±0.02	0.75±0.00	3.48±0.03	14.9	3.7 x 10 <sup>3</sup>	1.36 x 10 <sup>-11</sup>	1.20
Heat-treated	8.20±0.14	0.82±0.03	0.77±0.01	5.23±0.05	6.4	1.6 x 10 <sup>3</sup>	7.01 x 10 <sup>-11</sup>	1.14